Master's thesis

NTNU
Norwegian University of Science and Technology
Faculty of Natural Sciences
Department of Physics

Susanne Aspen Boucher

Characterization of perovskite oxide superlattices using HRTEM, STEM-EELS, 4D-HOLZ-STEM and Segmented SPED

Master's thesis in Nanotechnology
Supervisor: Magnus Nord
June 2023

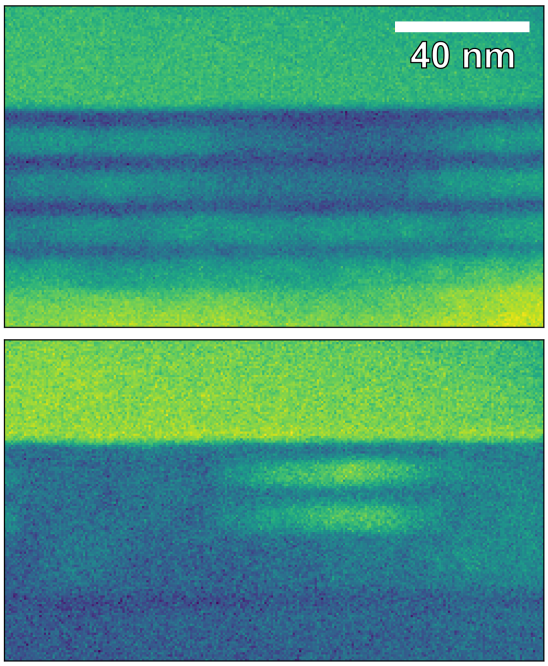

NTNU
Norwegian University of
Science and Technology

Susanne Aspen Boucher

Characterization of perovskite oxide superlattices using HRTEM, STEM-EELS, 4D-HOLZ-STEM and Segmented SPED

Master's thesis in Nanotechnology
Supervisor: Magnus Nord
June 2023

Norwegian University of Science and Technology
Faculty of Natural Sciences
Department of Physics

NTNU
Norwegian University of
Science and Technology

Abstract

Perovskite oxides are promising materials for use in spintronics and other advanced applications due to their strong structure-function coupling. By introducing subtle alterations to the atomic lattice through epitaxial growth on selected substrates, the balance between competing spin, lattice, and electronic degrees of freedom can be controlled, yielding new and novel functional properties.
In this work, two new epitaxial perovskite oxide superlattices, $(LSMO/LFO)_4$/DSO(111) and $(LSMO/LFO)_{10}$/STO(111), were characterized using a range of transmission electron microscopy (TEM) techniques. The samples were grown by pulsed laser deposition (PLD). High-resolution transmission electron microscopy (HRTEM), scanning transmission electron microscopy (STEM) with electron energy loss spectroscopy (STEM-EELS), and higher-order Laue zone-STEM (HOLZ-STEM) was used to study the structural, chemical and electronic properties of the superlattices at the nanoscale. Additionally, the newly proposed segmented scanning precession electron diffraction (S-SPED) methodology was tested, implemented and further developed in order to enhance resolution in SPED datasets by counteracting the effect of probe wandering. The significant improvements in resolution achieved through the application of S-SPED enabled crystallographic characterization of individual superlattice layers, which would not have been achievable with conventional SPED.
Chemical composition EELS studies revealed significant interdiffusion of Fe from LFO into LSMO layers in both superlattices. $(LSMO/LFO)_4$/DSO exhibited chemically distinct layers throughout the superlattice, while $(LSMO/LFO)_{10}$/STO displayed some intermixing of layers potentially due to 3D growth. Signs of oxygen vacancies were observed in the EELS fine structure at the substrate-superlattice interfaces of both samples. A chemical shift of the Mn-L_3 edge onset within individual LSMO layers in $(LSMO/LFO)_4$/DSO was detected, and a change in the ratio of Mn^{3+}/Mn^{4+} was suggested as an explanation. S-SPED, HRTEM, and FFT analysis revealed domain growth and structural distortions in both superlattices. In $(LSMO/LFO)_{10}$/STO, all layers had a similar lattice structure due to unit cell distortions in LSMO. In $(LSMO/LFO)_4$/DSO, the bottom LSMO layer had undergone unit cell distortions, while the subsequent LSMO layers maintained their bulk structure. Both superlattices exhibited at least two structural domains separated by vertical domain walls. In $(LSMO/LFO)_{10}$/STO, the domains were continuous throughout the superlattice, whereas $(LSMO/LFO)_4$/DSO exhibited monodomain growth in the bottom LFO layer and multidomain growth in subsequent layers.

Sammendrag

Perovskittoksider er lovende materialer for bruk i spintronikk og andre avanserte applikasjoner på grunn av deres sterke struktur-funksjonkobling. Ved å innføre små endringer i atomgitteret gjennom epitaksiell vekst på utvalgte substrater, kan balansen mellom konkurrerende spinn-, struktur- og elektroniske frihetsgrader kontrolleres, noe som kan gi opphav til nye og eksotiske funksjonelle egenskaper. I dette arbeidet ble to epitaksielle perovskittoksid-supergitre, $(LSMO/LFO)_4$/DSO(111) og $(LSMO/LFO)_{10}$ /STO(111), karakterisert ved bruk av en rekke transmisjonselektronmikroskopi (TEM)-teknikker. Prøvene er laget med pulset laser-deponering (PLD). Høyoppløsnings-transmisjonselektronmikroskopi (HRTEM), sveipestransmisjonselektronmikroskopi (STEM) med elektronenergitapsspektroskopi (STEM-EELS) og høyere-ordens Lauesone-STEM (HOLZ-STEM) ble brukt for å studere de strukturelle, kjemiske og elektroniske egenskapene til supergitrene på nanonivå.
I tillegg ble den nylig publiserte metodikken for segmentert sveipepresesjonselektro ndiffraksjon (S-SPED) testet, implementert og videreutviklet for å øke oppløsningen i SPED-datasett ved å minimere effekten av probevandring. De betydelige forbedringene i oppløsningen oppnådd gjennom bruk av S-SPED muliggjorde krystallografisk karakterisering av individuelle supergitterlag, noe som ikke ville vært mulig med konvensjonell SPED.
Kjemisk komposisjon undersøkt med STEM-EELS avslørte signifikant interdiffusjon av Fe fra LFO til LSMO-lag i begge supergitrene. $(LSMO/LFO)_4$/DSO hadde kjemisk distinkte lag gjennom hele supergitteret, imens $(LSMO/LFO)_{10}$/STO viste noe blanding av lagsttrukturen, potensielt på grunn av 3D-vekst. Tegn til oksygenvakanser ble observert i EELS-finstrukturen ved substrat-supergitter-grenseflatene i begge prøver. Et kjemisk skift i Mn-L_3-energitapstoppen i individuelle LSMO-lag i $(LSMO/LFO)_4$ /DSO ble detektert, og en endring i forholdet mellom Mn^{3+} og Mn^{4+} ble foreslått som en forklaring.
S-SPED, HRTEM, og FFT-analyse avdekket domenevekst og enhetscelleendringer i begge supergitrene. I $(LSMO/LFO)_{10}$/STO, hadde enhetscelleendringer i LSMO ført til lik struktur i LSMO og LFO. I $(LSMO/LFO)_4$/DSO, hadde det nederste LSMO-laget gjennomgått enhetscelleendringer, imens de etterfølgende LSMO-lagene bevarte sin bulkstruktur. Begge supergitre hadde minst to strukturelle domener, separert av vertikale domenevegger. I $(LSMO/LFO)_{10}$/STO var domenene kontinuerlige gjennom supergitret, imens $(LSMO/LFO)_4$/DSO hadde monodomenevekst i det nederste LFO-laget, og multidomenevekst i påfølgende lag.

Preface

This master's thesis concludes my M.Sc. degree in Nanotechnology at the Norwegian University of Science and Technology.
The research presented in this thesis was undertaken at the TEM Gemini Center at the Department of Physics, during the spring semester of 2023. The work has been supervised by Magnus Nord. In my project thesis, I explored single layer epitaxial LSMO thin films on two different substrates, employing several of the same techniques as in this work. However, all the results presented in this thesis are separate and unrelated to those obtained in the project thesis.
I personally conducted all TEM experiments performed with the *JEOL2100F* with the exception of one session, where instrument alignment was conducted by Emil Frang Christiansen. This work involved SPED, S-SPED and NBD-SED collection. STEM-EELS, HOLZ-STEM and HRTEM acquisitions using the
ARM200F was performed by PhD candidate Marthe Linnerud and my supervisor Magnus Nord. Although this instrument was operated by others, I was responsible for planning these sessions, and participated to the greatest extent possible. All data processing was performed by me, and I have designed all but one of the figures in the thesis, using the Python library Matplotlib [1], PowerPoint and InkScape [2].

Susanne Aspen Boucher
26th June 2023

Acknowledgements

I am deeply grateful to my supervisor Magnus Nord for always engaging in my work with unrelenting enthusiasm. His trust and ambition on my behalf as well as his investment of his own time in my work, has enabled me to delve into advanced techniques and physics far beyond my initial expectations. I would also like to thank Marthe Linnerud and Emil Christiansen for acquiring data with me and always answering my questions expertly. Bjørn Gunnar Soleim should be thanked for his calmness and patience during potentially risky experiments. I am grateful to my friend and classmate, Anders Mathiesen, for his unselfish assistance with early S-SPED data acquisition. His guidance was crucial to my work. Thank you also to Gregory Nordahl, for carefully reviewing everything S-SPED related in the thesis and being incredibly generous in sharing his knowledge of S-SPED. Ingrid Hallsteinsen and Yu Lui should be thanked for creating the exciting superlattices I have grown so fond of over the past months. I am also grateful to Amalie Strømme Falck for her meticulous proofreading of the thesis. To my genius roommate and (lab-)partner in crime Hedda Soland, I would like to extend a heartfelt thank you. I have benefited greatly from her willingness to share her extensive knowledge of TEM, HyperSpy and High-Performance-Computing (HPC). Moreover, the consistent supply of cake and scientific discussions provided by the TEM Gemini Research Group has been a great motivation throughout the past year. Special thanks are due to Inger-Emma Nylund for viewing my results and helping me clear up crystallographic mysteries along the way.
The most important thank you is to my brilliant and weird classmates from nano kull 18. I feel lucky to have gotten to grow up alongside you for the past five years, and I am so proud of all of us.

I would like to acknowledge the substantial computational resources provided by the IDUN High-Performance Computing (HPC) cluster project [3]. Moreover, I recognize the he support from the Research Council of Norway for Norwegian Center for Transmission Electron Microscopy, NORTEM (197405), the Norwegian Micro- and Nano-Fabrication Facility, NorFab (295864).

List of Acronyms

ABF annular bright field

AFM antiferromagnet

BF bright-field

CBED convergent beam electron diffraction

CFEG cold field emission gun

CMR colossal magnetoresistance

CTF contrast transfer function

EDS energy-dispersive x-ray spectroscopy

EELS electron energy loss spectroscopy

ELNES electron energy loss near edge structure

eV electron Volts

FEG field emission gun

FFT fast fourier transform

FIB focused ion beam

FM ferromagnet

GOS generalized oscillator strength

HAADF high-angle annular dark field

HPC high performance computing

HRTEM high-resolution transmission electron microscopy

NBD nanobeam diffraction

PLD pulsed laser deposition

ROI region of interest

SAD selected area diffraction

SED scanning electron diffraction

SPED scanning precession electron diffraction

S-SPED segmented scanning precession electron diffraction

STEM scanning transmission electron microscopy

TM transition metal

TEM transmission electron microscope/microscopy

VBF virtual bright field

VDF virtual dark field

XRD X-ray diffraction

ZLP zero-loss peak

Perovskite Oxide Acronyms

LSMO $La_{0.7}Sr_{0.3}MnO_3$

LFO $LaFeO_3$

STO $SrTiO_3$

DSO $DyScO_3$

Contents

Chapter 1

Introduction

Since the mid-20th century, there has been steady progress in the miniaturization of electronic devices [4]. However, this trend is expected to reach a halt in the near future as device feature dimensions become so small that their function is limited by quantum effects [5]. Simultaneously, the demand for high performance and sustainable computational and memory technology is ever-growing. In order to overcome this bottleneck, a shift from conventional electronics to spintronics has been proposed, triggering research efforts in the exploration of novel materials tailored for such applications [6]. Perovskite oxides are promising materials for use in future spintronic and electronic devices due to their exotic physics and strong structure-function coupling. Epitaxial growth of perovskite oxide heterostructures has emerged as a compelling way to control the balance between spin, charge, and lattice degrees of freedom in order to explore new states and functionalities in these systems [7]. As part of this development, periodically stacked epitaxial multilayers of perovskite oxides have become popular systems for exploration of emergent phenomena [6, 8]. For instance, ferromagnetic metallic behavior in superlattices composed of antiferromagnetic $LaMnO_3/SrMnO_3$ layers [8, 9] has been observed. Additionally, novel polar domain states such as "improper ferroelectricity" [10, 11] and ordered polar vortex arrays have been manipulated by adjusting the periodicity of $PbTiO_3/SrTiO_3$ superlattices [12]. As these functional properties emerge at the nanoscale, it is necessary to use techniques with nanometer resolutions to study these material systems. One such technique is the transmission electron microscope (TEM). Analysing the crystal structure across atomic layer thin film materials in the TEM are commonly done using aberration corrected scanning transmission electron microscopy-high angle annular dark field (STEM-HAADF) [13]. However, this analysis requires sophisticated sample preparation and an advanced TEM. Scanning precession electron diffraction (SPED) is a powerful technique for crystallographic characterization due to the increased quality of the diffraction patterns achieved by precessing the electron beam. This technique is applicable with any TEM equipped with a precession scan generator, and can be performed on of samples of varying quality. Unfortunately, the resolution achievable with SPED is limited due to probe wandering, an unavoidable consequence of precessing the electron beam [14]. This constricts the use of SPED in crystallographic analysis of nanoscale structures such as perovskite oxide thin films.

The new methodology Segmented SPED (S-SPED) proposed by Nordahl et al. [15], enhances the spatial resolution in SPED by counteracting the effects of probe wandering.
In this work, the S-SPED methodology has been implemented and further developed in order to improve resolution in both real and reciprocal space. In addition to this, two new epitaxial perovskite oxide superlattices, $(LSMO/LFO)_{10}$/STO(111) and $(LSMO/LFO)_4$/DSO(111), have been characterized using a range of TEM techniques, including S-SPED methodology. High resolution transmission electron microscopy (HRTEM), scanning transmission electron microscopy-electron energy loss spectroscopy (STEM-EELS) and higher order Laue zone-STEM (HOLZ-STEM) has been applied to study structural and chemical properties of the superlattices at the atomic level. The superlattices, while not designed for a specific application, provide valuable insights into fundamental responses to epitaxial multilayered growth. The aim of this thesis is to monitor these responses by studying the structural, chemical and electronic properties of the superlattices utilizing TEM techniques, and further develop a methodology to study these nanoscale material systems.
As the S-SPED methodology development is not related to the characterization of the superlattices, a separate chapter is dedicated to the subject of S-SPED development, while the rest of the thesis addresses the overall TEM characterization work.

Finally, a few words from two perovskite oxide research veterans.

> *"... we believe that the complex oxide materials with the most impact and influence remain to be unleashed. These new physical phenomena are on the verge of being exposed in oxide superlattices as we (the collective practitioners of oxide electronics) learn to navigate this relatively unexplored amalgamation of interfaces and competing order parameters in search of marvel."*
> – Ramamoorthy Ramesh and Darrell G. Schlom [6]

Chapter 2

Theory

This chapter assumes familiarity with solid state physics, TEM and EELS. References to learning materials dedicated to fundamental theory within these fields are included in the following sections. Instead of presenting general concepts found in the referenced learning materials, this chapter aims to highlight the principles behind the less established TEM techniques used, and provide a theoretical framework for the specific findings in this work. Theory specifically regarding the S-SPED methodology is included Chapter 4.

2.1 Crystal structures

2.1.1 Perovskite oxide structure

An ideal perovskite oxide has an ABO_3 crystal structure as illustrated in Figure 2.1. The structure consists of a central B cation surrounded by an oxygen octahedron, with A cations in the corner positions.

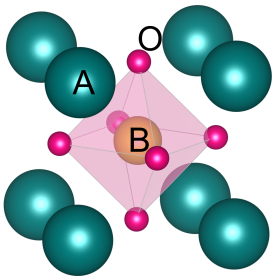

Figure 2.1: Ideal perovskite oxide ABO_3 structure.

Deviations from the ideal relationship between the ionic radii of A and B cations give rise to a range of different structural distortions such as cation shifts or oxygen octahedral rotation and tilt [7]. Since the different degrees of freedom in perovskite oxides compete at similar energy scales, even slight structural modifications can significantly alter their functional behavior in different ways. This is the origin of the versatility and richness of functional properties characteristic for this material class [6].

Table 2.1: Bulk crystal structure, pseudocubic unit cell parameters and octahedral tilt in Glazer notation for LSMO, STO, LFO and DSO [20, 22, 21, 13].

Compound	**Lattice**	**PC unit cell [Å]**	**Octahedral tilt**
LSMO	rombhedral	$a_{pc} = 3.869$	$a^-a^-a^-$
STO	cubic	$a = 3.905_c$	$a^0a^0a^0$
LFO	orthorhombic	$a = 3.927_{pc}$	$a^-a^-c^+$
DSO	orthorhombic	$a = 3.972_{pc}$	$a^-a^-c^+$

2.1.2 Crystal structures of LSMO, LFO, DSO and STO

Using standard Miller indexing convention, crystallographic planes are denoted by parenthesis (hkl), while directions are represented by square brackets [uvw] [16]. The subscripts *c* (cubic), *pc* (pseudocubic), *o* (orthorombic) *rh* (rombohedral) and *h* (hexagonal) will be used throughout the thesis to differentiate between different unit cell symmetries. $SrTiO_3$ (STO) has a cubic unit cell with lattice parameter $a_c = 3.905$ Å and belongs to space group $Pm\bar{3}m$ (no. 221) [17]. $LaFeO_3$ (LFO) and $DyScO_3$ (DSO) both have an orthorombic unit cell and belongs to the *Pbnm* (no. 62) space group. LFO has unit cell parameters $a_o = 5.556$ Å, $b_o = 5.565$ Å, and $c_o = 7.862$ Å, and DSO has unit cell parameters $a_o = 5.44$ Å, $b_o = 5.71$ Å, $c_o = 7.89$ Å [18, 19]. (LSMO) has a rombohedral unit cell and belongs to the $R\bar{3}c$ space group (no. 167). The lattice parameters of LSMO are $a_{rh} = 5.471$ and $\alpha = 60.471°$. LSMO will be illustrated with an equivalent hexagonal unit cell with $a_h = 5.503$ Å, $b_h = 5.503$ Å and $c_h = 13.342$ Å, with $\alpha = 90, 90, 120°$[20], as online resources and publications generally utilizes this. For convenient comparison of the different crystal structures, a pseudocubic unit cell is attributed to all the perovskite oxides. The pseudocubic unit cell is defined with *Pbnm* notation, giving $[001]_{pc} \parallel [001]_o$ and $[110]_{pc} \parallel [100]_o$, in accordance with previous work done on cubic and orthorombic heterointerfaces [21]. For orthorombic unit cells, the following equation was used to calculate the pseudocubic lattice parameters [21].

$$a_{pc} = \frac{\sqrt{a_o^2 + b_o^2} + \frac{c_o}{2}}{3} \tag{2.1}$$

The pseudocubic lattice parameter for LSMO was calculated using the equation below [21].

$$a_{pc} = \frac{a_{rh}}{\sqrt{2}} \tag{2.2}$$

Information about the unit cell structure, the pseudocubic lattice parameters (a_{pc}) and the octahedral tilt of LSMO, STO, LFO and DSO is summarized in Table 2.1. According to X-ray diffraction (XRD) simulations using InteractiveXRDFit [23] conducted by Hallsteinsen and Liu, the two superlattices consist of (LSMO27uc/LFO 32uc)$_4$/DSO and (LSMO5uc/LFO8uc)$_{10}$/STO. The lowercase number, 4 and 10, refers to the number of repeating layers, and the abbreviation 'uc' refers to the the number of $(111)_{pc}$ planes present in each layer. The notation (LSMO/LFO) indicates that LFO

is the bottom layer and LSMO is the top layer in each repetition. For convenience, the samples will be referred to as $(LSMO/LFO)_4/DSO$ and $(LSMO/LFO)_{10}/STO$. $(LSMO/LFO)_4/DSO$ and $(LSMO/LFO)_{10}/STO$ are $\approx$ 56 and $\approx$ 43 nm across, respectively. This means that $(LSMO/LFO)_4/DSO$ has 8 relatively "thick" multilayers, while $(LSMO/LFO)_{10}/STO$ has 20 "thinner" layers.

2.1.3 $(111)_{pc}$ interface symmetries

The following section outlines the orientation relationships and symmetries at $(111)_{pc}$ interfaces. A particular focus will be on LFO/STO$(111)_c$ and LFO/DSO$(111)_{pc}$, as these initial growth interfaces are expected to have an important impact on the superlattice structures. In LSMO, the $(001)_h$ facet is equivalent to the $(111)_{pc}$ facet [22]. For LFO and DSO, both the $(011)_o$ and $(101)_o$ facets are equivalent to the $(111)_{pc}$ facet. These two cases correspond to either having the orthorombic and a_o or b_o axis parallel to the $(111)_{pc}$ plane [21, 18]. The DSO substrate has a $(101)_o$ orientation according to the manufacturers at SurfaceNET GmbH [24], and therefore has $b_o \parallel (111)_{pc}$. Figure 2.2 shows the $(111)_{pc}$ facets of each perovskite oxide, along with a pseudocubic representation of the unit cell visualized with Vesta [25]. Only one of the possible $(111)_{pc}$ facets of LFO are included in the illustration.

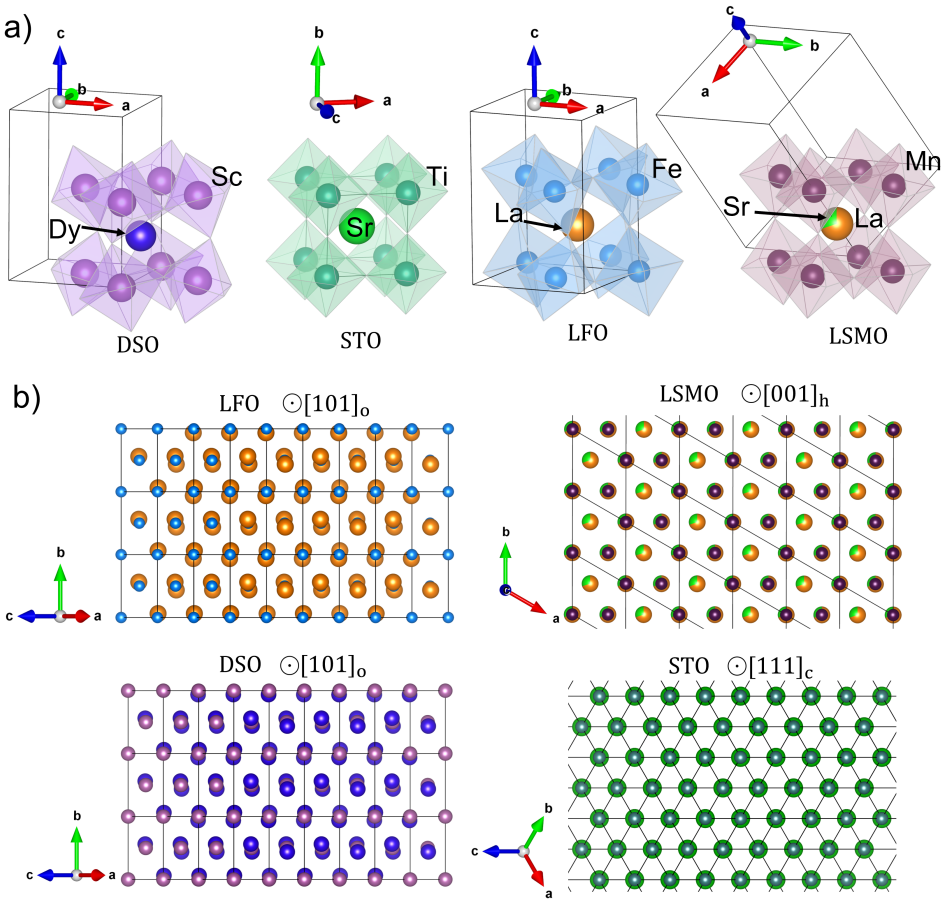

Figure 2.2: a) Pseudocubic representations of DSO, STO, LFO and LSMO. Note that the relative ionic radii are not to scale. b) $(111)_{pc}$ facets of LFO and DSO seen along the $[101]_o$ zone axis, LSMO seen along the $[001]_h$ zone axis and STO along the $[111]_c$ zone axis.

Analogously to utilizing a pseudocubic unit cell to compare the perovskite oxides, the surface symmetry of the $(111)_{pc}$ facets will be described as hexagonal and pseudo-

hexagonal. While LSMO and STO have perfect hexagonal surface symmetry in the $(111)_{pc}$ orientation, LFO and DSO have a pseudo-hexagonal symmetry due to buckling of the hexagons [21]. This means that the three-fold rotation symmetry of the $(111)_{pc}$ facets is degenerate for LSMO and STO and not for LFO and DSO. The term rotation on a $(111)_c$ plane refers to the rotation of the unit cell around the direction perpendicular to the plane, in this case $[111]_c$. The rotation of an orthorombic unit cell on a $(111)_c$ substrate is illustrated in Figure 2.3, along with a schematic of the two orthorombic $(011)_o$ and $(101)_o$ facets.

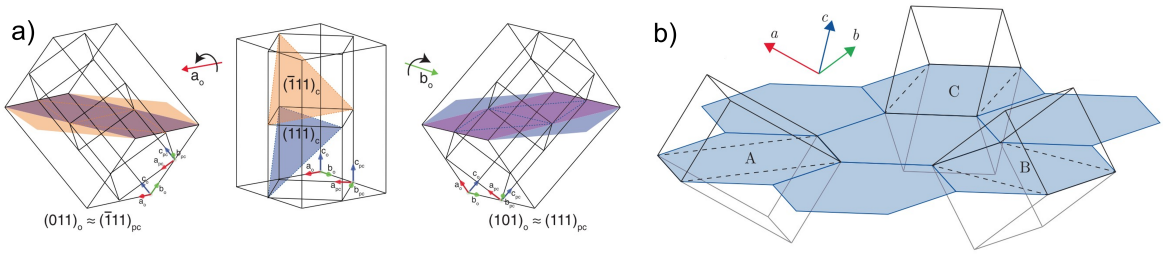

Figure 2.3: Image courtesy of Kjærnes et al. [21]. a) Relationship of the $(101)_o$ and $(011)_o$ facets with $(111)_{pc}$ and $(\bar{1}11)_{pc}$ crystal planes, respectively. b) Three-fold rotation of the orthorombic unit cell on the $(111)_{pc}$ facet.

The two variants of the orthorombic $(111)_{pc}$ facets have the same degree of hexagonal buckling, which is also referred to as net orthorombic distortion [21]. However, the direction of the buckling is different for the two facets with respect to a $(111)_{pc}$ substrate. This will not be discussed further, but is mentioned to illustrate that the strain conditions for $(101)_o$ and $(011)_o$ facets are not equivalent on the STO$(111)_c$ and DSO$(101)_o$ substrates. Further details on the orthorombic, cubic and rombohedral $(111)_{pc}$ interface symmetry can be found in Section 5.2.1 and in ref. [21].
The (LSMO/LFO)$_{10}$/STO sample is cut along the $[01\bar{1}]$ plane, and imaged in the TEM along the $[2\bar{-}1\bar{-}1]$ zone axis. The (LSMO/LFO)$_4$/DSO sample is cut at a 90°angle relative to (LSMO/LFO)$_{10}$/STO, and is imaged along the $[0\bar{1}1]$ zone axis. For the sake of comparability between the different crystal structures, all diffraction patterns and fast Fourier transforms (FFTs) will be indexed with pseudocubic (hkl) indices. In images, single superlattice layers will be annotated with numbers beginning at the film/substrate interface, and increasing in successive layers away from the substrate. Similarly, the terms "down" and "up", or "bottom" and "top" will correspond to positions closer to and further away from the substrate, respectively. These terms are intended to reflect the sequential nature of PLD growth.

2.1.4 Origin of magnetic properties in LSMO and LFO

This thesis primarily focuses on TEM characterization of structural and chemical properties in the superlattices. However, certain structural and chemical alterations are known to impact the functional properties of the involved materials. It is therefore useful to include a brief description of the origin of the bulk functional properties in

these materials. The emphasis will be on the origin of magnetic properties in bulk LFO and LSMO. Magnetic interaction theory is from "Magnetism in Condensed Matter" by Blundell [26], where more extensive information can be found.
Bulk DSO and STO are insulators and exhibit paramagnetism and diamagnetism, respectively, at room temperature [27, 7]. LFO is a room temperature anti-ferromagnet (AFM) due to super-exchange between Fe^{3+}-O^{2-}-Fe^{3+}. LFO has the highest Néel temperature (T_N = 740 K) and the largest Fe-O-Fe buckling angle (155°) in the orthoferrite family [28]. LFO is often referred to as a prototypical antiferromagnetic (AF) insulator and is considered a promising material for spintronic devices and novel memory applications. The formation of AF domains as a consequence of structural domain growth presents a challenge in controlling the Néel vector in LFO, necessary for novel applications [21]. To control the Néel vector, it is desirable to achieve monodomain growth of LFO.
The mixed valence state in $La_{0.7}Sr_{0.3}MnO_3$ results in a double-exchange mechanism between Mn^{3+}-O^{2-}-Mn^{4+}, responsible for ferromagnetic (FM) ordering in LSMO. Additionally, the electronic and structural degrees of freedom are linked through crystal field and Jahn-Teller effects [17]. This results in a Curie temperature of (T_C = 370 K), colossal magnetoresistance (CMR) and close to fully spin polarized electronic subbands at the Fermi level in LSMO. LSMO is therefore considered a promising candidate for magnetic tunneling junctions and other spintronic applications [29].
Factors which are expected to interfere with the magnetic exchange interactions in these materials are structural domain growth, strain, cation diffusion, oxygen vacancies, and alterations in the B cation oxidation state [7, 28]. These are therefore especially interesting properties to characterize in the superlattices.

2.2 Transmission Electron Microscopy

In this section, the principles behind the applied TEM techniques will be presented. The information in the TEM and electron diffraction section is from "Transmission Electron Microscopy" by Williams and Carter [30]. General diffraction theory is also based on "Introduction to Solid State Physics" by Kittel [16]. The 4D-STEM and SPED sections have information from the chapter "Precession Electron Diffraction" in "Advances in Imaging and Electron Physics" by Eggeman and Midgley [31]. Individual citations will not be given in the following sections. The reader is directed to these sources for more extensive information about the presented topics.

2.2.1 TEM and STEM

A transmission electron microscope utilizes high-energy electrons transmitted through a thin specimen to generate images of the specimen at the atomic scale. In conventional TEM, the sample is "illuminated" with a parallel electron beam in one single exposure. In STEM imaging, a nanoscale convergent electron beam is used to scan the sample in a raster pattern. In STEM, annular detectors are used to collect electrons scattered to specific semi-angles. The image contrast depends on the collection angle.

STEM-HAADF images are created with electrons scattered to high angles ($\sim$ 50 to 400 mrad). STEM-HAADF images are also called Z-contrast images due to the contrast proportionality to atomic number ($\approx Z^2$). Heavier atoms scatter to wider angles, and will therefore appear brighter compared to lighter elements in STEM-HAADF images. High Resolution TEM (HRTEM) is an effective and accessible technique to image the atomic lattice. However, interpreting the contrast in HRTEM images is complicated, as the contrast mechanism depends on changes in the phase and amplitude of the electron beam. As outlined by Eggeman and Midgley [31], several factors can influence the phase relationships in the scattered beam, resulting in different image contrast. The sample must be ultrathin and exactly on zone axis to image the atomic columns. Moreover, the phase relationships in the scattered beam is sensitive to lens aberrations. In addition to instrument and sample dependent factors, the Contrast Transfer Function (CTF) for HRTEM is significantly more complicated than for other imaging techniques such as STEM-HAADF. The CTF describes how the microscope transfers contrast from the specimen to the final image as a function of spatial frequency, relating the contrast to the periodic lattice structure. In STEM-HAADF, the CTF is a positive straight line, while in HRTEM, it oscillates between 1 and -1. This means that some lattice periodicities will give positive contrast, some negative contrast, and certain lattice periodicities will give no contrast. It is therefore not straightforward to relate the observed contrast in HRTEM images to the atomic lattice of the specimen, and this should ideally be coupled with simulations. The interpretations of HRTEM images in this work are therefore made under consideration of these issues and in conjunction with other techniques such as S-SPED and HOLZ-STEM.
There are two main types of electron detection used in TEM, called indirect and direct electron detection. Indirect electron detection involves the conversion of the electron signal to a photon signal using a scintillator, which is then detected with a CCD or CMOS camera. On the other hand, direct electron detectors (DED) directly detect the impinging electrons using pixel sensors connected to smart chips [32]. This technology provides superior noise filtering and quantum efficiency compared to conventional detection methods, making it particularly well-suited for 4D-STEM applications.

Conventional diffraction in TEM

Diffraction arises from low angle, coherent, elastic scattering, reflecting the wave nature of electrons. The atomic lattice acts as a grid of scattering centers, causing interference of the electron beam. The diffracted beam propagates at specific angles respective to the direct beam, and the condition for diffraction is determined by the crystallographic orientation and plane separation. This is termed Bragg scattering. The Ewald sphere is a geometric construct which represents the set of scattering vectors in reciprocal space that meet the diffraction condition given the wave vector of the incident beam. Essentially, all reciprocal lattice points which intersect with the surface of the Ewald sphere meet the diffraction condition. Thus, diffraction pattern acts as a 2D projection of a region of the reciprocal lattice, and is therefore a valuable source of crystallographic information.
The Fast Fourier Transform (FFT) of a HRTEM image is a mathematical transform-

ation that converts the image from real to reciprocal space, resulting in a pattern that represents the periodicity and symmetry in the crystal lattice. Although this is a purely mathematical method, FFT analysis of HRTEM images can yield similar structural information about a crystal as diffraction patterns.
A common technique in TEM diffraction experiments is to use a selected area aperture to block a portion of the beam, so that electrons only interact with a selected region of the sample. The technique is called selected area diffraction (SAD), and is used to inspect diffraction patterns originating from selected sample regions. Another common technique used in conventional TEM diffraction is dark field (DF) imaging. By placing an aperture in the back focal plane of the objective lens, it is possible to select electrons scattered to one specific diffraction reflection. Only electrons scattered to the selected diffraction spot will contribute to form an image of the specimen, making regions which fulfill the condition for diffraction to that reflection appear bright. This is commonly done to identify and image differently oriented crystal grains. Conversely, the centre spot can be selected with an aperture to form a bright field (BF) image. In this case, the image is formed by non-scattered electrons. Bright contrast in BF images corresponds to weakly scattering regions, such as amorphous regions or vacuum. This explanation, while somewhat simplified, aims to illustrate the contrast characteristics of BF and DF imaging.
Extinction is the phenomenon where reflections which are expected to occur based on the crystal structure are systematically absent from the diffraction pattern. Extinction occurs when the the scattered beams interfere destructively. This is a result of crystal symmetry, and specific crystal symmetries therefore have distinct set of extinction rules. The kinematic scattering model assumes that the electron beam only interact with the crystal once. In ultrathin samples, this can be a sufficient approximation. However, in most thicker samples, multiple scattering events are likely to occur. This is described by dynamic scattering theory. A key difference between kinematic and dynamic scattering is that extinction rules apply in kinematic scattering, but not necessarily in dynamic scattering. Reflections which are extinct as a result of crystal symmetry may therefore be present in the diffraction pattern due to dynamic scattering events. As extinction is a result of the wave nature of the electron, extinction does not apply in FFT images. This means that kinematically extinct reflections are present in FFT patterns. This is a simplified explanation of dynamic and kinematic scattering and extinction, provided in order to interpret the diffraction patterns obtain in this work. For information about the fundamental principles and nuances of these phenomena, the reader is directed to "Introduction to Solid State Physics" by Kittel [16] and "Transmission Electron Microscopy" by Williams and Carter [30].

2.2.2 4D-STEM and CBED

This section uses information from the chapter "Precession Electron Diffraction" in "Advances in Imaging and Electron Physics" by Eggeman and Midgley [31], as well articles by Vincent et al. and Barnard et al.[14, 33].
In conventional TEM, diffraction patterns are acquired with a parallel electron beam. Another diffraction imaging method is convergent beam electron diffraction (CBED), where a convergent STEM probe is used to generate diffraction patterns from small sample regions. It is common to use a very large convergence angle in CBED acquisition, often leading to overlap of the diffraction disks. In this work, the convergence angle was kept smaller than in conventional CBED in order to separate the diffraction disks.
The term 4D-STEM is a collective term referring to all scanning techniques where a diffraction pattern is recorded for each scan position on the sample. Fast pixelated direct electron detectors are used to acquire 4D-STEM data. A schematic representation of the 4D-STEM acquisition procedure and data structure is shown in Figure 2.4. The electron beam, illustrated as a blue cone, records a diffraction pattern at each scan position, represented as a grid point on the sample. The diffraction pattern is "stored" at this scan position in the dataset. Thus, 4D-STEM data represents both real space and diffraction information simultaneously.The illustration in Figure 2.4 shows 4D-STEM acquisition with a precessing beam (indicated with a cone shaped electron probe). Note that the depicted data structure is universal for all 4D-STEM techniques.
A wealth of information can be extracted from 4D datasets through data processing. The diffraction pattern from different probe positions can be examined individually, or diffraction patterns from a region of interest can be summed for increased intensity. Conceptually, this is analogous to SAD in conventional TEM, only with the opportunity to choose any size and shape of the SA aperture. Another powerful application of 4D-STEM is virtual imaging. Virtual images of the sample are generated by application of virtual apertures to the diffraction data. Analogously to BF/DF-TEM and ABF/ADF-STEM imaging, only electrons scattered to angles collected by the virtual detector contribute to the intensity of each scan position in the reconstructed image. Thus, regions of the sample with an orientation that scatters to that specific detector area will appear bright in the virtual image.
A virtual bright field (VBF) image is created when the transmitted beam, the 000 diffraction spot, is selected. This gives images where the regions with less scattering appears brighter, as in conventional TEM-BF. Probe positions in amorphous regions or vacuum will consequently appear brightest. Conversely, when a diffraction spot is selected with a virtual aperture, a virtual dark field (VDF) image emerges. In these cases, crystalline regions areas of the sample which scatter the beam to the angles defined by the virtual aperture, and therefore fulfil a given diffraction condition, will appear bright. VDF is useful for imaging grain orientations and domain growth in crystalline materials.

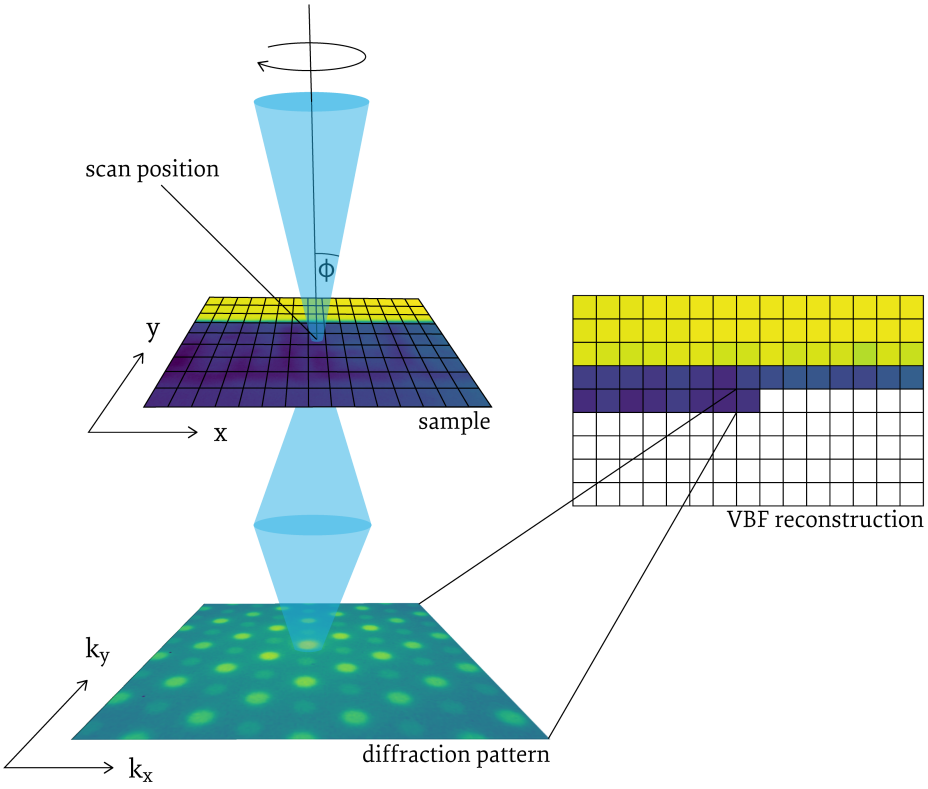

Figure 2.4: Schematic of the acquisition procedure and data structure in 4D-STEM. For each scan position, a diffraction image is recorded and "stored in a scan point" in the virtual image labelled "VBF reconstruction". The process of generating virtual images is not illustrated.

The advantage of 4D-STEM lies in the capacity to generate a multitude of virtual images, each revealing potentially unique information about the sample, all from a single scan. Thus, virtual images are useful for virtual inspection and qualitative analysis of the sample.
A convenient tool in convergent beam alignment procedures is the ronchigram. The ronchigram is a shadow image of the specimen formed when a convergent beam is at or close to focus on the specimen. The centre of the ronchigram is called the "aberration free region", as it shows the angular extent of non-aberrated rays from the optical axis.

2.2.3 SPED

Scanning Precession Electron Diffraction (SPED) is a type of NBD-SED (nano-beam diffraction-scanning electron diffraction) where the electron beam is tilted to an azimuthal angle (typically 0.5-3°) and rotated around the optical axis at each scan position. This angle is called the precession angle (ϕ), and is indicated in Figure 2.4. Scanning electron diffraction (SED) is a broad term which normally encompasses several techniques, including SPED. The term NBD-SED will be used to describe the technique which is equivalent to SPED, but without beam precession. The introduction of precession compared to NBD-SED adds benefits to the electron diffraction patterns in several ways. Firstly, diffraction patterns acquired with SPED contains a greater number of reflections than in NBD-SED, assuming otherwise equal acquisition parameters. As the probe precesses, the Ewald sphere moves through the reciprocal lattice with a rocking motion. This causes the surface of the Ewald sphere to intersect with a greater number of reciprocal lattice points than in NBD-SED, where the Ewald sphere is stationary. The intensities of all excited reflections throughout the azimuthal rotation are integrated to produce the final diffraction pattern. This process is illustrated in Figure 2.5.

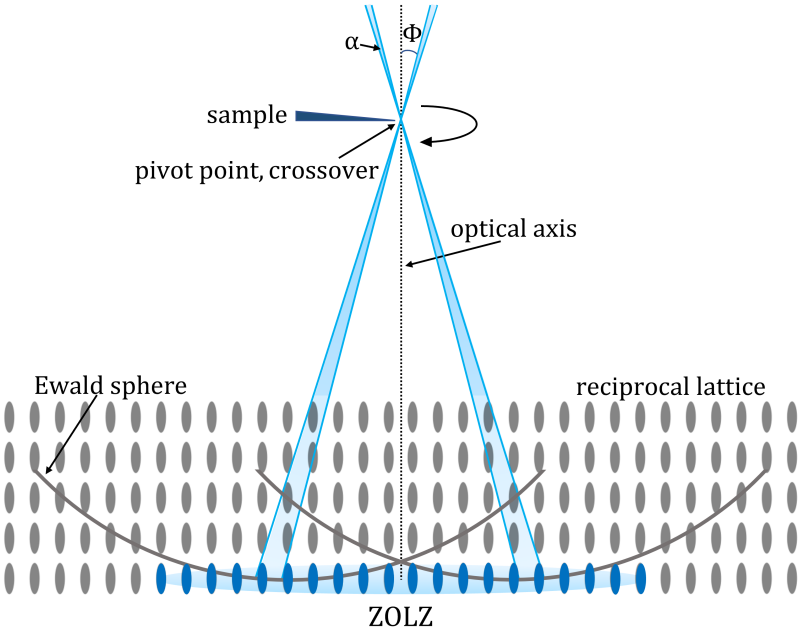

Figure 2.5: Schematic of the precessing electron beam and the interception of the rocking Ewald sphere with the reciprocal lattice points marked with blue. The precession angle (ϕ) and convergence angle (α) are indicated along with the sample position, pivot point and beam crossover. Please note, the diagram is not to scale and in reality the incident beam should intersect with the Ewald sphere perpendicularly. Design choices were made to ensure the inclusion of all essential features.

Another benefit of precession is that intensity variations in the convergent diffraction disks are averaged out due to the rocking motion, giving a uniform intensity in each diffraction spot. The uniformity of diffraction spots in SPED facilitates the detection of their precise position in data processing. This is an essential step in SPED data processing tasks such as orientation or strain mapping, making SPED the preferred technique for performing these analyses. The tilting of the beam off zone axis helps minimize the effects of dynamic scattering, making SPED diffraction patterns more kinematic-like.
A drawback with SPED is a potential loss of spatial resolution compared to NBD-SED. When the beam is tilted away from the optical axis and outside of the aberration free area of the ronchigram, the beam gets displaced from the optical axis proportional to the gradient of the local aberration function [34]. Under normal alignment, this results in a periodic motion of the beam referred to as probe wandering [14]. This motion is integrated at each scan point, giving a larger time-averaged probe and consequently a reduction in spatial resolution. Spatial blur due to probe wandering increases with the precession angle with blur $\sim \phi^2$ for $\phi > 15$ mrad, as predicted by Vincent and Midgley [33].
Another challenge with SPED compared to NBD-SED, lies in its time-consuming alignment process and stringent alignment conditions. Moreover, alignment becomes increasingly difficult for higher magnification and larger precession angles. Figure 2.5 shows a well aligned SPED setup, where the electron beam crossover and pivot point are aligned with the sample. This point will be referred to as the focus point in SPED. Deviations from this alignment can further degrade spatial resolution by introducing additional probe shift. The term "probe wandering" will be used to describe the unavoidable probe motion inherent to SPED, and "probe shift" will refer to motion caused by instrument misalignment, as these are important distinctions.

2.2.4 4D-HOLZ-STEM

The reciprocal lattice planes perpendicular to the electron beam which intersect with the Ewald sphere are termed Laue zones (LZ). The plane intersecting the Ewald sphere at the point of incidence of the electron beam, is called the zeroth order Laue zone (ZOLZ). The ZOLZ gives rise to the diffraction patterns which are usually detected in conventional SAD and NBD-SED. The first intersecting reciprocal space plane which extends beyond the ZOLZ is called the first-order Laue zone (FOLZ), the second is called the second-order Laue zone (SOLZ) and so on. Collectively, all Laue zones beyond the ZOLZ are termed higher-order Laue zones (HOLZ). When a convergent beam is scattered from HOLZ, it forms concentric rings around the central spot, each representing a LZ. The Ewald sphere intersecting with HOLZ, and the resulting convergent beam diffraction patterns is illustrated in Figure 2.6. As the periodicity of the reciprocal lattice reflects the periodicity of the real space lattice, the number of LZ intersecting with the Ewald sphere depends on the real space lattice periodicity along the electron beam. Figure 2.6 illustrates how periodicity doubling in the atomic lattice along the electron beam leads to a doubling of the HOLZ rings in the diffraction

pattern.

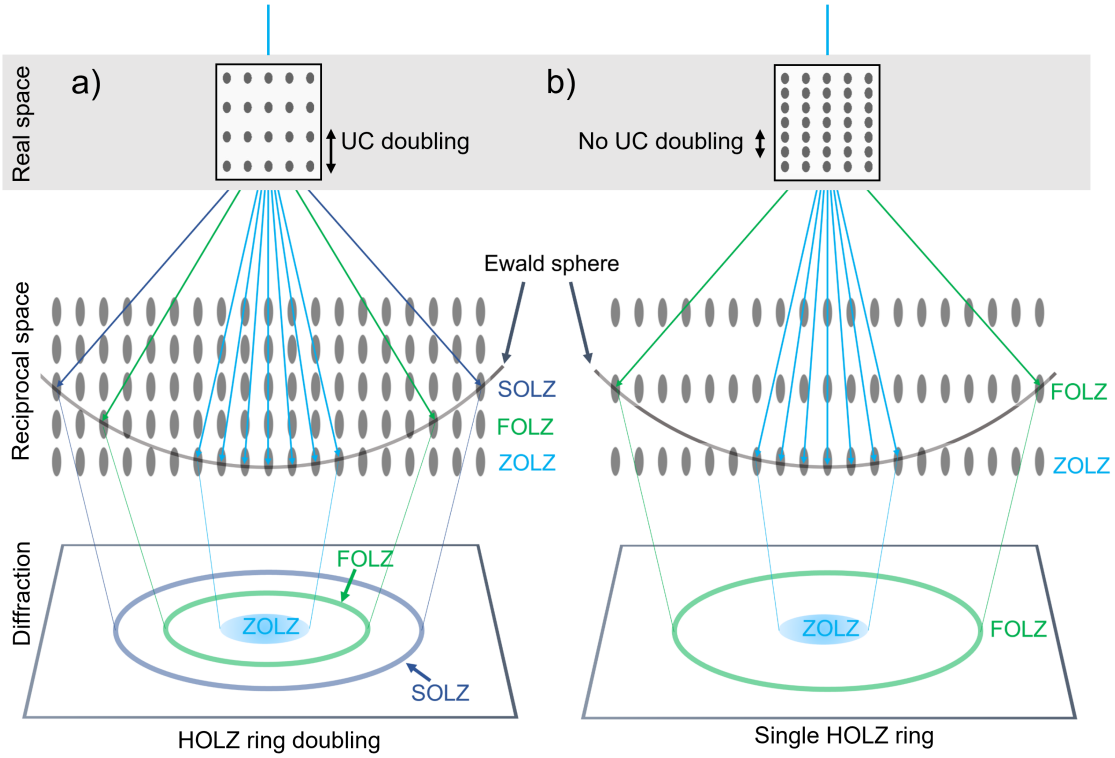

Figure 2.6: Schematic showing the Ewald sphere intersecting with the ZOLZ and HOLZ and resulting CBED pattern in the case of a) periodicity doubling and b) no periodicity doubling along the electron beam.

The real space plane separation along the electron beam is doubled in Figure 2.6 a) compared to in Figure 2.6 b). This periodicity doubling in real space is equivalent to introducing new intermediate planes in the reciprocal lattice. In Figure 2.6 a), this is shown by the appearance of a new FOLZ. Consequently, the Ewald sphere intersects with the twice as many LZ, and the number of HOLZ rings doubles in in the diffraction pattern in Figure 2.6 a) compared to b). Thus, HOLZ-STEM can be utilized to image changes in lattice periodicity along the electron beam. This was proposed by Huang et al. [35]. Nord et al. utilized this technique to study periodicity doubling along the electron beam in an LSMO/LFO/STO(111) bilayer using fast pixelated direct electron detector technology to acquire 4D-HOLZ-STEM data [36, 37]. Overall, HOLZ-STEM is a powerful technique for obtaining 3D information about a sample from a single orientation.

2.3 STEM-EELS

2.3.1 Chemical characterization with EELS

This section is based on information from "Electron Energy-Loss Spectroscopy in the Electron Microscope" by Egerton [38], where more extensive information about EELS can be found.
The electron beam undergoes several types of inelastic scattering which transfer energy from the incident beam to the sample. One important inelastic scattering mechanism is inner shell ionization. In EELS, the detected electron energy loss is equal to the energy required to remove an electron from an inner shell of an atom. This energy threshold is unique to each element. The resulting EEL spectrum features are called core loss edges or ionization edges, and serve as a chemical fingerprint for the elements in the sample. The relative intensity of the core loss edges in EELS are related to the relative chemical composition in the sample. Combined with STEM, EELS is a powerful technique for localized characterization of the specimen. The terms core loss edge and ionization edge will be used interchangeably throughout the thesis. Conventionally, the term "low loss" describes the part of the EEL spectrum where the energy loss is caused by plasmon and phonon scattering. The term "high loss" is conventionally used to describe core loss EELS.
Subtle variations in intensity can be observed at the core loss edges, referred to as EELS fine structure or electron energy loss near-edge structure (ELNES). These terms will be used interchangeably. The features of the ELNES represent unoccupied states which the inner shell electron is excited to in a core loss event. Several factors can influence the energy and density of these unoccupied electronic states, seen as changes in the ELNES. The ELNES is therefore sensitive to the local chemical and electronic environment of the atom. In the context of this thesis work, the EELS fine structure is useful to study the oxidation state of B cations and the presence of oxygen vacancies in the samples.
One constraint on the energy resolution in EELS is the energy spread of the incident beam. Cold Field Emission Guns (CFEG) can produce a beam of electrons with a narrower energy distribution, making them preferable over traditional electron guns [39]. The *JEOL ARM200F*, which was employed in this study, utilizes a CFEG. In the EEL spectrum, the peak representing the transmitted beam is referred to as the zero loss peak (ZLP). The energy spread of the incident beam is represented by the full width at half maximum (FWHM) of the ZLP. To observe fine structure features, a FWHM typically below 1 eV is required [40].
STEM-EELS is done by scanning the sample with a STEM probe and recording the EEL spectrum at each scan position. Thus, local chemical and electronic variations in the sample can be compared. An effect which can impact the spatial resolution of the EELS signal is electron channelling. This phenomenon causes the electrons to spread to adjacent atomic columns, interacting with a larger volume of the sample, leading to a decreased spatial resolution of the EELS signal. To suppress the effects of electron channeling, MacArthur et al. proposed introducing a sample tilt 1 - 2°off zone axis

during acquisition [41].

2.3.2 Oxidation state and oxygen vacancy detection in EELS

The exchange mechanisms responsible for the magnetic properties in LSMO and LFO are influenced by two central factors; the oxidation state of the B cation and the presence of oxygen vacancies. Both of these properties can be studied with fine structure EELS. The B cations considered in this work are Mn in LSMO and Fe in LFO. For convenience, Mn and Fe will be collectively referred to as Transition Metals (TM), and the Mn-$L_{2,3}$and Fe-$L_{2,3}$ edges will be referred to as TM-$L_{2,3}$ edges. The term B cation will also be used about Mn and Fe when it is important to underline the position of the TM in the perovskite oxide unit cell. The following section will give the theoretical background necessary to interpret spectral features in EELS which are indicative of changes to the oxidation state of the B cation and the presence of oxygen vacancies. Information about the TM-$L_{2,3}$ edge is based on the article "Oxidation state and chemical shift investigation in transition metal oxides by EELS" by Tan et al. [42], and the section describing the O-K edge is based on "Effects of Multiple Local Environments on Electron Energy Loss Spectra of Epitaxial Perovskite Interfaces" by Lawrence et al. [43].
Generally, the formation of oxygen vacancies is expected to occur simultaneously with a lowering of the cation oxidation state to maintain charge neutrality in the compound [44, 45]. As these properties are normally related, it is useful to study signs of oxygen vacancies and changes in oxidation state simultaneously. The TM-L_3 and -L_2 peaks originate from the $2\,p^{1/2} \rightarrow 3d$ and $2\,p^{3/2} \rightarrow 3d$ transition respectively. The O-K edge originates from the transition from 1s $\rightarrow$ hybridized states with the TM cation. In LSMO and LFO, this hybridization is between 2p electrons from oxygen and 3d electrons in the TM. The O-K, Mn-$L_{2,3}$ and Fe-$L_{2,3}$ edges are shown in Figure 2.7.

Mn-$L_{2,3}$ and Fe-$L_{2,3}$ edges

Traditionally, two main methods are used to study the TM oxidation state using the TM-$L_{2,3}$ edge. The first is the white-line ratio method and the other is the chemical shift method. For clarity, a higher oxidation state refers to a higher nominal charge, so that the oxidation state of Mn^{4+} is higher than the oxidation state of Mn^{3+}.
The application of the white-line ratio in Mn and Fe has been thoroughly studied by Tan et al. [42]. The white-line ratio relates the integral intensity ratio of the TM-L_3 and -L_2 peaks to the formal TM oxidation state. For Mn, a monotonic decrease of the white-line ratio corresponds to an increasing oxidation state due to a systematic increase of the L_2 intensity relative to the L_3 intensity. The $L_{2,3}$ peaks of Mn and Fe are shown in Figure 2.7. As LSMO contains a mix of Mn^{3+} and Mn^{4+}, the Mn-$L_{2,3}$ edge is expected to show a combination of Mn^{3+} and Mn^{4+} features.
The work done by Tan et al. also revealed that no monotonic relation exists between the white-line ratio and oxidation state of Fe, indicating that the white-line method is unsuitable to determine the nominal oxidation state of Fe in ferrite oxides. However, observing relative changes in the white-line ratio of Fe-$L_{2,3}$ within a compound could

provide clues about relative changes in oxidation state. The white-line ratio of Fe-$L_{2,3}$ is addressed further in Section 6.2. The chemical shift method relates the ionization edge onset of the TM-L_3 edge to the TM oxidation state. This method is applicable to both Mn and Fe. A systematic chemical shift to higher ionization edge energy onsets is correlated to an higher oxidation state. This is called "the chemical shift rule" [42].

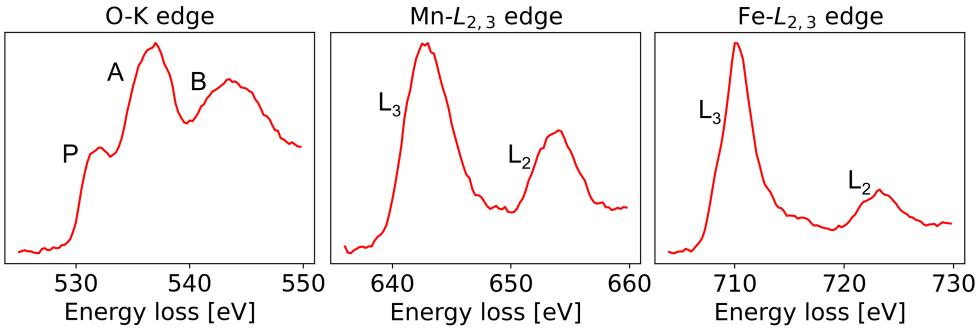

Figure 2.7: O-K edge ELNES with annotated sub-peaks, Mn-$L_{2,3}$ and Fe-$L_{2,3}$ peaks respectively.

O-K ELNES

In perovskite oxides, the O-K edge is affected by variations in both the initial states of oxygen and the final states of the cations, including the oxidation state of the TM cation. Unlike the TM-$L_{3,2}$ edges, the O-K edge is therefore sensitive to variations in the coordination environment and bonding with the surrounding cations, which can be influenced by changes in the cation oxidation state and the presence of oxygen vacancies, as well as changes in octahedral tilt and strain. The O-K edge onset energy is expected to decrease with increasing oxidation state of the TM [42].
The well-understood physical origins of the P, A and B sub-peaks in the ELNES at the O-K edge make them powerful tools in EELS studies of transition metal oxides. See Figure 2.7 for an illustration of the O-K sub-peaks. The pre-peak (P), represents the bonding between O 2p orbitals and B cation 3d orbitals. The first main peak, A, arises from the interaction between O 2p orbitals and the A cation (La (5d) and La (5d)/Sr (5s) in LFO and LSMO, respectively). The second main peak, B, reflects the hybridization of oxygen with the 3s and 3p orbitals of the B cation [43]. Specifically, a simultaneous decrease of the P and B peak intensity is normally interpreted as a sign of oxygen vacancies. This feature is also associated with a a reduced B cation oxidation state. A lowering of the intensity of the full O-K edge is also associated with oxygen vacancies. Previously, it has been argued that a lowering of the P-peak intensity is associated with strain, due to a lowering of the orbital overlap between O and the B cation. In their work, Lawrence et al. [43] found that the sub-peak intensities and O-K edge onset only changed very subtly as a response to strain, and that chemical and electronic effects had a more significant impact on the features of the O-K ELNES. The core loss edge energies used in this work are included in Table 2.2.

Table 2.2: Atomic number, valence and experimental core loss edge onset of the elements in the samples, in order of increasing ionization edge onset energy [46].

Element	**Z**	**Valence**	**EELS edge onset [eV]**
Sc	21	+3	$L_{2,3}$: 402
Ti	22	+4	$L_{2,3}$: 455
O	8	-2	K: 532
Mn	25	+3.3	$L_{2,3}$: 640
Fe	26	+3	$L_{2,3}$: 708
La	57	+3	$M_{4,5}$: 832
Dy	66	+3	$M_{4,5}$: 1295
Sr	38	+2	$L_{2,3}$: 1940

Chapter 3

Materials and Methods

3.1 Sample preparation

The superlattices were grown with pulsed laser deposition (PLD) by Yu Liu and Ingrid Hallsteinsen at the Department of Materials Science and Engineering at NTNU, using a *Mantis Deposition PLD*. Liu cut both samples into cross-section TEM lamella using a focused ion beam (FIB) lift-out technique with a *Helios G4 UX* FIB. The two samples were cut with a 90°angle difference. Descriptions of the PLD growth parameters were provided by Liu, and can be found in Appendix A.

3.2 Instruments

4D-STEM experiments such as SED, SPED and S-SPED were conducted using a *JEOL JEM2100F* equipped with a NanoMEGAS DigiSTAR precession scan generator and a Quantum Detectors MerlinEM direct electron detector. HRTEM, EELS and STEM-HOLZ acquisition was done with a *JEOL ARM200F* instrument. Both instruments were operated at 200 kV acceleration voltage. HRTEM images were acquired with a Gatan Rio CMOS 4K camera. STEM-HOLZ data was acquired by conducting a conventional STEM scan with a high convergence angle using a NanoMEGAS DigiSTAR scan generator and detecting the diffraction patterns using a Quantum Detectors MerlinEM Direct Electron Detector. STEM-EELS was detected with a Gatan GIF QuantumER detector, and overview images recorded simultaneously using Gatan HAADF and Gatan BF/DF detectors.

3.3 Crystallographic analysis

HRTEM, FFT and S-SPED experiments were conducted in order to characterize the crystal structures found in the superlattices. S-SPED was used to probe the diffraction patterns from different regions in the sample in order to understand the local crystal structures in the superlattices. This was done by inspecting diffraction patterns from

single probe positions, and by summing diffraction patterns from all probe positions within a selected region of interest (ROI). Note that summing diffraction patterns from ROIs was only undertaken when it was evident that different patterns would not be mixed in the summation process. The diffraction analysis was complemented with VDF imaging by applying virtual apertures to selected diffraction spots, in order to map the sample regions scattering electrons to specific reflections. This enabled the simultaneous identification of distinct diffraction patterns and the sample regions from which they originated. HRTEM images were used to inspect the appearance of the atomic lattice. FFTs from different regions of interest in the HRTEM images were generated to detect changes in the atomic lattice frequencies in HRTEM images. FFT images were compared with S-SPED patterns in order to relate the features found in virtual images to those found in HRTEM images. FFTs and S-SPED reflections were indexed based on simulated diffraction patterns of the materials in the superlattices using ReciPro [47]. For convenience, all S-SPED and FFT indices were given in the pseudocubic system. Comparison of S-SPED and HRTEM FFTs was done while keeping in mind that S-SPED and FFT patterns are generated in completely different ways, and represent different phenomena. 4D-HOLZ-STEM was conducted in order to detect changes in the atomic lattice along the electron beam direction in one of the superlattices. An annular virtual aperture was used to select electrons scattered to specific HOLZ rings to generate VDF images. Crystal visualization software and diffraction simulations were used to identify crystal orientations and relate structures both within each sample, and features in the two samples to each other. See Section 3.5 for more information about crystal structure visualization and diffraction simulations tools.

3.4 STEM-EELS

STEM-EELS was recorded along line scans traversing the superlattice layers from the substrate to the protection layer. By comparing the spectral features from different scan position along the scan line, information about the relative chemical composition, oxidation state of Mn and Fe, and oxygen vacancies in different sample regions was studied. Analysis of the relative intensity of the core loss edges was used to probe the relative chemical composition in the samples. The white-line ratio of the Mn-$L_{2,3}$ and Fe-$L_{2,3}$ edges, and the ELNES of the O-K peak were studied for information about TM oxidation states and oxygen vacancies.
The core loss energies of the elements in the samples ranged from 402 eV (Sc-L_3) to 2007 eV (Sr-L_2) in $(LSMO/LFO)_4$/DSO and 456 eV (Ti-L_2) to 2007 eV (Sr-L_2) in $(LSMO/LFO)_{10}$/STO. See Table 2.2 for all core loss energies. To acquire all interesting core loss energies in one EELS line scan, a somewhat unconventional method was utilized. Instead of recording the electron energy loss beginning at 0 eV, the full energy detection range was shifted to higher energy losses in order to include all interesting core loss energies. This allowed for simultaneous acquisition of a "low energy regime" and "high energy regime" core loss spectrum, thus covering the full range of core loss energies of the sample compounds. Figure 3.1 shows the low and high energy regime

spectra recorded simultaneously using this method. EEL spectra from the substrate and superlattice regions are included to illustrate how a unique spectrum is recorded for each probe position along the line scan.
The method of shifting the detected energy range came at the cost of precise energy calibration. Conventional energy calibration in EELS is done by setting the energy at the ZLP to 0 eV [48]. This could not be performed in the recorded spectra, as the ZLP was not included in the recorded energy ranges. Instead, ionization edge onset energies were used for energy calibration. Core loss edges likely to undergo chemical shifts as a response to local structural and chemical conditions, such as the TM-$L_{2,3}$ and O-K edges, were not used for calibration. However, no ionization edge has an absolute energy onset, and it was kept in mind that this calibration technique was less robust compared to using the ZLP.

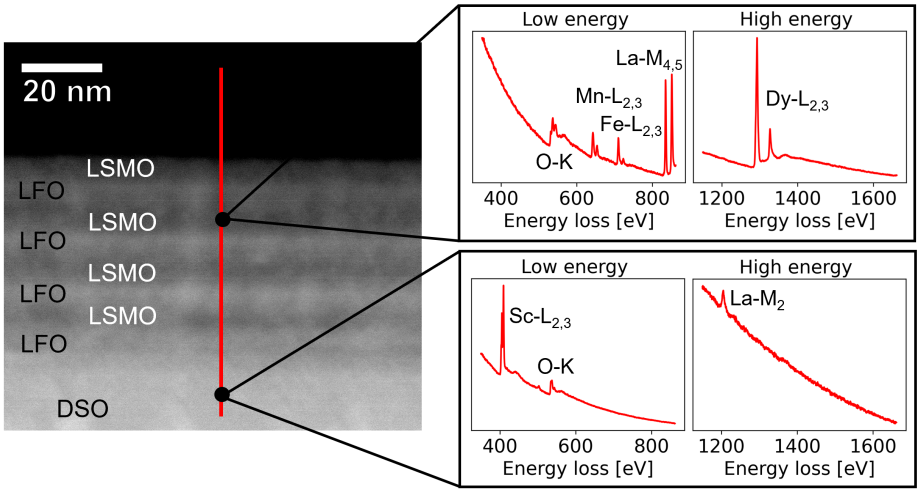

Figure 3.1: STEM-HAADF overview image of $(LSMO/LFO)_4/DSO$ with a red line representing the EELS line scan. EEL spectra with "low and high" energy regimes from the DSO substrate and the superlattice are included. The scan points where the spectra were generated are marked with black circles.

The terms "low and high energy regime" are not to be confused with the terms "low loss" and "high loss" conventionally used in EELS. All EELS analysis conducted in this work was high loss EELS. The "low energy regime" ranged from 350-860 eV for $(LSMO/LFO)_4/DSO$ and 400-900 for eV for $(LSMO/LFO)_{10}/STO$, while the "high energy regime" was 1150-1660 eV for $(LSMO/LFO)_4/DSO$ and 1650-2200 eV for $(LSMO/\ LFO)_{10}/STO$. The STEM-HAADF images acquired alongside STEM-EELS were recorded with collection angles 118.5 - 470.9 mrad. The dispersion was set to 0.25 eV per channel in both EELS acquisition sessions. To limit the effects of channelling, a sample tilt of 1°off zone axis was introduced, as suggested by MacArthur and her colleagues [41]. Energy dispersive X-ray (EDS) detection was performed simultaneously with EELS. EDS was excluded from further analysis as it did not provide additional

information about the samples beyond what was obtained from EELS.

3.5 Data processing

EELS and S-SPED data processing was done using the open source python library HyperSpy and Pyxem [49, 50]. Particularly memory intensive operations were run on the NTNU high performance computing (HPC) cluster IDUN [3] for increased processing efficiency. Digital Micrograph [51] was used for inspection of HRTEM and STEM-EELS results prior to data processing, as well as FFT generation from HRTEM images. Crystal structures were visualised using Vesta [25], and diffraction patterns were simulated in ReciPro [47]. Ideally, as both kinematic and dynamic scattering effects contribute in diffraction imaging of the the superlattices, MultiSlice simulations [52], using dynamic scattering theory should have been performed. However this was not conducted due to time constraints, and kinematic ReciPro [47] simulations were performed instead. In these simulations all spot intensities are represented equally, and extinct reflections are included and marked with red. As chapter 4 is dedicated to S-SPED, details on S-SPED data processing can be found there. The following section outlines EELS data processing only. HyperSpy was used for analysis of STEM-EELS data. The pre-processing steps included pre-edge background subtraction and removal of high-energy radiation peaks. The specifics of the initial processing procedures are detailed below. After initial processing, the relative intensities of the core loss edges were plotted for chemical composition analysis, and the white-line ratios of TM-$L_{2,3}$ edges and O-K edge ELNES were studied for information about TM-oxidation state and oxygen vacancies in the samples.

Two built-in functions were utilized in the pre-processing steps of the EELS data analysis. Some of the datasets were subject to external radiation, such as cosmic rays, impinging on the EELS detector during acquisition. The resulting high energy spikes in the EEL spectra were removed using HyperSpy's built-in interactive `spikes_removal_tool()` function [53]. The threshold values were adjusted to differentiate between EELS peaks and external radiation peaks.

Conventionally, the EELS background is removed by fitting a power-law to the pre-edge region, and subtracting this from the spectra [54]. In this work, a model-based approach was used for pre-edge background removal. Instead of fitting a power-law to the spectrum, a model was fitted to the EEL spectrum based on a physical approximation. The model based approach is generally considered more precise than the conventional method [54]. The model consists of several separate components representing each element and its core loss and fine structure features. For each core loss edge, the component of the model representing that edge was deactivated, and the rest of the model was subtracted from the EEL spectrum. In this way, the background and energy loss contributions from all other elements in the sample were subtracted from the EEL spectrum, and only the relevant core loss edge remains. This was done using the built-in HyperSpy EELS curve fitting function `multifit()` [55]. The fitting procedure was run on the IDUN HPC cluster.

The `multifit()` function utilizes a hydrogenic Generalized Oscillator Strength (GOS)

approximation to create the model [55]. This method can only model K- and L-edges [56]. Model based background subtraction could therefore not be applied the La-$M_{4,5}$ and Dy-$M_{4,5}$ edges. Background removal for these edges was instead conducted by conventional power-law fitting and subtraction. EELS background subtraction procedures are further addressed in Section 6.2.

Chapter 4

Development of Segmented SPED

The following chapter will give a complete account of the development and testing of the S-SPED methodology conducted in this work.

4.1 Principle behind S-SPED

The information presented in the following section is from the publication "Correcting for probe wandering by precession path segmentation" by Nordahl et al. [15], as well articles by Vincent et al. and Barnard et al.[14, 33]. Individual citations will not be given.
As outlined in Section 2.2.3, the electron beam can move outside of the aberration free region of the ronchigram during SPED acquisition. This leads to a periodic deflection of the beam by spherical aberrations in the probe forming lenses called probe wandering. When probe wandering is integrated at each scan position during precession, the result is a larger effective probe size and a loss of spatial resolution compared to non-precessing techniques such as NBD-SED. When imaging nanoscale structures such as the superlattices studied in this work, minimizing the probe size is critical to obtain the most localized diffraction data possible. Reduced spatial resolution due to probe wandering is therefore unfortunate. On the other hand, precessing the electron beam is necessary to obtain high quality diffraction patterns. S-SPED is proposed as a new methodology to achieve both high quality diffraction data and high spatial resolution by minimizing the effect of probe wandering.
The principle behind S-SPED involves dividing the precession path into multiple segments. This is done by capturing n frames for each azimuthal rotation of the electron beam, generating n individual SPED datasets, referred to as segment slices. The magnitude of the probe wandering is equal but directionally different between each segment due to the isotropic nature of the spherical aberrations in the probe forming lenses. Therefore, the probe is displaced radially outward from the optical axis based on where the beam is on the precession azimuth. By segmenting the precession path into n segment slices, the effect of probe wandering is seen as shifts of the the position of imaged features varying across the segment slices in a circular motion.
With S-SPED correction, these relative feature shifts can be counteracted by rigidly

correcting their movement. Practically, this means aligning the positions of recognizable features between each segment. Effectively, this rigid correction procedure is equivalent to virtually relocating the electron beam closer to the center of the scan point, making the time-averaged probe smaller. The final corrected S-SPED dataset is created by combining the aligned segment datasets. This gives a smaller effective probe size than in conventional SPED, and improved spatial resolution.
With few segments, more probe wandering is integrated into each segment, leading to more precession-induced blur in individual segments. Consequently, the maximum achievable resolution improvement is determined by the number of acquired segments, n. It should also be pointed out that S-SPED correction can improve resolution compared to SPED, but never enhance resolutions beyond what is achievable with NBD-SED.
Resolution improvement by application of S-SPED has been demonstrated in VBF images by Nordah et al. [15]. However, S-SPED correction can also be applied to the diffraction dimension of the 4D-dataset. This was done for the first time in this work. When the diffraction patterns generated from a large time-averaged probe are integrated during precession, the structural information in the resulting diffraction image originates from a larger region of the sample, making crystallographic analysis of small features impossible. Conversely, by reducing the effective size of the electron probe by minimizing probe wandering with S-SPED, the information in diffraction patterns in the corrected dataset become more localized. The S-SPED correction process is shown schematically in Figure 4.3. This illustration also highlights the impact of S-SPED correction on diffraction pattern quality. The term "higher reciprocal space resolution" will be used to describe the localization of diffraction information achieved with S-SPED correction.

4.2 S-SPED method

4.2.1 Experimental acquisition

S-SPED data was acquired with a*JEOL 2100F* operating at a 200 kV acceleration voltage, using a NanoMEGAS DigiSTAR precession scan generator and a Quantum Detectors single chip MerlinEM direct electron detector. Precession alignment was done following the method described by Barnard et al. [14], and S-SPED acquisition was done based on the description detailed by Nordahl et al. [15]. A 0.5 nm NBD probe was used with a 1.185 mrad convergence semi-angle. The precession angle was 1.0°or 17.5 mrad, and the precession frequency was set to 100 Hz. The camera length (CL) was 22.95 cm. With a 100 Hz precession frequency, one full azimuthal rotation of the beam takes 10 ms, while the minimum detector read-out time is 0.617 ms, assuming 12 bit imaging. Theoretically, this means that any number of segments below $n = 10/0.617 = 16.21$ can be detected continuously without missing any azimuthal rotation angles. Datasets with $n = 4$, 8, and 16 segments were collected to examine the influence of and determine an optimal number of segments. In all cases, the dwell time was set to 10 ms to allow one rotation of the beam between each scan point. Figure 4.1 shows

images of the segments of intensity integration of the segmented precession path and diffraction images with $n = 8$ segments.

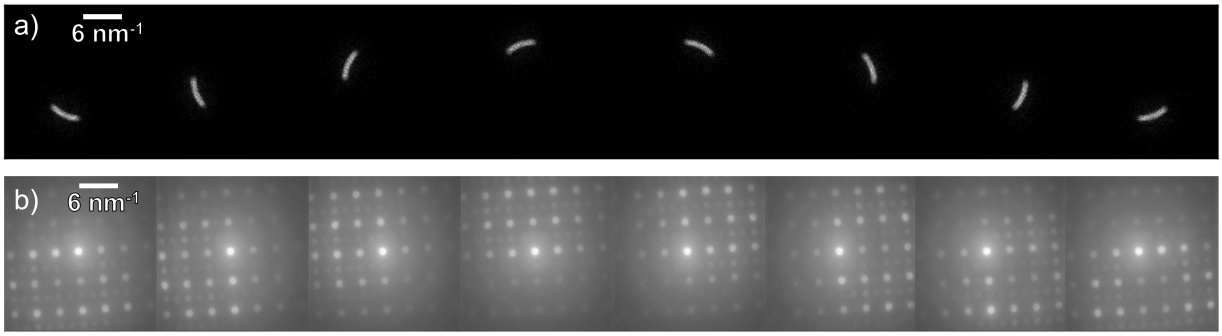

Figure 4.1: a) Images of the electron beam in each of the $n = 8$ segments. The images are recorded during a segmented scan with precession de-rocking turned off, in an amorphous sample region. This showcases the $n = 8$ segments of intensity integration captured for each azimuthal rotation of the electron beam. b) Images of the diffraction patterns recorded with precession de-rocking turned on from at a crystalline sample region. Due to the difference in the incident beam angle in the segments, the position of the Ewald sphere shifts between the segments. This appears as a circular illumination of sections of the diffraction pattern.

The number of Y scan points was set to either 128 or 160 depending on film thickness, and all X scan points (points per scan line) set to 256. To perform path segmentation, the number of X scan points had to be multiplied by n and the frame time divided by n. An 8 segment scan therefore had X points $256 \cdot 8 = 2048$ and frame time $10/8 = 1.25$ ms. As the 8 segments are represented as scan points in the X direction, this causes the raw data to appear 8 times wider in X. An image of the raw data and the individual segment images can be seen in Figure 4.2. Correspondingly, 16 segment scans had X points = 4096 and frame time = 0.625 ms. The scanner flyback delay was increased to 250 ms. In addition to this primary data collection, 11x11 point scans with precession de-rocking turned off were routinely carried out to inspect the ellipticity of the precession path and measure convergence and precession angles.

Intentionally misaligned data

In order to evaluate the potential of counteracting misalignment through S-SPED correction, several S-SPED datasets were acquired with intentional instrument misalignment. All deliberately misaligned scans were recorded with $n = 8$ segments. Pivot point misalignment was introduced by adjusting the amplitude of the scan coil 0.2% with respect to a correct SPED alignment in the Y direction. Misalignment of the pivot point in the Y direction was anticipated to induce probe shifts, and thus increase blur in the vertical direction of the VBF images. This choice was made intentionally, as vertical movement of the superlattice interfaces was more straightforward

to detect and correct compared to horizontal movement.
Another S-SPED dataset was recorded with the sample moved away from the focus point. This was done by moving the sample downward parallel with the beam direction using the goniometer while monitoring VBF images acquired with NBD-SED until significant blur was observed. This was expected to give significant probe shifts in SPED.

S-SPED alignment

An important distinction should be made at this point. Unless otherwise indicated, all datasets were acquired with the best possible alignment achievable for a master student spending a reasonable amount of time on TEM and SPED alignment. This will be referred to as "as good as possible" alignment. However, the TEM and SPED alignment could most likely have been further fine-tuned by performing a greater number of iterative alignment steps. It is therefore plausible that some misalignment contributes to probe shifts even in the "as good as possibly" aligned S-SPED datasets. In order to test the resolution improvement potential on a "perfectly" aligned S-SPED dataset, highly experienced SPED operator Emil Frang Christiansen conducted TEM and SPED alignment unusually meticulously in an experiment dedicated to this. This specific dataset will therefore be described as "perfectly aligned", while all other datasets acquired independently will be described as "as good as possibly" aligned. It is important to keep in mind that the former demanded much stricter alignment and was more time consuming, while the latter resulted from typical alignment procedures.

4.2.2 Post-acquisition data processing

S-SPED correction and further data analysis was conducted using the open-source Python libraries HyperSpy [49] and the HyperSpy extension Pyxem [50]. Given the substantial amount of data collected in this study, comprising over thirty SPED, S-SPED, and NBD-SED datasets, each ranging from 20 to 80 GB, the majority of this data was stored on the NTNU HPC cluster, IDUN [3]. In addition to data storage, IDUN was employed for tasks requiring significant computational resources, such as data conversion and other memory-intensive operations. All processing code is included in Appendix D, and the processing steps are described below.
For clarity, the images depicted in Figure 4.2 a) and b) are not purely VBF in nature, but are reconstructed from electrons scattered across the full range of angles on the detector. Consequently, diffracted electrons also contribute to the contrast in these images. However, given that the majority of detected electrons are transmitted rather than scattered, bright-field (BF) is the dominant contrast mechanism. For ease of discussion and to reflect this predominance, these images will be referred to as VBF reconstructions. Figure 4.2 a) shows the raw data of a $n = 8$ segments dataset, and Figure 4.2 b) shows the first processing step of slicing the data into $n = 8$ segment slices.

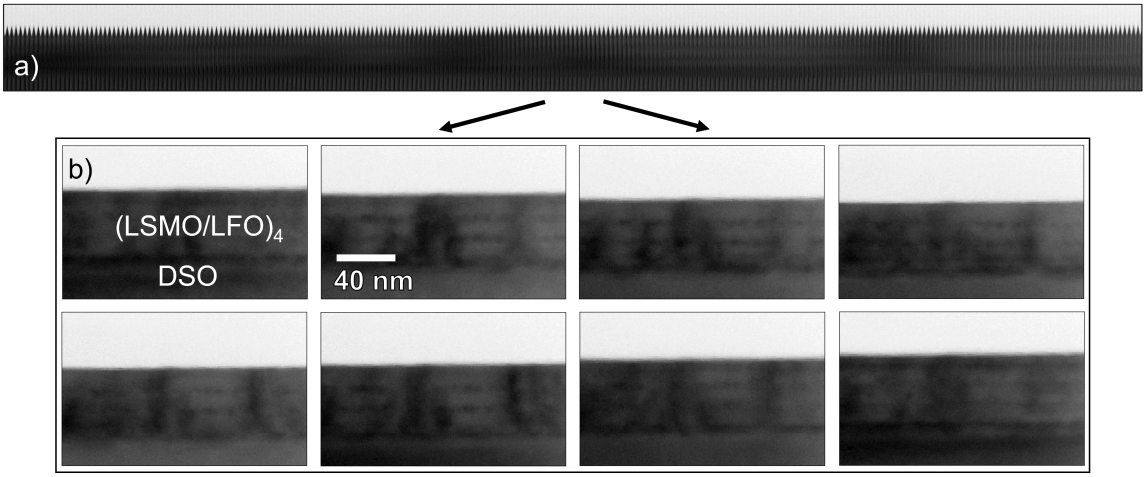

Figure 4.2: a) VBF of a $n = 8$ segment S-SPED dataset prior to segment slicing, showing the raw data as it appears during acquisition. b) VBF images of the same dataset sliced into 8 segments. The shifts of the position of the superlattice between segments are caused by probe wandering.

The effect of probe wandering is seen as small shifts, predominantly in the Y direction, in Figure 4.2 b). The fundamental purpose of S-SPED is to manipulate the data to counteract these shifts. Alignment of the segment slices was performed by generating VBF images from each segment slice and creating a stack of these images. In Figure 4.2 b), each VBF image represents a full SPED-dataset. However, the initial alignment steps were conducted using only a VBF image from each segment, as this was significantly more memory efficient than aligning probe positions and diffraction patterns in full SPED-segments. The feature shifts between the VBF images were detected manually, and a list of counteractive shifts was generated. The built-in HyperSpy function `align2D()` [57] was used to apply these shifts to each VBF in the stack. The VBF images were summed in order to inspect the resolution improvement resulting from the rigid alignment. The alignment procedure of VDF images is illustrated schematically in Figure 4.3 b) and c).
The correcting probe position shifts found in the previous step were applied to both real and reciprocal dimensions of the data by shifting both the probe positions and their associated diffraction patterns within the 4D-data structure of each segment slice. This was done using the function `da.roll()` [58], which moves data points in an array to the opposite edge of the dataset, as illustrated by red probe positions in Figure 4.3 c). A corrected S-SPED dataset was created by averaging the corrected segment datasets, while the equivalent to a non-corrected SPED dataset was produced by averaging the uncorrected segment datasets. This was done in order to assess the resolution improvement achieved with S-SPED correction. The rolled probe positions were cropped out of the corrected dataset.
In the schematic in Figure 4.3, virtual bright-field (VBF) images are illustrated as a grid of scan points. The black scan point represents a crystalline feature, and the gray background represents amorphous sample regions.

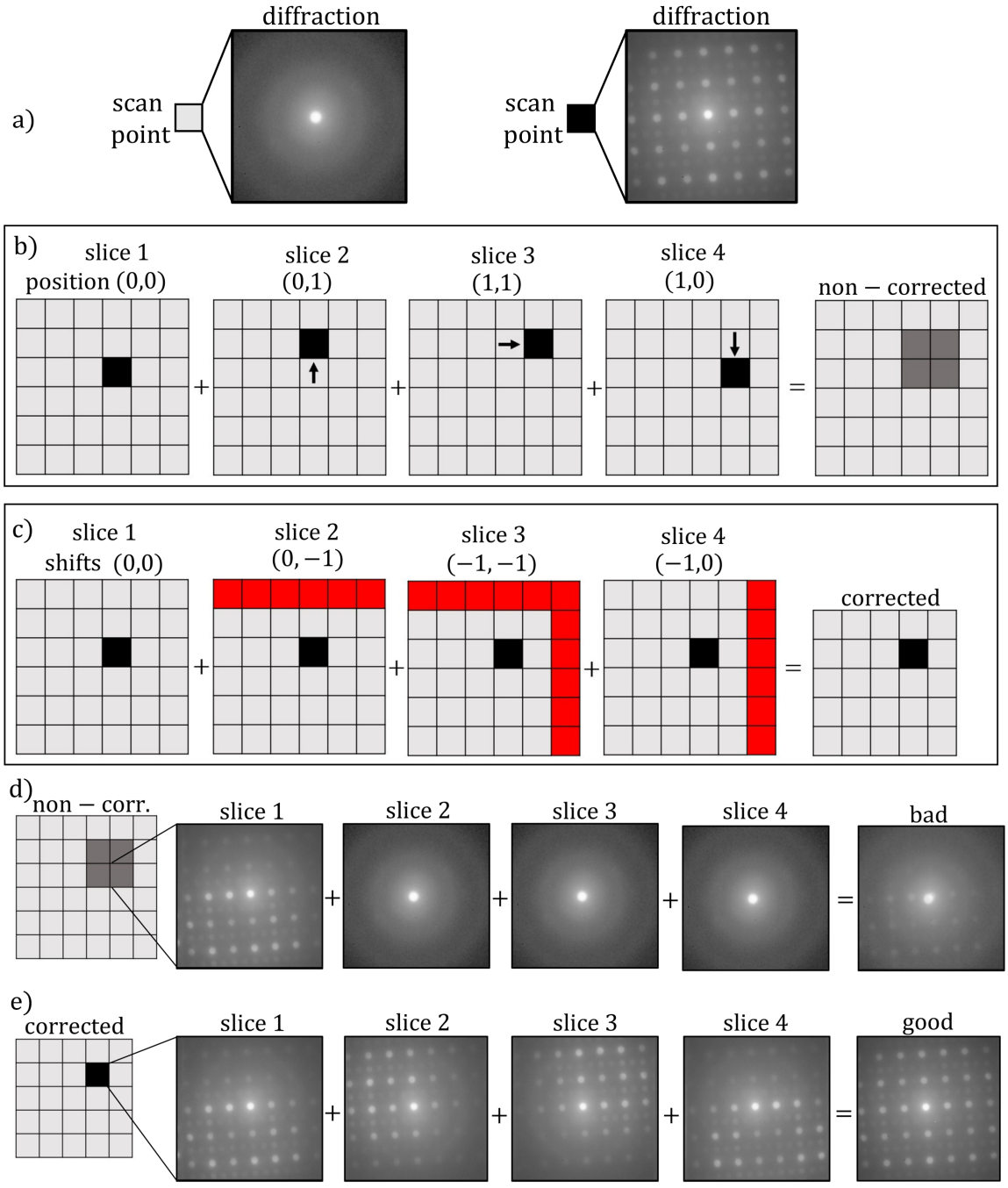

Figure 4.3: a) The diffraction patterns associated with gray (amorphous) and black (crystalline) grid points. b) Non-corrected segments combined to a final image where the crystalline feature appears larger than in each segment. c) Introduction of correctional shifts counteracting the effects of probe wandering by "rolling" probe positions in the datasets. "Rolled" positions are represented in red. The feature is not blurred when combining the segments. d) "Bad" or ambiguous final diffraction pattern due to integration of diffraction patterns from both crystalline and amorphous regions. e) "Good", or unambiguous final diffraction pattern, due to integration of diffraction patterns from only the crystalline region.

In Figure 4.3 b), probe wandering is seen as circular movement of the black feature between the segment's VBF images. It should be noted that this feature shift is exactly one scan point. In real experiments, it is not likely that the relative probe motion is equal to an integer number of scan positions. Therefore, achieving a resolution which is identical to that of single segments is not realistic in S-SPED.
Figure 4.3 b) and c) show how spatial resolution is enhanced by shifting the probe positions by "rolling the data" to counteract probe wandering. In the corrected dataset in Figure 4.3 c), the black feature is the same size as in single segments, while it is four times larger in the non-corrected dataset in Figure 4.3 c). On the other hand, Figure 4.3 d) and e) demonstrates how the reciprocal space resolution is enhanced by applying S-SPED correction. In the uncorrected dataset, diffraction patterns from both crystalline and amorphous sample regions are combined, giving ambiguous diffraction information (denoted as "bad"). This is analogous to intensity integration with a larger time averaged probe size due to probe wandering. In the corrected dataset, the final diffraction image is combined of segment diffraction patterns from aligned probe positions, and the information in this diffraction pattern is therefore unambiguous (denoted as "good").
Generation of VDF images has been conducted in order to assess reciprocal space resolution improvements in S-SPED data. Diffraction reflections used for VDF generation have been selected in order to differentiate between the superlattice layers. If the diffraction patterns are mixed, as illustrated in Figure 4.3, there will be no VDF contrast between the layers. Conversely, if distinct layers are resolved in the S-SPED data, the superlattice layers will display different VDF contrast, due to distinct or "unambiguous" diffraction patterns. In $(LSMO/LFO)_{10}/STO$, this has been done by selecting the edge of a diffraction reflection known to shift within layers, $(111)_{pc}$. VDF contrast in images of $(LSMO/LFO)_{10}/STO$ therefore showcases subtle changes in unit cell parameter through the layers. In $(LSMO/LFO)_4/DSO$, reflections exclusive to LFO have been selected for VDF generation. As this section does not address crystallography, specifics about diffraction patterns will not be given, other than descriptions of the contrast mechanisms seen in VDFs. Diffraction results from S-SPED analysis are presented in Section 5.2.3.
Another resolution assessment approach used in this work is intensity line scan plotting across interfaces with different contrast. The steepness of the intensity line across these interfaces has been used to qualitatively assess the resolution in virtual images. The maximum shifts introduced in S-SPED corrections will be given in order to quantify the probe motion in the different datasets. The direction of these shifts will be given with X and Y coordinates, corresponding to the horizontal and vertical directions in the images, respectively.

4.3 Results of S-SPED correction

Figure 4.4 a) shows VBF images from SED, SPED, and S-SPED ($n = 8$ and $n = 16$) scans, all acquired with the same experimental setup. Noticeably, the interface between the superlattice and the amorphous protection layer is significantly more blurred in the SPED VBF than in the NBD-SED VBF. This is due to probe wandering. The increased spatial blur in SPED compared to NBD-SED is reflected in the intensity line scan in Figure 4.4 b), where the black line representing NBD-SED has a steeper slope than the dashed red line representing SPED VBF. In S-SPED-corrected VBF images of 8 and 16 segment S-SPED, this interface is considerably sharper than in SPED. The intensity line profiles form the corrected S-SPED data is also significantly steeper than the original SPED line. However, the NBD-SED image is still sharper and has the steepest line profile slope of the four images in Figure 4.4. This emphasizes that while S-SPED can enhance resolution over SPED, it cannot surpass the resolution achievable with NBD-SED.

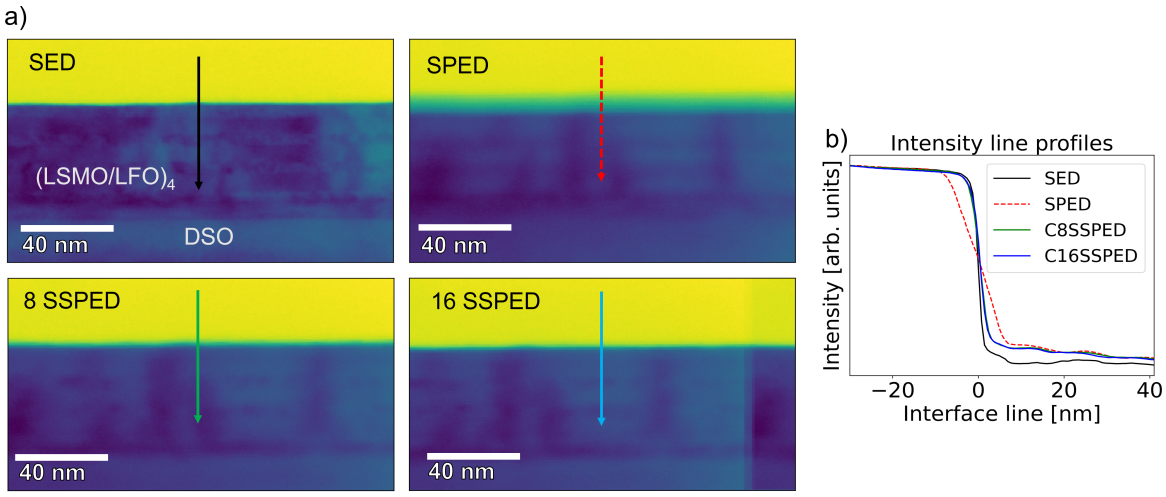

Figure 4.4: a) VBF images of NBD-SED, SPED, $n = 8$ and $n = 16$ segment S-SPED datasets of $(LSMO/LFO)_4/DSO$ recorded under identical acquisition conditions. Arrows mark the path of the intensity line profile plot. b) Intensity line profiles measured across the indicated lines in the VBF images.

As seen in the $n = 16$ segment S-SPED VBF, a portion of the scan appears to have moved to the opposite side of the image. This was seen in the raw data, and the reason for this is unidentified. As the scan is largely unaffected by this artefact, it is still useful for analysis. The maximum shifts introduced to the VBFs with S-SPED corrections was 8.9 nm for $n = 8$ and 10.9 nm for $n = 16$, both in the X direction.
It should be noted that all virtual images from the same scan exhibit the same spatial resolution. However, the contrast seen in VDFs specifically demonstrates how applying S-SPED corrections to the reciprocal space dimension localizes the information in the corrected diffraction patterns. In the following section, virtual apertures has been

used to create VDF images of the superlattices. Diffraction spot selection was done to achieve different VDF contrast between the two superlattices. Images of the specific diffraction patterns and virtual apertures can be found in Section 5.2.3.

Figure 4.5 shows VDF reconstructions of corrected and non-corrected S-SPED datasets of $(LSMO/LFO)_4/DSO$ and $(LSMO/LFO)_{10}/STO$. Both datasets are acquired with "as good as possible" alignment.

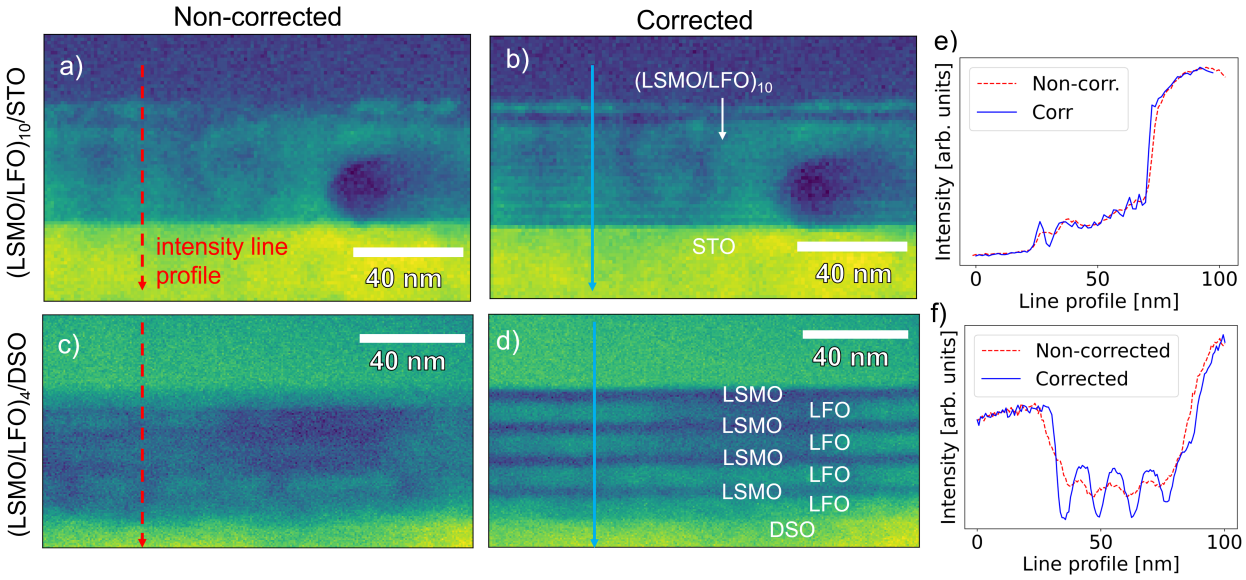

Figure 4.5: a)-d) VDF image of $(LSMO/LFO)_4/DSO$ and $(LSMO/LFO)_{10}/STO$ before and after applying S-SPED correction to a $n = 8$ segment scan. e)-f) Intensity line profiles traversing the superlattices for comparison of corrected and non-corrected VDF image contrast.

The maximum correctional shifts applied to the data in Figure 4.5 was 4.3 nm (in Y) for $(LSMO/LFO)_{10}/STO$ and 8.9 nm (in X) for $(LSMO/LFO)_4/DSO$. For $(LSMO/LFO)_4/DSO$, the VDF was generated by selecting the reflection between the $(000)_{pc}$ and $(1\overline{1}1)_{pc}$ spot, which is exclusively found in LFO and DSO. DSO and LFO appears bright in the VDF, while LSMO appears dark. For $(LSMO/LFO)_{10}/STO$, the VDF was generated by selecting the edge of the $(111)_{pc}$ spot. The observed contrast in Figure 4.5 a) and b) can most likely be attributed to small variations in the lattice parameter between the LSMO and LFO in the $[111]_{pc}$ direction.

The non-corrected VDFs in Figure 4.5 a) and c) are too blurred to allow for the differentiation of individual superlattice layers. In the corrected VDFs in Figure 4.5 b) and d), the contrast between LSMO and LFO is significantly stronger. This improvement is also evident in the line profiles in Figure 4.5 e) and f), where the uncorrected profile (red) is flat, while the corrected profile (blue) has large variations in intensity across the superlattice. The observed enhancement in VDF contrast, particularly in the thin layers of $(LSMO/LFO)_{10}/STO$, shows that the resolution improvement enables the investigation of diffraction patterns originating from individual superlattice layers. This is not feasible with the non-corrected datasets, representing conventional

SPED. Another useful way to assess the effect of S-SPED correction is by inspecting diffraction patterns from equivalent probe positions in corrected and non-corrected datasets. This is shown in Figure 4.6 a) and b).
The diffraction image from region (1) in Figure 4.6 a) contains contributions from both crystalline and amorphous sample regions. On the other hand, the diffraction image from the identical region (1) in Figure 4.6 b) presents no such ambiguity, displaying a diffraction pattern without reflections and only the centre beam, characteristic for amorphous regions. The diffraction information in the corrected dataset thus displays unambiguous information compared to the non-corrected dataset. This demonstrates that S-SPED correction mitigates the effect of probe wandering, and leads to improved resolution in real and reciprocal space. This improvement in reciprocal space resolution is analogous to that illustrated in Figure 4.3.

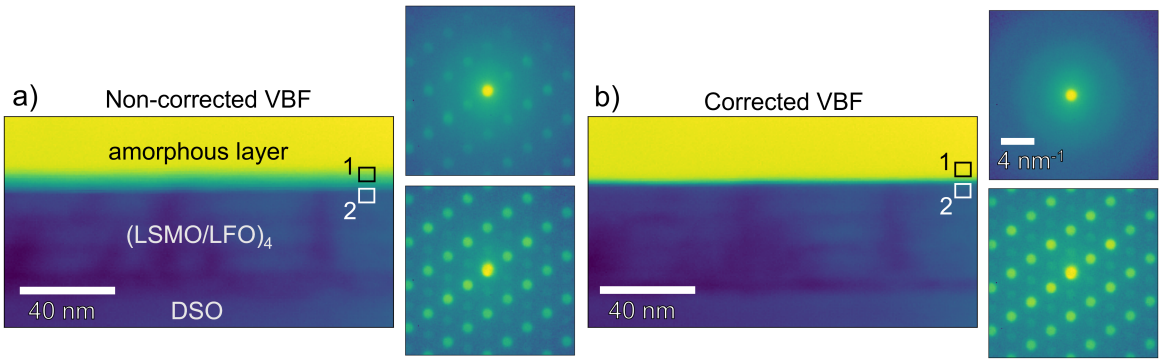

Figure 4.6: VBF images of $(LSMO/LFO)_4$/DSO with diffraction patterns generated from regions of interest above (1) and inside (2) the crystalline film. a) Non-corrected VBF image and diffraction patterns. b) Corrected VBF image and diffraction patterns.

All datasets presented above were achieved with "as good as possible" instrument alignment. Figure 4.7 shows the result of S-SPED correction of two "perfectly" aligned S-SPED datasets, with $n = 16$ and $n = 8$. These datasets exhibited significantly less probe wandering compared to the datasets aligned with "as good as possible" alignment. Although small shifts, 1.2 nm for $n = 8$ and 2.1 nm for $n = 16$ in Y, were observed and corrected between the segment slices, this did not result in detectable resolution improvement between the corrected and non-corrected VBF images in Figure 4.7. This suggests that "perfect" instrument alignment can bring the beam into the aberration free region of the ronchigram, minimizing probe wandering to a level where S-SPED correction is superfluous.

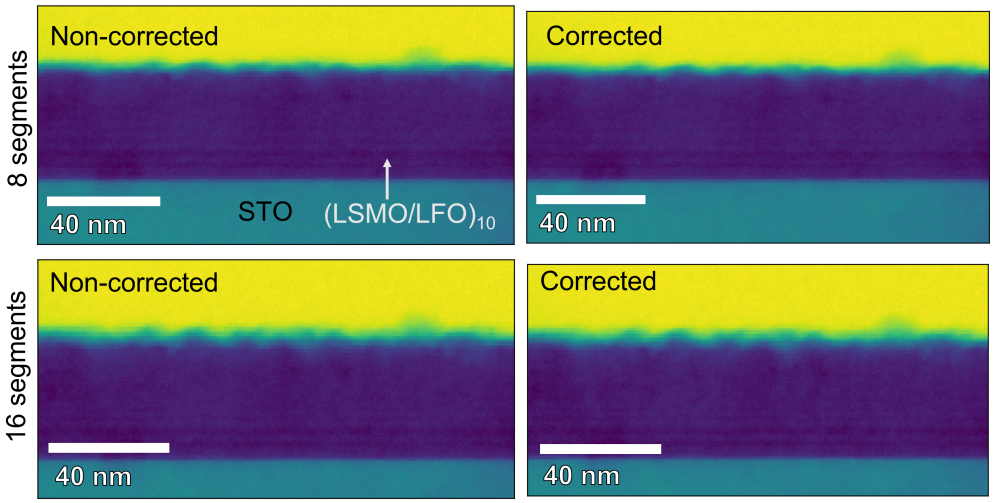

Figure 4.7: $n = 8$ and $n = 16$ segment "perfectly aligned" VBF images of $(LSMO/LFO)_{10}/STO$ before and after S-SPED correction.

Several types of instrument misalignment are known to introduce additional probe shifts during precession [14]. It is therefore useful to test the potential to counteract misalignment-induced probe shifts with S-SPED correction to improve resolution. Figure 4.8 illustrates the application of S-SPED correction on a dataset with an intentional pivot point misalignment applied to the Y scan coil. This misalignment was expected to cause additional probe shifts, especially in the Y direction. Indeed, the misaligned dataset required larger correctional shifts (up to 5.5 nm in Y) compared to a "as good as possibly" aligned dataset acquired during the same session (3.4 nm in Y).

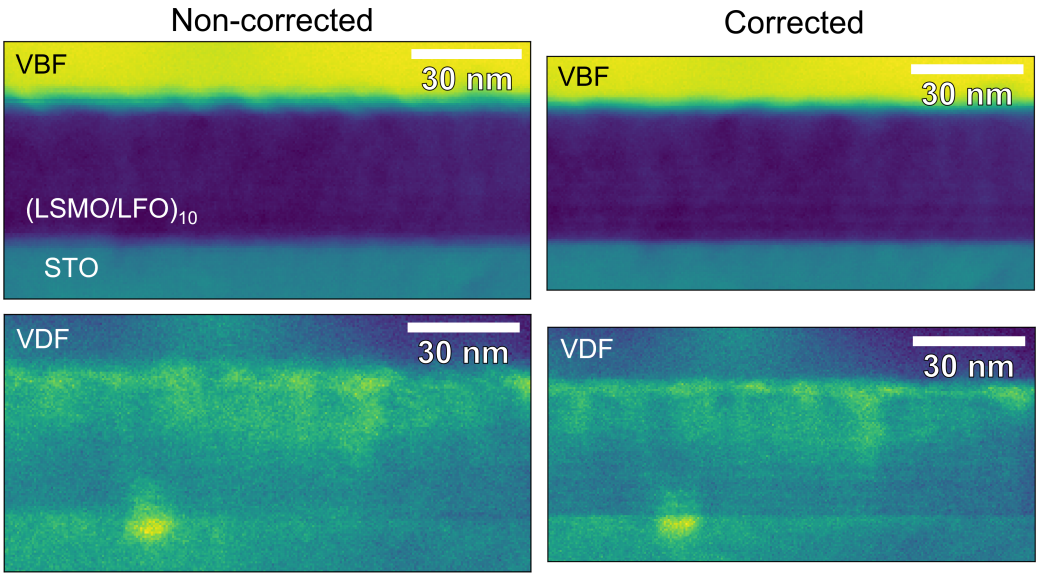

Figure 4.8: Non-corrected and corrected n=8 S-SPED VBF and VDF images of $(LSMO/LFO)_{10}/STO$ with deliberate pivot point misalignment.

VDF images were generated as previously described for $(LSMO/LFO)_{10}/STO$. The non-corrected virtual images display a distinct blur in the y-direction, obscuring the interfaces and individual superlattice layers. However, when S-SPED correction is applied, there is a noticeable improvement in resolution, resulting in the appearance of different contrast between LSMO and LFO. Figure 4.8 thus demonstrates that S-SPED can counteract the probe shifts induced by pivot point misalignment, and improve resolution. The other deliberately introduced misalignment involved adjusting the sample position to deviate from the focus point. The individual segment slice VBF images and the result of S-SPED correction is presented in Figure 4.9.

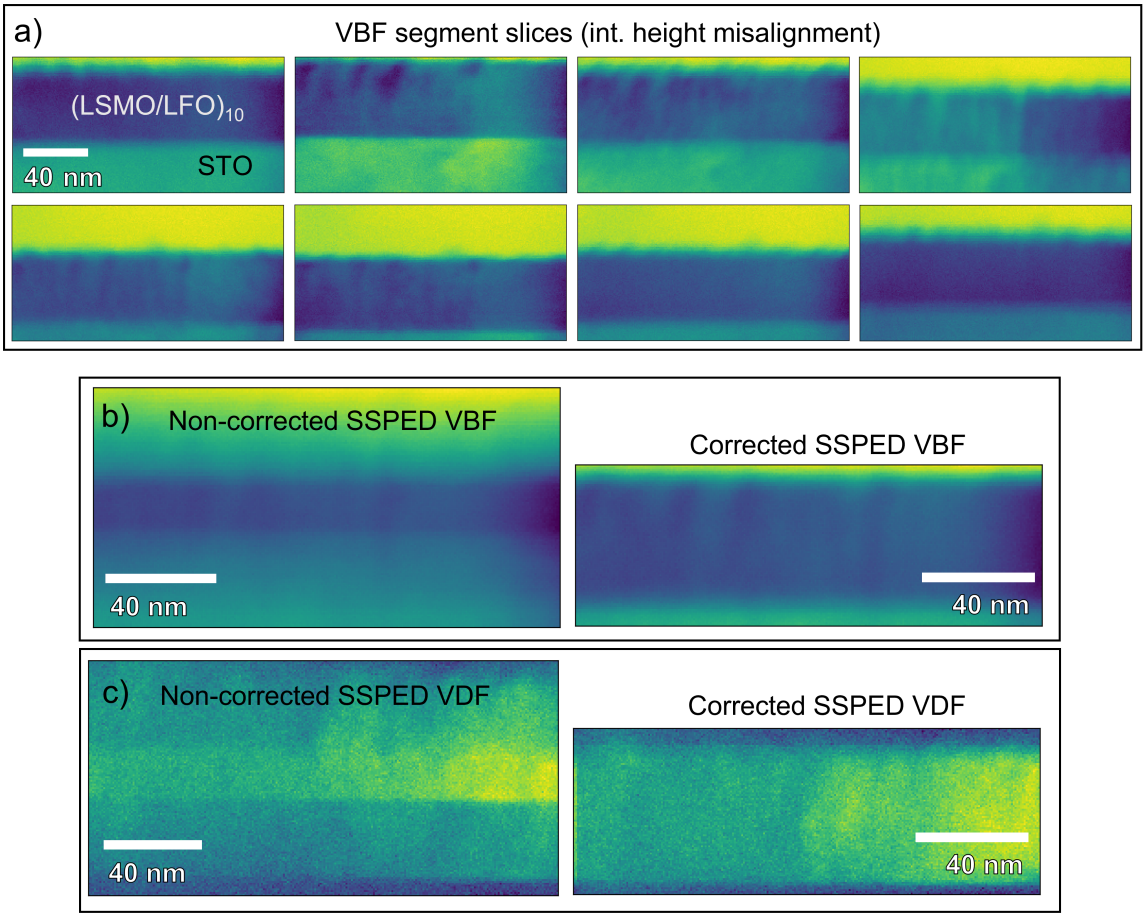

Figure 4.9: a) VBF images of each segment slice acquired with intentional sample position deviation from the focus point. The sample is $(LSMO/LFO)_{10}/STO$. Misalignment-induced probe shifts cause movement of the superlattice between segment slices. b) VBF image before and after S-SPED correction. c) VDF image before and after S-SPED correction.

Figure 4.9 a) shows that the deviation of the sample from the focus point dramatically increased probe motion. The maximum shift employed in correction of this data was 30 nm in Y, almost as large as thickness of the superlattice. The uncorrected S-SPED VBF and VDF in Figure 4.9 b) and c) are blurred to the point where the features are

unrecognizable. On the other hand, the corrected VBFs and VDFs in Figure 4.9 b) and c) exhibit well-defined contrast between the film and substrate. For the VDF, a reflection exclusive to LSMO and LFO (not found in STO) was selected. Consequently, only the superlattice appears bright in the corrected VDF image. This demonstrates that meaningful diffraction information can be extracted from the corrected dataset. Figure 4.9 thus shows how S-SPED correction can potentially salvage data recorded with very poor instrument alignment.
The resolution improvement achievable in Figure 4.9 b) and c) was primarily constrained by the blur resulting from the integration of probe wandering in each segment. This is seen as significant blur in the single segment VBF images in Figure 4.9 a). Determining the ideal number of segments in S-SPED acquisition involves a trade-off between dataset size and resolution improvement, which both theoretically increase with more segments. With more acquired segments, less probe wandering is integrated in each segment slice, resulting in higher resolution. To explore the impact of S-SPED correction with a varying number of segments, $n = 8$ and 16 segment S-SPED datasets were recorded, corrected and compared. A $n = 4$ segment dataset was constructed by summing two and two segments slices from the $n = 8$ segment dataset and performing regular S-SPED correction on this dataset. Figure 4.10 shows both single slices and full corrected datasets with $n = 4$, 8 and 16 segments.

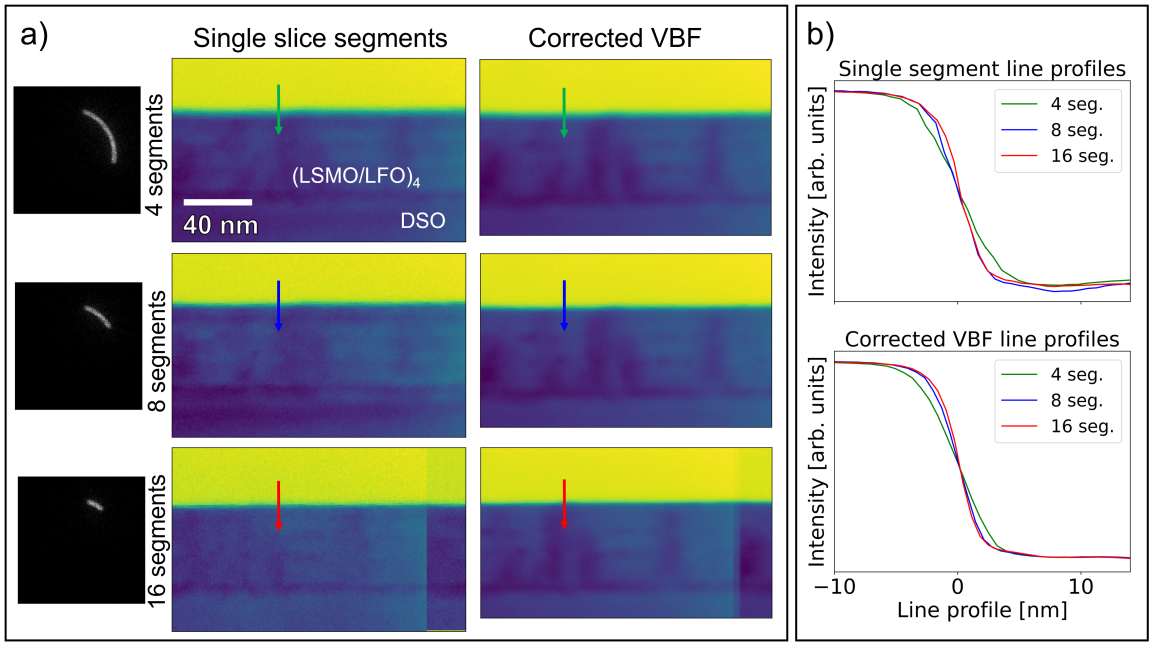

Figure 4.10: a) VBF images of $(LSMO/LFO)_4$/DSO acquired with $n = 4$, 8 and 16 segments. The leftmost images show the segment intensity integration path. The left VBF image column displays the first segment slice in each dataset, and the right VBF image column shows the result of S-SPED of all segments. b) Intensity line profiles, indicated by arrows.

The VBFs of single segment slices in Figure 4.10 a) demonstrate a distinct enhance-

ment in resolution when transitioning from 4 segments to 8 and 16 segments. This improvement is also seen in the corresponding intensity line profile in Figure 4.10 b), where the line profile exhibits a noticeably steeper slope for 8 and 16 segments compared to 4 segments. Similar trends can be observed in the VBF images and intensity line profiles of the complete corrected S-SPED datasets. Interestingly, the resolution improvement becomes less pronounced when progressing from 8 to 16 segments. Based on this, it can be determined that using $n = 8$ segments provides a favorable balance between data size and resolution improvement when imaging the superlattices studied in this work.

To conclude the Segmented SPED development chapter, improved real and reciprocal space resolution through application of the S-SPED technique has been demonstrated. Both inherent probe wandering due to precession and additional probe shifts induced by instrument misalignment have been minimized using S-SPED. However, S-SPED correction did not improve datasets recorded with "perfect" instrument alignment. Through the application of S-SPED, single superlattice layers were resolved in both samples. This would not have been possible with conventional SPED under "as good as possible" alignment. In this respect, the development of the S-SPED methodology proved crucial for the crystallographic characterization work conducted in this thesis.

Chapter 5

Superlattice characterization

5.1 EELS

5.1.1 Chemical composition

STEM-EELS has been used to probe the relative chemical composition along line scans traversing the superlattice layers. This was done by measuring the relative intensity of the ionization edges of the elements in the sample. Figure 5.1 shows the result of chemical composition EELS line scans across both superlattices, along with STEM-HAADF overview images. The Sr-$L_{2,3}$ edge signal was very low due to the high energy onset compared to other core loss edges in the same EEL spectrum, and was therefore omitted from the chemical composition line plots.
Several interesting features can be observed in the chemical composition line plots. As expected, the intensities of the Mn, Fe, and La signals vary periodically, corresponding to the alternating layers of LSMO and LFO in both superlattices. However, in Figure 5.1 c), around 25 nm into $(LSMO/LFO)_{10}$/STO, the alternating intensities seem to flatten out in the direction away from STO. This suggests that LSMO and LFO are mixed in the topmost layers. Moreover, the corresponding STEM-HAADF image in Figure 5.1 d) shows that certain regions in the upper layers of the superlattice are blurred, supporting the observation of chemical intermixing. The fact that the mixing of LFO and LSMO is only observed in the topmost layers of the superlattice suggests that this is a result of 3D growth rather than uniform diffusion.

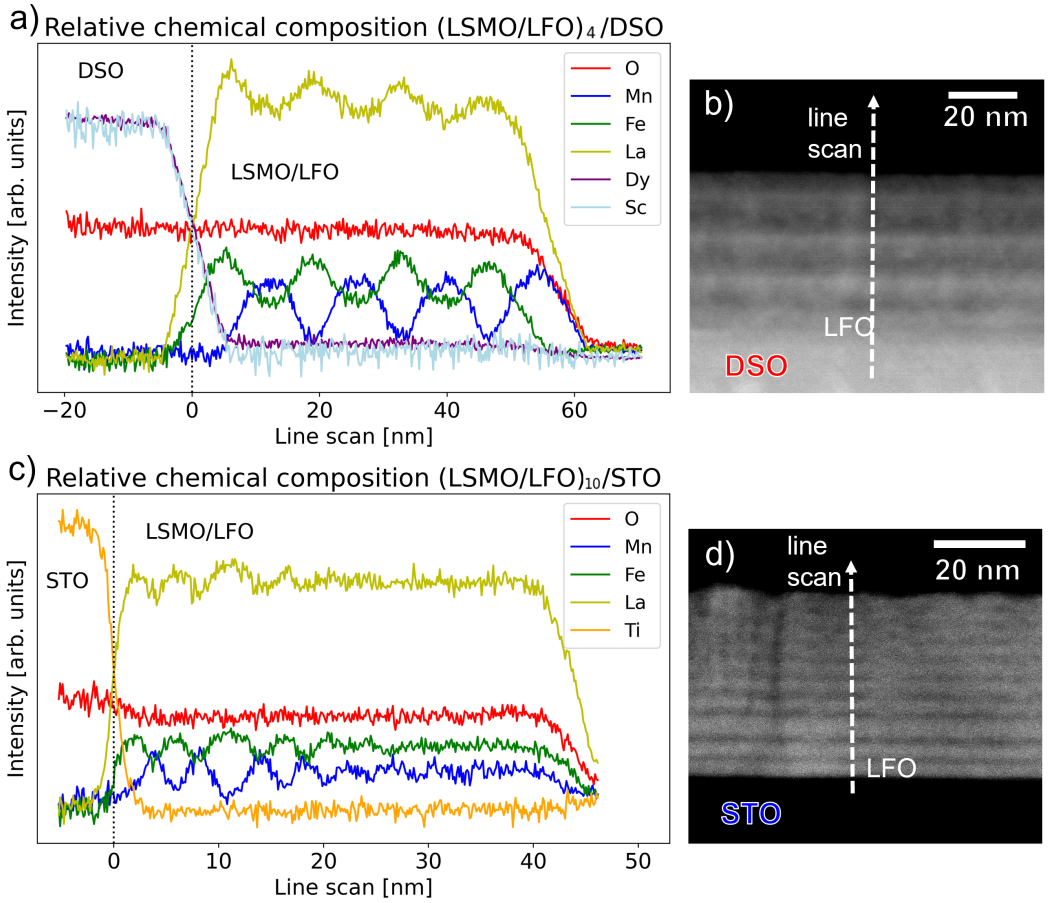

Figure 5.1: Relative chemical composition based on EELS intensity. a) Relative chemical composition in $(LSMO/LFO)_{10}/STO$. b) Relative chemical composition in $(LSMO/LFO)_4/DSO$. c)-d) STEM-HAADF overview images marking the path of the EELS line scans.

The chemical composition EELS scans also show evidence of interdiffusion of Fe into LSMO in both superlattices. In both $(LSMO/LFO)_4/DSO$ and $(LSMO/LFO)_{10}/STO$, the Mn edge intensity declines to approximately zero within the LFO layers. Within LSMO, the Fe edge intensity remains relatively high, suggesting the presence of Fe in these layers. The only layer in which the Fe signal declines to 0, is the topmost layer of LSMO in $(LSMO/LFO)_4/DSO$. Noticeably, this is the only LSMO layer not covered by LFO. This suggests that LFO has diffused into adjacent LSMO layers.
Individual EEL spectra from LSMO and LFO in both superlattices have been compared in order to detect the presence of Fe-$L_{2,3}$ peaks in LSMO. This is shown in Figure 5.2. In agreement with the chemical line scan results, the spectra in Figure 5.2 c) and d) show a prominent Fe-$L_{2,3}$ peak in LSMO within both $(LSMO/LFO)_{10}/STO$ and $(LSMO/LFO)_4/DSO$. This confirms the hypothesis that Fe has diffused into LSMO in both superlattices. On the other hand, only very weak Mn-$L_{2,3}$ peaks are found in LFO in Figure 5.2 a) and b). This could suggest that minor diffusion of Mn into LFO may have occurred too.

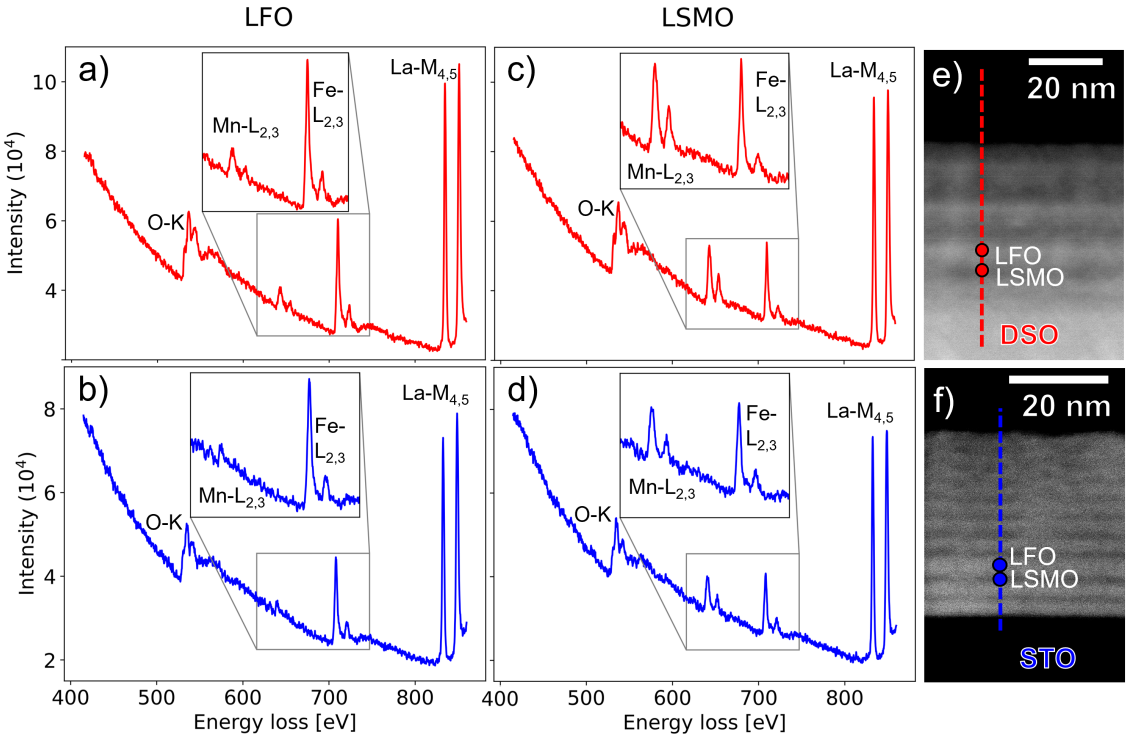

Figure 5.2: EEL spectra from the scan points indicated with red ($(LSMO/LFO)_4/DSO$) and blue ($(LSMO/LFO)_{10}/STO$) circles. Insets show magnified regions of the spectra where the Mn-$L_{2,3}$ and Fe-$L_{2,3}$ edges are located. EEL spectrum from a) LFO in $(LSMO/LFO)_4/DSO$. b) LFO in $(LSMO/LFO)_4/DSO$, c) LSMO in $(LSMO/LFO)_4/DSO$, d) LSMO in $(LSMO/LFO)_{10}/STO$, e)-f) STEM-HAADF overview images with the line scans and spectrum acquisition points indicated.

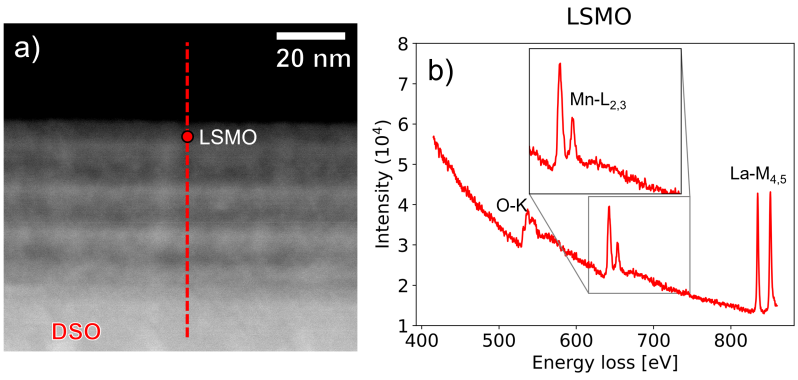

Figure 5.3: a) STEM-HAADF line scan overview image with the spectrum acquisition point indicated by a circle. b) EEL spectrum from the topmost layer of LSMO in $(LSMO/LFO)_4/DSO$.

The EEL spectrum from the topmost LSMO layer of $(LSMO/LFO)_4/DSO$ is shown

in Figure 5.3. The absence of a Fe-$L_{2,3}$ peak confirms that this layer is devoid of Fe, as seen in the chemical composition line scan. An interesting question is whether the oxidation state is different between "native" Fe in LFO and interdiffused Fe in LSMO. This was examined by comparing the white-line-ratio of Fe-$L_{2,3}$ from LFO and LSMO in both superlattices. No difference in white-line ratio was detected, suggesting that no measurable change in oxidation state had occurred during diffusion. This result is included in Appendix B.

5.1.2 Fine structure EELS

In this section, the white-line ratios of Mn-$L_{2,3}$ and Fe-$L_{2,3}$ are computed in all LSMO and LFO layers in order to detect relative changes in the Mn and Fe oxidation state. Additionally, the ELNES of the O-K edge in each layer is examined for indications of oxygen vacancies. Figure 5.4 shows these spectral features measured from the centre position of each superlattice layer in each sample. Plots of the relative chemical composition of Fe and Mn are included for an overview of the LSMO and LFO layers in the superlattices, along with numbers annotating the layers. Spectral features measured in LFO (Fe-$L_{2,3}$ and O-K) are marked with green, and spectral features measured in LSMO (Mn-$L_{2,3}$ and O-K) are marked with blue. The numbers along the y-axis of the fine structure plots correspond to the annotated layers in the chemical composition plots.

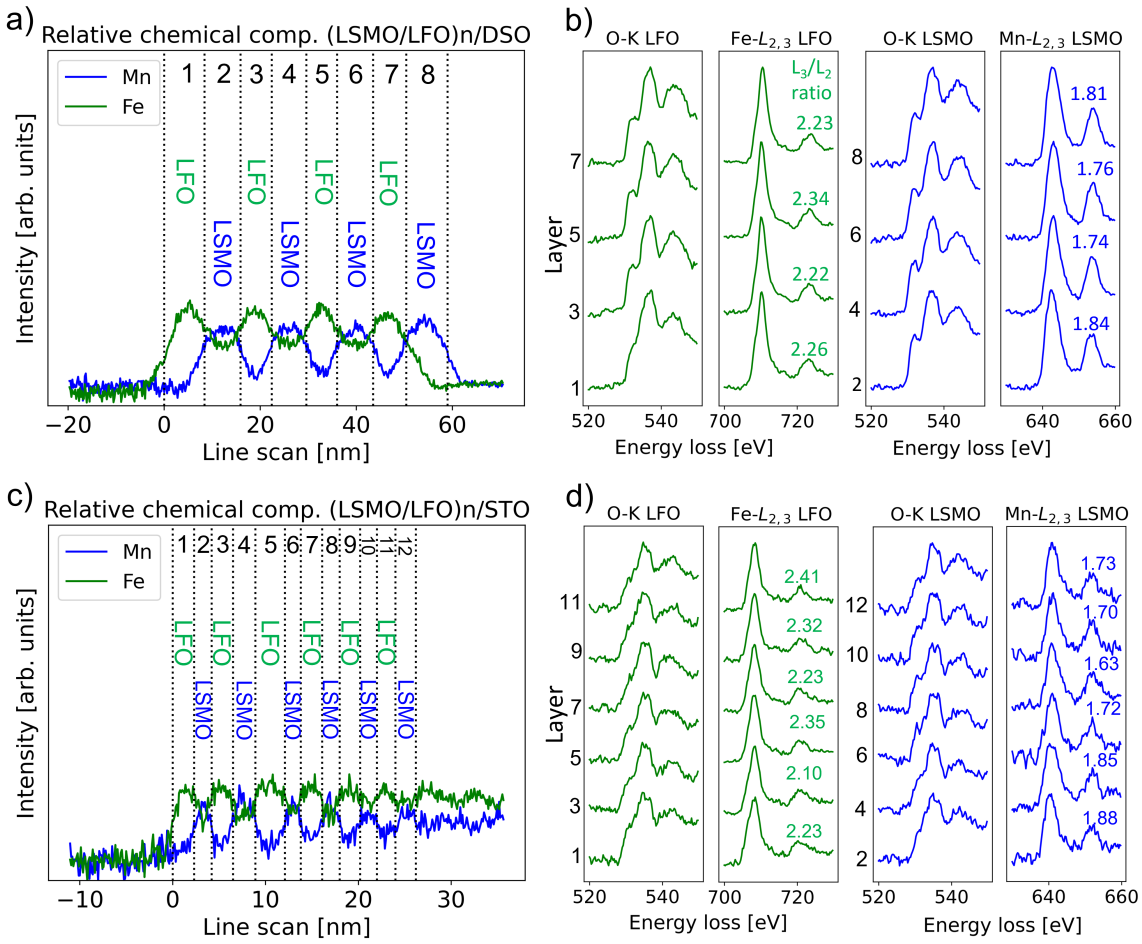

Figure 5.4: a) Relative chemical composition of Fe and Mn in $(LSMO/LFO)_4/DSO$. b) EELS fine structure plots from all layers; O-K ELNES, Fe-$L_{2,3}$ from LFO and Mn-$L_{2,3}$ from LSMO in $(LSMO/LFO)_4/DSO$. c) Relative chemical composition of Fe and Mn in $(LSMO/LFO)_{10}/STO$. d) O-K ELNES, Fe-$L_{2,3}$ from LFO and Mn-$L_{2,3}$ from LSMO in $(LSMO/LFO)_{10}/STO$.

An initial observation from Figure 5.4 b) is a reduction in intensity of the O-K P-peak and B-peak in the initial LFO layer (layer 1) of $(LSMO/LFO)_4/DSO$. This is typically indicative of oxygen vacancies [43]. The O-K edge ELNES of the successive LFO and LSMO layers display normal P- and B-peak intensities, suggesting that oxygen vacancies only occur in the bottom layer of LFO.
As seen in Figure 5.4 d) the EELS signal from $(LSMO/LFO)_{10}/STO$ is noisier than the signal from $(LSMO/LFO)_4/DSO$. As some spectral features may be obscured by signal noise, the following observations are made with a degree of uncertainty. It appears that the P-peak of the O-K edge ELNES is absent in multiple layers of both LSMO and LFO in $(LSMO/LFO)_{10}/STO$ (layer 1-4 and 9-12), and only present in the central layers (layer 5-8) of the superlattice. This is indicative of oxygen vacancies near both the top and bottom regions of $(LSMO/LFO)_{10}/STO$. Changes in the B-peak intensity are difficult to assess due to noise in the signal.
The observations of a weakening of the P- and B-peak in the O-K edge ELNES are expected to be accompanied by a reduction of the white-line ratio due to a reduction of the TM-oxidation state [43]. However, no corresponding changes in the white-line ratios of Fe-$L_{2,3}$ or Mn-$L_{2,3}$ are observable in Figure 5.4. Moreover, the edge onset energy of the TM-$L_{2,3}$ does not change in layers with and without oxygen vacancies. This suggests that the formation of oxygen vacancies is not related to a reduction in the TM oxidation state in neither of the superlattices.
Figure 5.5 shows an apparent chemical shift of the Mn-$L_{2,3}$ edge onset energy within single layers of LSMO in $(LSMO/LFO)_4/DSO$.

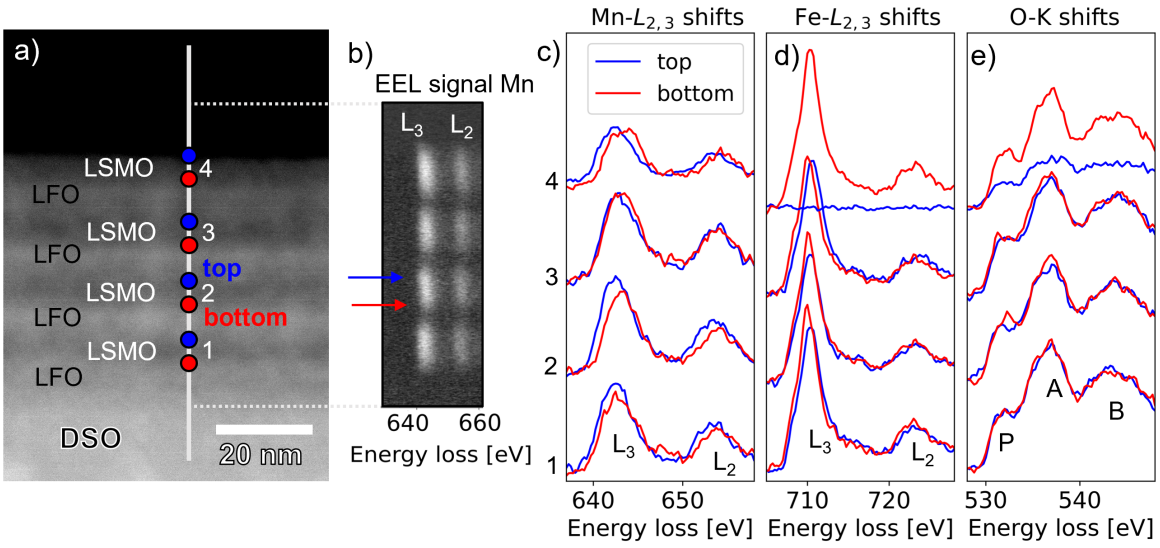

Figure 5.5: a) STEM-HAADF overview image of $(LSMO/LFO)_4/DSO$ with top (blue) and bottom (red) measurement points indicated along the line scan. b) Intensities of Mn-$L_{2,3}$ as a function of position along line scan and energy loss (x-axis). This plot is aligned with the STEM-HAADF image. c)-e) Mn-$L_{2,3}$, Fe-$L_{2,3}$, O-K edge ELNES from the top and bottom region of each LSMO layers.

The onset energy is highest in the lower region of each layer and gradually shifts to lower onset energies towards the upper part of each LSMO layer. This is seen as a leftward tilt of the Mn signal plotted along the line scan in Figure 5.5 b), indicated by arrows. Individual spectra from the top (blue) and bottom (red) regions of each LSMO layer are shown in Figure 5.5. There is a clear chemical shift of ≈ 1 eV in the first, second, and fourth LSMO layer.

The chemical shift could indicate a change in the oxidation state of Mn. However, the white-line ratio of Mn-$L_{2,3}$ between the top (blue) and bottom (red) measurements appears unchanged in all measurements except in the topmost layer, contradicting this. Since LSMO is a mixed valence system, the Mn-$L_{2,3}$ spectral features consist of a combination of the peaks normally attributed to Mn^{3+} and Mn^{4+}, making the interpretation of the chemical shift more complicated. One possible explanation for observed features is that a gradual change of the relative concentration of Mn^{3+} and Mn^{4+} through the LSMO layers has occurred. This would imply that the bottom regions of the LSMO layers contain more Mn^{4+} compared to Mn^{3+}, and the topmost layers contain a relatively higher concentration of Mn^{3+}. Such a change in the net oxidation state of Mn could be related to the interdiffusion of Fe in LSMO, but this is difficult to determine.

As no systematic chemical shifts or changes in the ELNES are observed at the O-K edge, the proposed change in the net Mn oxidation state is most likely not related to oxygen vacancies. A small chemical shift in the opposite direction as that of Mn-$L_{2,3}$ is noticed in the Fe-$L_{2,3}$ edge in layer 1,2 and 3. However, as this is a significantly smaller shift than that observed in Mn, it is difficult to determine whether this is systematic or coincidental.

The topmost measurement from the upper superlattice layer shows signs of oxygen vacancies and a reduced oxidation state in Mn. The reduced oxidation state is observed as a reduction of the Mn-L_3 peak compared to the Mn-L_2 peak (a reduced white-line ratio). Oxygen vacancies are indicated by the reduced P- and B-peak intensity and overall intensity reduction of the O-K edge. As this measurement point is very close to the end of the superlattice, which is subject to chemical interaction with the surrounding environment, oxygen vacancies and a reduced Mn oxidation state is not surprising, and most likely not related to the chemical shift observed in the other layers.

Overall, the observed chemical shift in the Mn-$L_{2,3}$ onset energy could be explained by a change in the net oxidation state of Mn. However, multiple factors can influence the edge onset energy of Mn, and more research is needed to understand the nature of the observed chemical shift.

5.2 Crystallographic characterization

5.2.1 Domain 1 and domain 2 definitions

Two structural domains have been identified in both superlattices, based on the S-SPED, HRTEM and FFT results presented in Section 5.2.3. This means that two different lattice orientations with distinct FFT and S-SPED patterns have been discovered in the samples. These structural domains will be referred to as domain 1 and domain 2. However, there are multiple possible crystallographic orientations in the samples which produce degenerate or practically indistinguishable diffraction patterns. It is therefore necessary to define the classification of domains utilized in the interpretation of the crystallographic characterization. In the following section, the degenerate and quasi-degenerate crystal orientations encompassed by the terms domain 1 and 2 will be presented, along with their corresponding simulated diffraction patterns. Figure 5.6 shows which orientations of LFO are defined as domain 1 and 2.

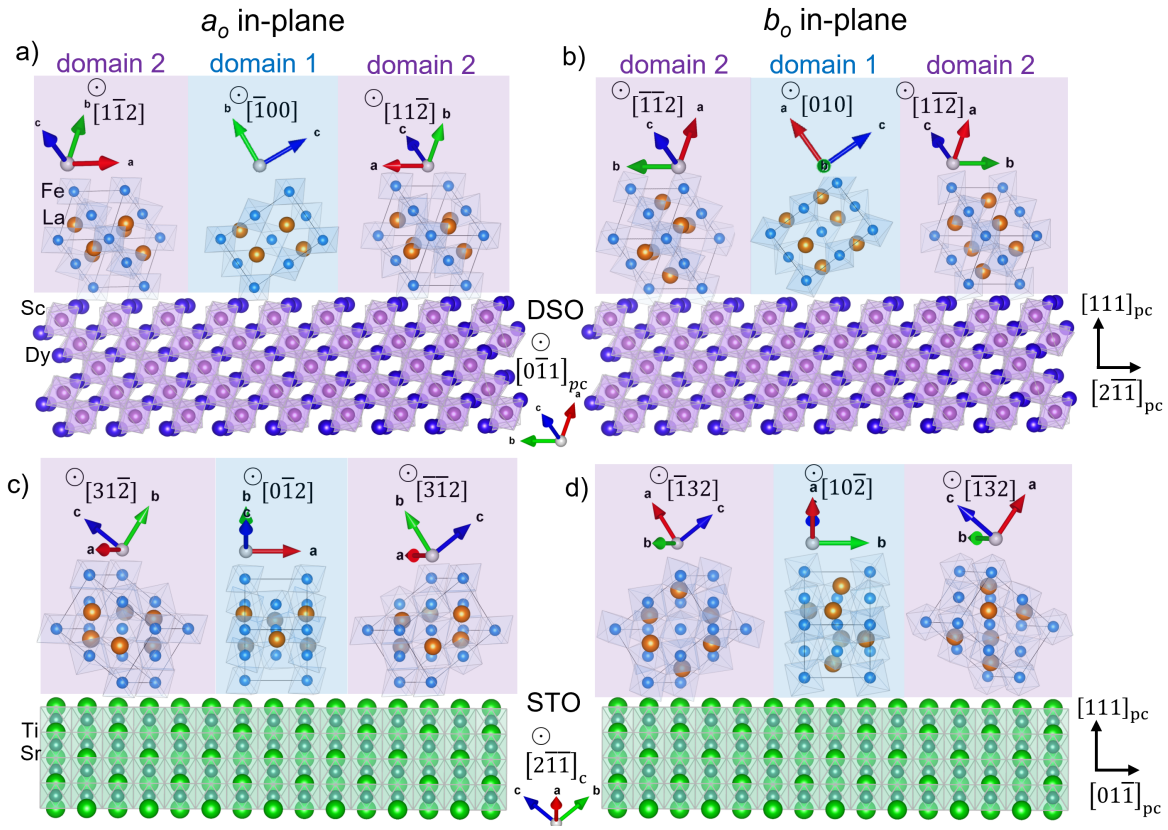

Figure 5.6: Schematic overview of the LFO orientations on STO$(111)_{pc}$ and DSO$(101)_o$ defined as domain 1 (blue) and domain 2 (purple). a) $(011)_o$ and b) $(101)_o$ LFO unit cell rotations on DSO$(101)_o$ seen along the $[0\bar{1}1]_{pc}$ zone axis. c) $(011)_o$ and c) $(101)_o$ LFO unit cell rotations on STO$(111)_{pc}$ seen along the $[2\bar{1}\bar{1}]_{pc}$ zone axis.

Note that the orientations of LFO are given in the orthorombic system, while the orientations of the substrates are given in pseudocubic coordinates in Figure 5.6. The samples are imaged along the $[0\bar{1}1]_{pc}$ zone axis for DSO and $[2\bar{1}\bar{1}]_{pc}$ for STO. Along both of these zone axes, the orthorombic unit cell has two degenerate and one non-degenerate rotation on the $(111)_{pc}$ surface in terms of diffraction. The term "domain 1" represents the non-degenerate orientation of the orthorombic unit cell, while "domain 2" represents the two degenerate orientations seen along the $[0\bar{1}1]_{pc}$ and $[2\bar{1}\bar{1}]_{pc}$ zone axes. It is not known which one of the orthorombic $(101)_o$ or $(011)_o$ facets of LFO that are parallel to the $(111)_{pc}$ substrates. Figure 5.6 shows all possible orientations of LFO on the two substrates seen along their respective zone axes which result in domain 1 (blue background) and domain 2 (purple background) characteristics. $(011)_o$ oriented LFO has the orthorombic $a_o \parallel (111)_{pc}$ (denoted as a_o in-plane), while $(101)_o$ oriented LFO has $b_o \parallel (111)_{pc}$ (denoted as a_o in-plane) in the Figure 5.6. The visualization is created with bulk unit cells using Vesta [25]. The illustration does therefore not accurately represent the unit cells or relative ionic radii in the superlattices.

In order to distinguish the domains in diffraction experiments, domain 1 is defined by having a periodicity doubling in the $[01\bar{1}]_{pc}$ direction relative to a pseudocubic unit cell, and domain 2 by not having this. This distinction has been used to classify domains of LFO on STO$(111)_c$ previously [18]. Along the zone axis of the (LSMO/LFO)$_{10}$/STO sample, this mean that domain 1 has one of the orthorombic short axes (a_o or b_o) aligned with the $[01\bar{1}]_{pc}$ direction, perpendicular to the electron beam. Along the zone axis of (LSMO/LFO)$_4$/DSO, this means that domain 1 has one of the orthorombic short axes (a_o or b_o) aligned parallel with the electron beam. All LFO orientations meeting these conditions are marked with the blue "domain 1" background in Figure 5.6. The terms orientation, growth and structure will be used to describe the two domains in the following sections. In this context, all of these terms will refer to the rotations of LFO and LSMO on the $(111)_{pc}$ shown in Figure 5.6 and Figure 5.8.

5.2.2 Diffraction simulations

The diffraction patterns simulated with ReciPro [47] used to identify domain 1 and 2 orientations of LFO in the superlattices are presented in Figure 5.7.

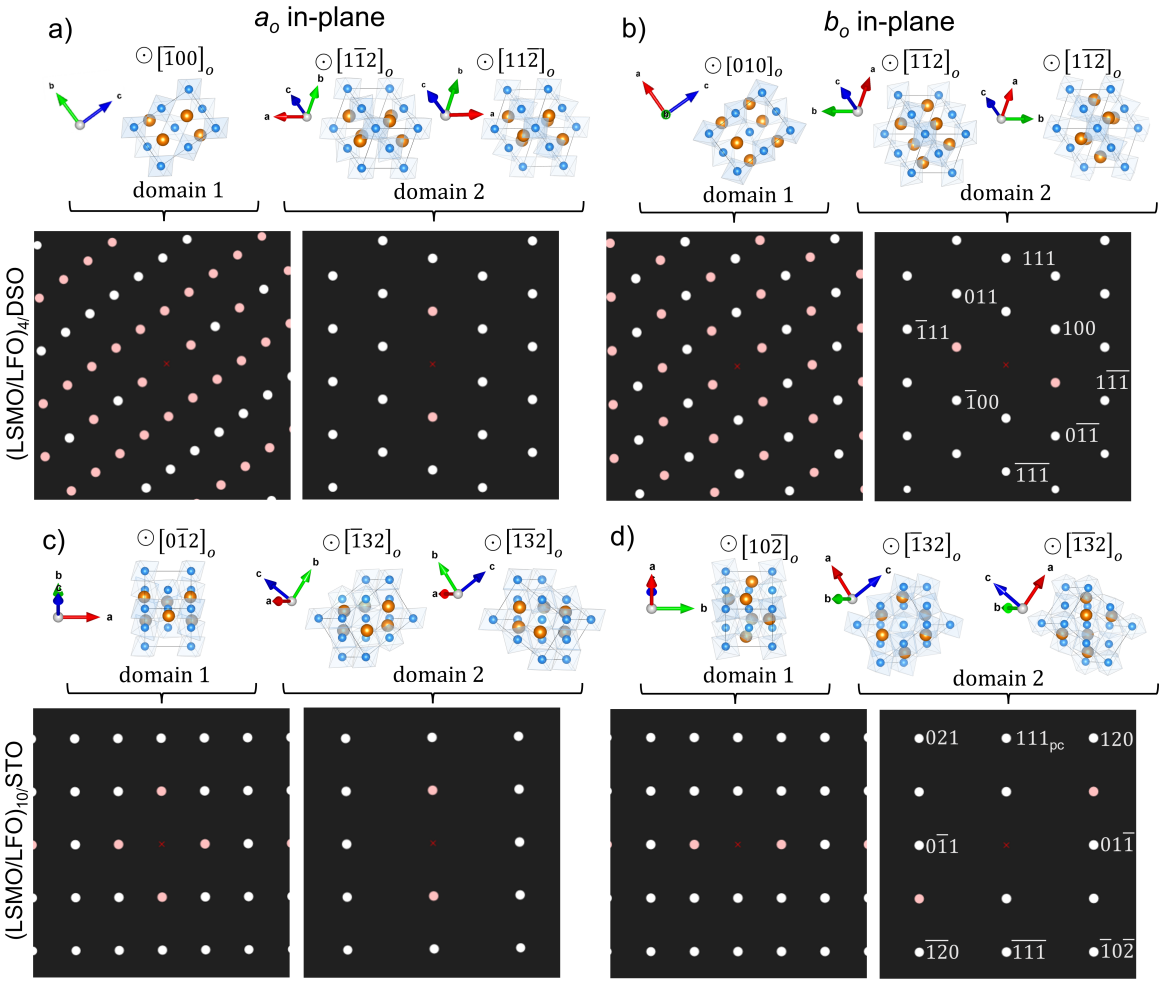

Figure 5.7: Domains used to identify domain 1 and 2 in the samples. Extinct reflections are marked with red. a) Simulated diffraction patterns of $(011)_o$ and b) $(101)_o$ LFO unit cell rotations on DSO$(101)_o$ seen along the $[0\bar{1}1]_{pc}$ zone axis. c) Simulated diffraction patterns of $(011)_o$ and c) $(101)_o$ LFO unit cell rotations on STO$(111)_{pc}$ seen along the $[2\bar{1}\bar{1}]_{pc}$ zone axis.

The simulated diffraction patterns in Figure 5.7 are used to differentiate between domain 1 and 2 orientations in LFO through comparison with FFT and S-SPED patterns. It is clear from Figure 5.7 that the diffraction patterns from LFO$(101)_o$ and LFO$(011)_o$ are practically indistinguishable if extinction is not considered. Both of these orientation possibilities are therefore included when referring to the simulated diffraction patterns of the two domains. Generally, not considering extinction, the domains can be distinguished by having different frequencies in different direction. Along the $[0\bar{1}1]_{pc}$ zone axis, in the (LSMO/LFO)$_4$/DSO sample, the diffraction pattern

of domain 1 is characterized by having an extra frequency, a periodicity doubling, in the $[100]_{pc}$ direction compared to domain 2. Along the $[2\bar{1}\bar{1}]_{pc}$ zone axis, in the $(LSMO/LFO)_{10}/STO$ sample, the diffraction pattern of domain 1 is characterized by having an extra frequency in the $[01\bar{1}]_{pc}$ direction compared to domain 2.
The orientations of LSMO seen along the pseudocubic zone axes of the two samples and their corresponding simulated diffraction patterns are shown in Figure 5.8.

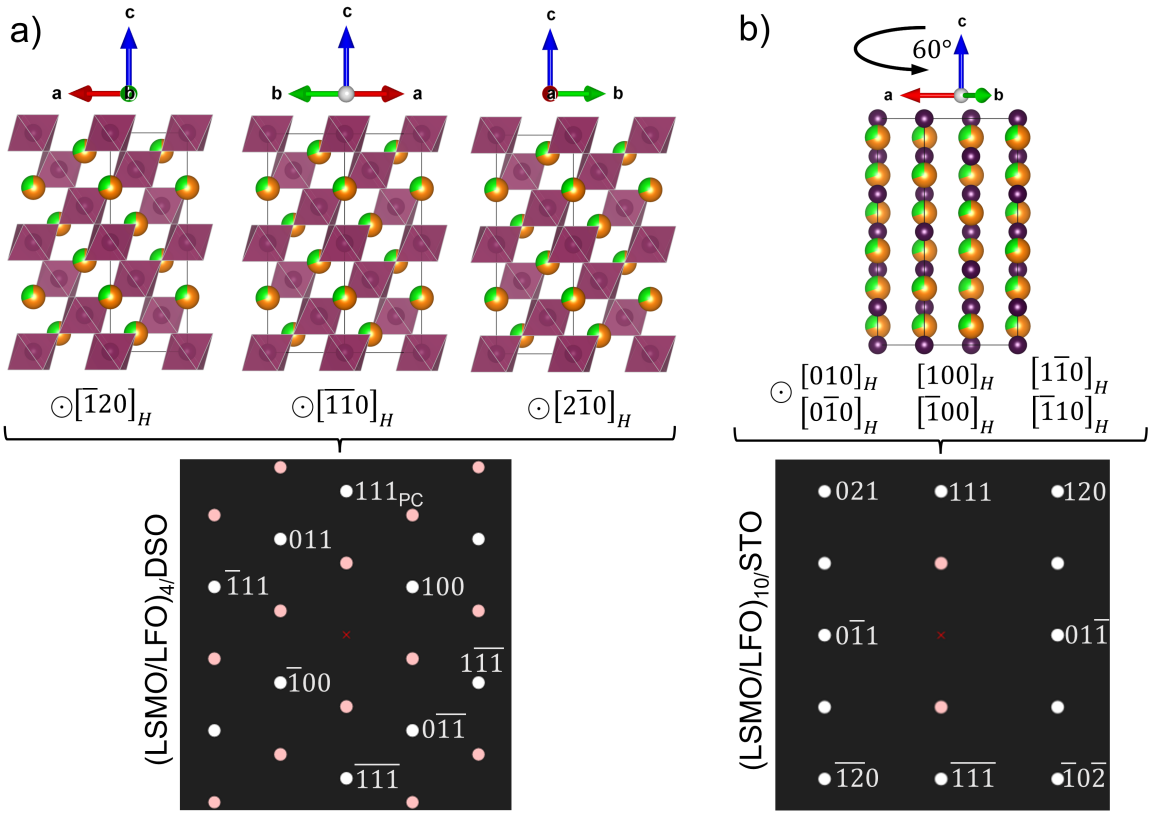

Figure 5.8: Orientations and their corresponding simulated diffraction pattern of LSMO on $(111)_{pc}$ substrates. a) Three degenerate LSMO orientations and diffraction patterns seen along the $[2\bar{1}\bar{1}]_{pc}$ zone axis. b) Six degenerate LSMO orientations and diffraction patterns seen along the $[0\bar{1}1]_{pc}$ zone axis.

Note that the orientations of LSMO are given in the hexagonal system in Figure 5.8. Due to the hexagonal surface symmetry of bulk LSMO, there exists three orientations that yield indistinguishable diffraction patterns along the $[2\bar{1}\bar{1}]_{pc}$ zone axis, as seen in Figure 5.8 a). Similarly, six orientations produce identical simulated diffraction patterns along the $[0\bar{1}1]_{pc}$ zone axis seen in Figure 5.8 b). Hence, when discussing domain growth within these superlattices, the domain 1 and 2 classification only applies to the LFO layers. Ignoring extinction differences, it can be noted that the simulated diffraction patterns of LSMO have identical symmetries as the simulated diffraction patterns of LFO domain 2 in Figure 5.7.

5.2.3 Experimental findings

The following section includes HRTEM images of the superlattices, displaying phase contrast. As detailed in Section 2.2.1, phase contrast interpretation is not straightforward. Hence, the conclusions drawn about atomic lattice structures from HRTEM images are always considered along with S-SPED data. All (hkl) indices and zone axes will be given in pseudocubic coordinates throughout this section. It is assumed that the S-SPED patterns result from a combination of dynamic and kinematic scattering in the samples. This impacts the interpretation of features in the obtained S-SPED patterns, especially when considering extinction. In the following section, some diffraction features can only originate from structural changes in the materials, while other features can be explained by either structural changes or dynamic scattering effects. Although the ReciPro simulations are kinematic, the contribution of dynamic effects in S-SPED patterns will be considered in the following analysis.

$(LSMO/LFO)_{10}/STO$

The S-SPED patterns from individual LFO and LSMO layers from $(LSMO/LFO)_{10}$ /STO are shown in Figure 5.9. These two diffraction patterns appear practically indistinguishable. This could be caused by mixing of the layers by 3D growth, causing both LSMO and LFO to contribute in the showcased diffraction patterns. However, there is reason to assume that this is not the case, and that the two diffraction patterns represent structural information from the separate layers. This implies that the similarity in diffraction patterns are caused by a similarity of the crystal structure of LSMO and LFO, rather than mixing of these layers. The reasoning behind this assumption and supporting evidence is addressed in Section 6.3.

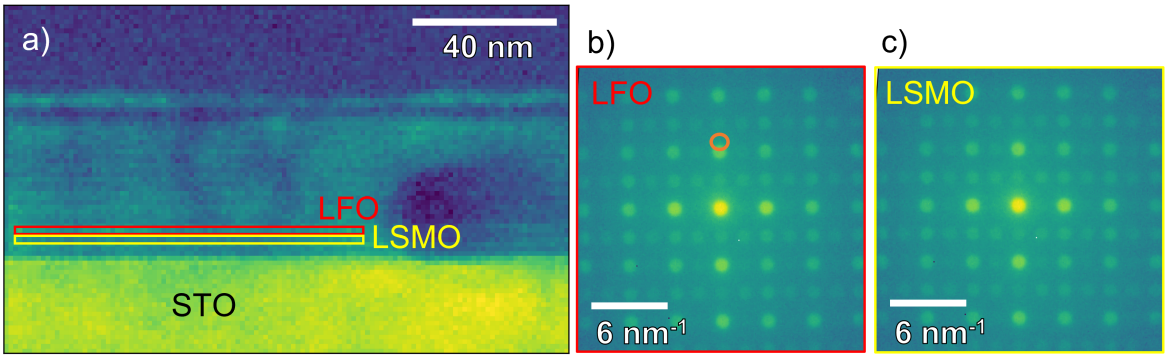

Figure 5.9: a) VDF image generated by selecting the edge of the $(111)_{pc}$ diffraction spot with a virtual aperture. b) Diffraction pattern from the ROI indicated by a red square, in LFO. Placement of the virtual aperture is indicated with an orange circle. c) Diffraction pattern from the ROI indicated by a yellow square, in LSMO.

When comparing the diffraction patterns in Figure 5.9 with simulated diffraction patterns of LFO and LSMO in Figure 5.7 c) and d) and Figure 5.8 b), both of the

diffraction patterns resemble the simulated diffraction pattern of LFO in the domain 1 orientation. This indicates that LSMO has undergone a change in crystal structure, as the S-SPED pattern from LSMO has new reflections which are not present in simulations of the bulk structure in Figure 5.8. These diffraction features cannot be explained by dynamic scattering effects. It can thus be assumed that LSMO has undergone structural changes and obtained a structure similar to LSMO in this superlattice.

The difference between the diffraction patterns in Figure 5.9 b) and c) compared to the simulated diffraction pattern of LFO domain 1 is that kinematically extinct reflections are present in the S-SPED patterns. This could be explained by both dynamic scattering effects and structural changes from the bulk LFO structure. It is possible that subtle structural changes in the crystal structure has altered the symmetry changing the conditions extinction. Previous studies by Kjærnes et al. [21] discovered distortion of LFO on STO(111) leading to a monoclinic unit cell. As distortion of the LFO unit cell has been observed in previous studies, this is not unlikely. However, it is not possible to determine whether the appearance of extinct reflections in S-SPED are caused by structural changes, dynamic scattering or a both. The proposed similarity in crystal structure in LSMO and LFO in this superlattice will be referred to as structural coupling between the layers. It should be noted that the diffraction patterns in Figure 5.9 could consist of a combination of LFO domain 1 and domain 2 diffraction patterns, as all reflections in domain 2 also appear in in domain 1 diffraction patterns, ignoring differences in extinction.
It is possible that the alterations of the LSMO crystal structure could be induced by interdiffusion of Fe in LSMO. Considering the thickness of 5 and 8 $(111)_{pc}$ monolayers in LSMO and LFO layers, respectively, structural distortion is not surprising, as this is more plausible to occur in epitaxial layers with monolayer thickness.

Further signs of structural coupling between the LSMO and LFO layers in $(\text{LSMO/LFO})_{10}$/STO are observed in the S-SPED images in Figure 5.10. This shows VDF images of two different regions of the superlattice along with diffraction images from different domains and the STO substrate. The VDFs were generated in order to identify domain 1 and 2 orientations in the superlattice. This was done by selecting the reflection between $(111)_{pc}$ and $(120)_{pc}$ with a virtual aperture, as this reflection is exclusively found in LFO domain 1, and not in LSMO or LFO domain 1. Consequently, only regions with LFO domain 2 crystal structure appears bright in the VDF images in Figure 5.10. Single layer resolution has been demonstrated in this the S-SPED dataset in Figure 5.10 b) in Section 4.3. This implies that the LSMO layers would have showed dark contrast in the VDF in Figure 5.10 b) if it still maintained its bulk unit cell. However, the VDF contrast intead suggests that LSMO and LFO both scatter equally to the selected reflection. This supports the hypothesis that a change of unit cell structure has occurred in LSMO.

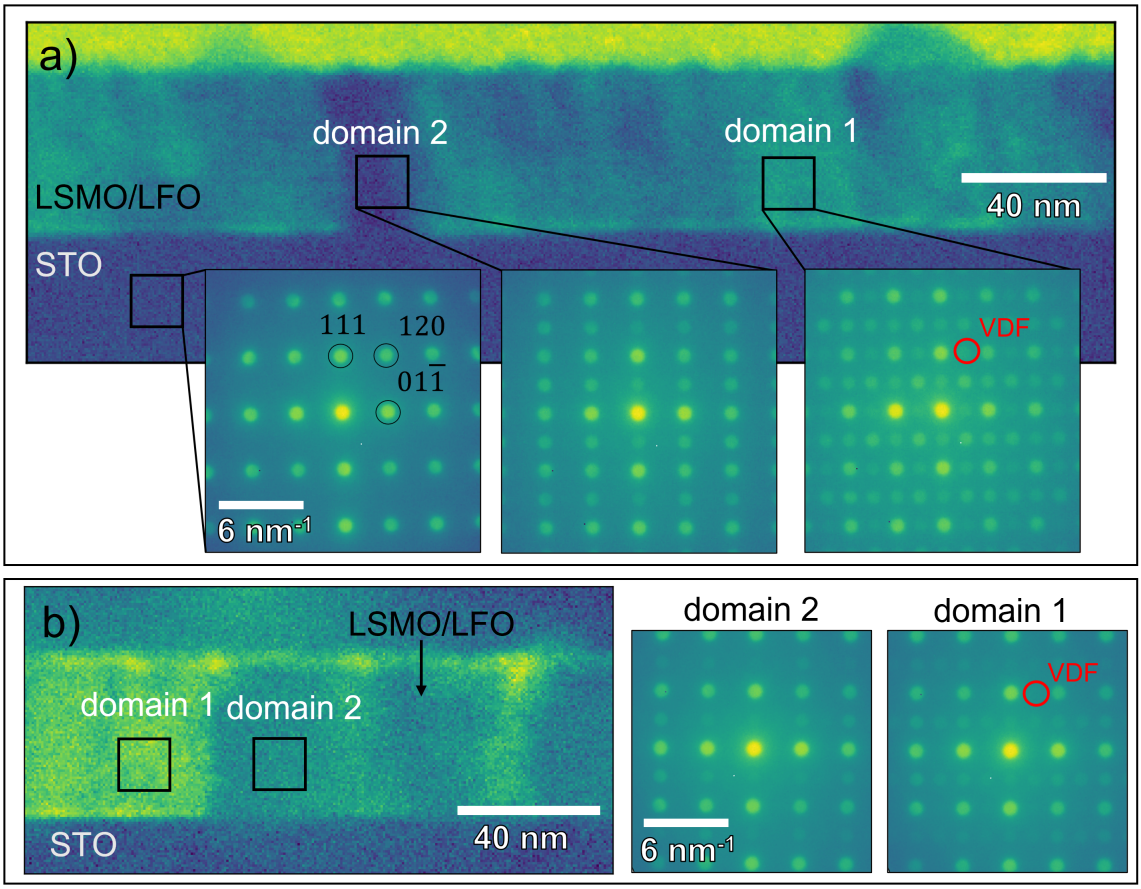

Figure 5.10: a) SPED and b) S-SPED of two $(LSMO/LFO)_{10}/STO$ regions. The following description applies to a) and b): VDFs acquired along the $[2\bar{1}\bar{1}]_{pc}$ zone axis with diffraction images indicated by black squares. Red circles mark the diffraction spots selected to generate the VDFs.

While the VDF contrast in Figure 5.10 a) indicates that the majority of the $(LSMO/LFO)_{10}/STO$ superlattice has domain 1 orientation, Figure 5.10 b) shows a higher proportion of domain 2. Based on these two VDFs, it is not possible to determine whether one domain structure occurs more frequently than another.
A HRTEM image of the interface between the substrate and superlattice in $(LSMO/LFO)_{10}/STO$ is depicted in Figure 5.11. The FFTs shown in the top insets suggest that the left and right regions of the HRTEM image has domain 2 and 1 orientation, respectively. This is seen as a doubling of frequencies in the FFT along the $[01\bar{1}]_{pc}$ direction in domain 1 compared to in domain 2. This is in agreement with previous findings in $LFO/STO(111)_c$ [18], and the simulated diffraction patterns for LFO in Figure 5.7 c) and d). The bottom insets show magnified regions of the superlattice/substrate interface. The crystal structures appear different in the two insets, but this could be due to the domain 1 interface not being fully on zone axis. Overall, it is not possible to distinguish differences in the atomic lattice between the superlattice layers in $(LSMO/LFO)_{10}/STO$ based on the HRTEM image in Figure

5.11.

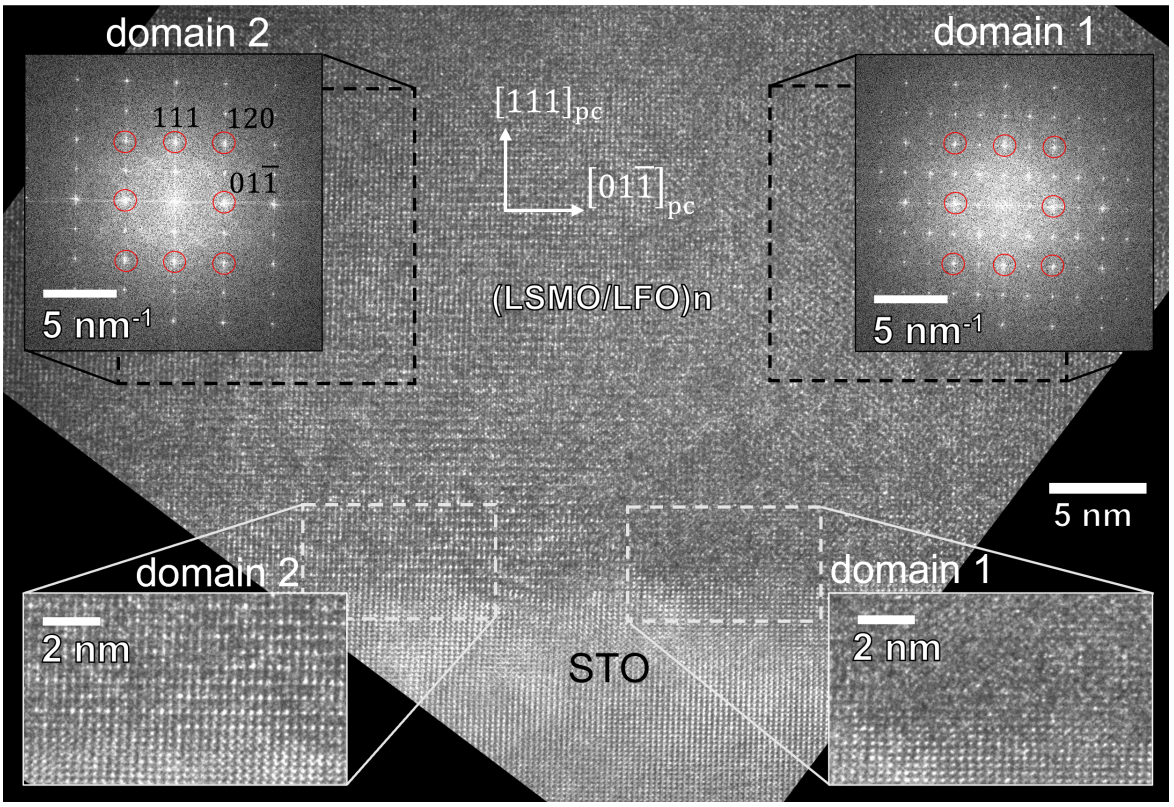

Figure 5.11: HRTEM image of $(LSMO/LFO)_{10}/STO$ acquired along the $[2\bar{1}\bar{1}]_{pc}$ zone axis. FFTs from the structural domains are included as insets at the top of the image, while magnified regions of the LFO/STO interface are shown in the bottom insets. FFT reflections are indexed with pseudocubic indices marked with red circles.

In summary, the crystallographic characterization of $(LSMO/LFO)_{10}/STO$ shows signs of unit cell distortion in LSMO, giving a structure similar to that of LFO in the superlattice. It cannot be determined whether structural distortions are present in LFO. Both domain 1 and domain 2 orientation are observed in both S-SPED data and FFTs from HRTEM images, similarly to previous observations in $LFO/STO(111)_{pc}$ by Christiansen et al. [18].

$(LSMO/LFO)_4/DSO$

The $(LSMO/LFO)_4/DSO$ TEM lamella is cut at a 90°angle relative to $(LSMO/LFO)_{10}/STO$, and is imaged along the $[0\bar{1}1]_{pc}$ zone axis. The periodicity doubling in the $[0\bar{1}1]_{pc}$ direction which defines domain 1 is therefore parallel to the electron beam in the $(LSMO/LFO)_4/DSO$ sample. While traditional TEM and diffraction techniques are unable to image the atomic lattice in this particular direction, HOLZ-STEM methodologies are specifically developed for this.
Figure 5.12 shows VDF images and diffraction patterns from a 4D-HOLZ-STEM scan along approximately 1 µm of the $(LSMO/LFO)_4/DSO$ sample. As domain 1 is defined by having a periodicity doubling parallel to the electron beam relative to domain 2, this orientation is expected to give an extra inner HOLZ ring in the diffraction images compared to domain 2. A virtual annular aperture, indicated in Figure 5.12 a) was placed around the inner HOLZ ring to generate the VDF seen in Figure 5.12 b). This means that only domain 1 scatters to the virtual aperture, and therefore appears bright in the VDF. HOLZ ring doubling in domain 1 relative to domain 2 is shown in Figure 5.12 c) and d). These diffraction images are generated from the regions marked as "domain 1 and domain 2 ROI" in the VDF. The diffraction image from domain 1 displays both a FOLZ and a SOLZ ring, while the diffraction image from domain 2 only displays a FOLZ ring.

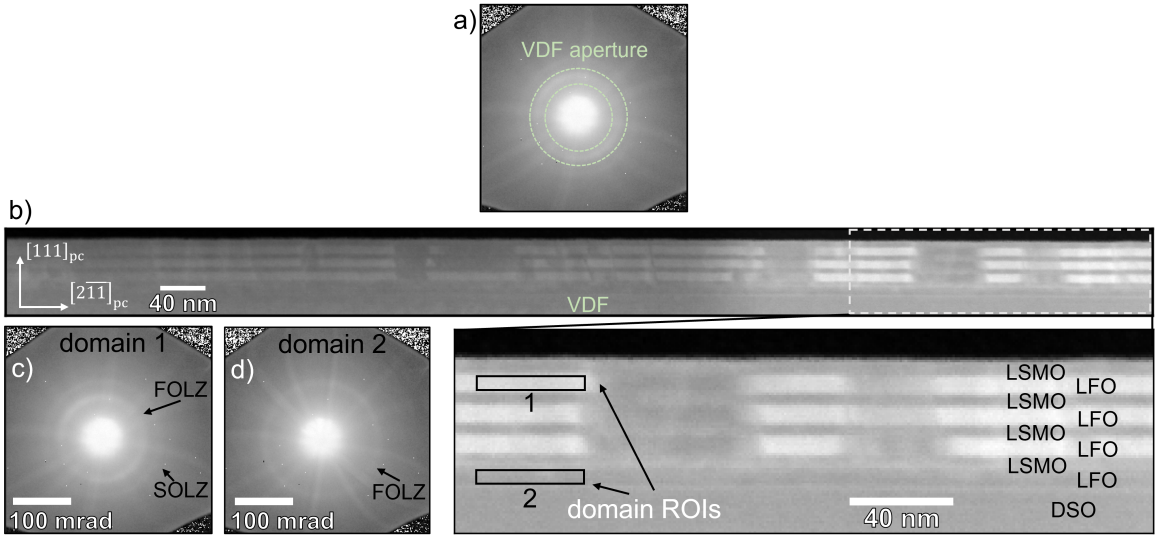

Figure 5.12: a) Placement of the virtual aperture used to generate the VFD. b) VDF image of the superlattice with a magnified region marked by a dashed square. c) and d) HOLZ diffraction images from the two regions of interest marked with black squares on the VDF.

The VDF in Figure 5.12 a) showcases the distribution of domains across the full view of the superlattice. It can be seen from the VDF that the bottom layer of LFO exhibits monodomain growth with a domain 2 orientation along the full region of the imaged superlattice. This is seen as dark contrast throughout the bottom LFO layer. In

the successive layers, LFO shows both domain 1 (bright regions) and domain 2 (dark regions) growth. The domains are separated by vertical domain walls. As DSO has the same crystal symmetry as LFO, it is possible to determine the orientation of DSO using HOLZ-STEM similarly as for LFO. No HOLZ ring doubling is observed in DSO, meaning that DSO is seen along one of the domain 2 orientations in this sample. As it is known from the manufacturer that the DSO substrate is $(101)_o$ oriented, it can be established that the DSO unit cell is seen along either $[\overline{1}12]_o$ or $[1\overline{1}2]_o$ in this sample. Considering that the bottom layer of LFO is also domain 2 oriented, it is likely that the monodomain growth is a result of this orientation being energetically favourable on the DSO substrate. Monodomain growth of LFO on DSO$(111)_{pc}$ has been observed in previous work [21]. Elaborations on the origin of domain growth can be found in section 6.3.
Figure 5.13 shows three different VDF images of the $(LSMO/LFO)_4$/DSO sample, along with diffraction patterns from LFO domain 1 and 2, and the DSO substrate.

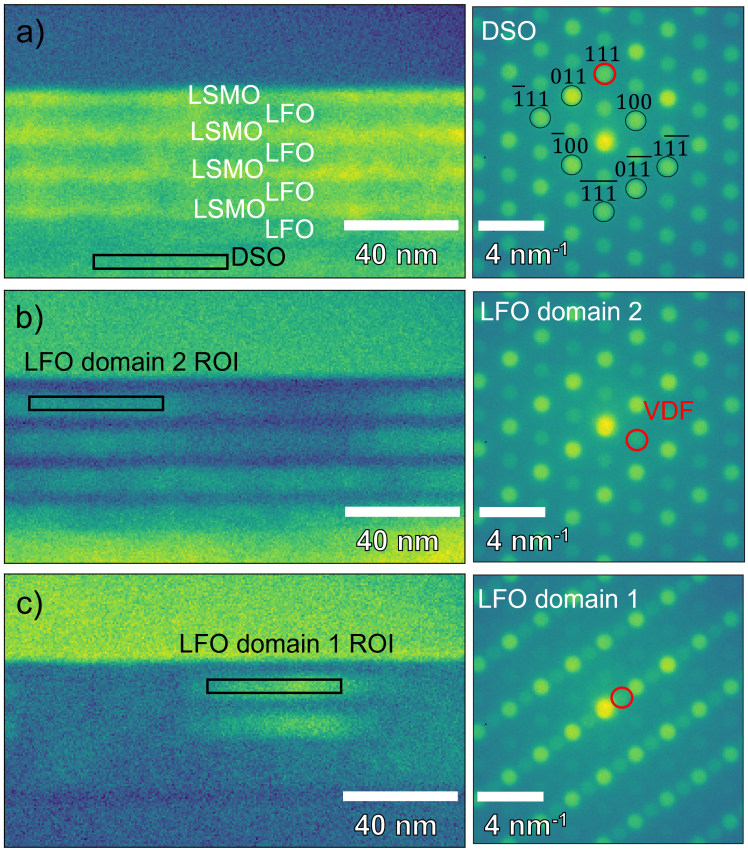

Figure 5.13: S-SPED VDF reconstructions of $(LSMO/LFO)_{10}$/STO acquired in the $[0\bar{1}1]_{pc}$ zone axis with diffraction patterns from regions of interest indicated by with black squares. Red circles indicate diffraction spots used for VDF generation. VDF and diffraction pattern from a) DSO, b) LFO domain 2, c) LFO domain 1.

The VDF in Figure 5.13 b) is created by selecting a reflection exclusively found in the diffraction pattern of LFO (and DSO) domain 2. The bright regions in Figure 5.13 b) therefore correspond to LFO and DSO domain 2 orientation. Likewise, the reflection chosen to generate the VDF in Figure 5.13 c) is exclusive for the domain 1 orientation. Domain 1 LFO appears in the VDF as an intense region in Figure 5.13 b), and as a dark region in Figure 5.13 c). The distribution of LFO domains, featuring domain 2 orientation in the bottom LFO layer and domain 1 orientation in the upper layers, aligns with the distribution observed in the HOLZ-STEM VDF images. The similarity of the diffraction patterns from LFO domain 2 and DSO in Figure 5.13 a) and b) confirms hat LFO and DSO in this region has the same orientation.
The diffraction patterns in Figure 5.13 b) and c) are similar to the simulated diffraction patterns for domain 1 and 2 in Figure 5.7 a) and b) in some respects. Firstly, the reflections in the $[011]_{pc}$ direction are very faint in S-SPED patterns from domain 1 in Figure 5.13 c). Moreover, both S-SPED patterns differ from the ReciPro simulations due to the appearance of extinct reflections. Analogous to the discussion for $(LSMO/LFO)_4/DSO$, this observation could be attributed to either dynamic scattering, structural distortions within LFO, or a combination of these effects.

The remaining question is whether there are structural variations present in LSMO throughout the superlattice. The simulations of the bulk structure of LSMO in Figure 5.8 a) produce degenerate simulated diffraction patterns. Orientation dependent domain growth such as that found in LFO is therefore not expected assuming a bulk-like unit cell symmetry of LSMO. The VDFs of the superlattice in Figure 5.12 b) and Figure 5.13 show that the LFO domains are separated by vertical domain walls, and consistent through the superlattice layers. There are several mechanisms which can explain this vertical domain growth. One theory for the formation of vertical domain walls is that the preferred orientation of successive LFO layers is "translated" through LSMO via some structural coupling mechanism. It is therefore interesting to examine whether LSMO has a different structure depending on the adjacent LFO domain growth. This is investigated in Figure 5.14, where diffraction patterns are generated from regions of interest in each of the LSMO layers, both from layers near domain 1 and near domain 2 LFO.

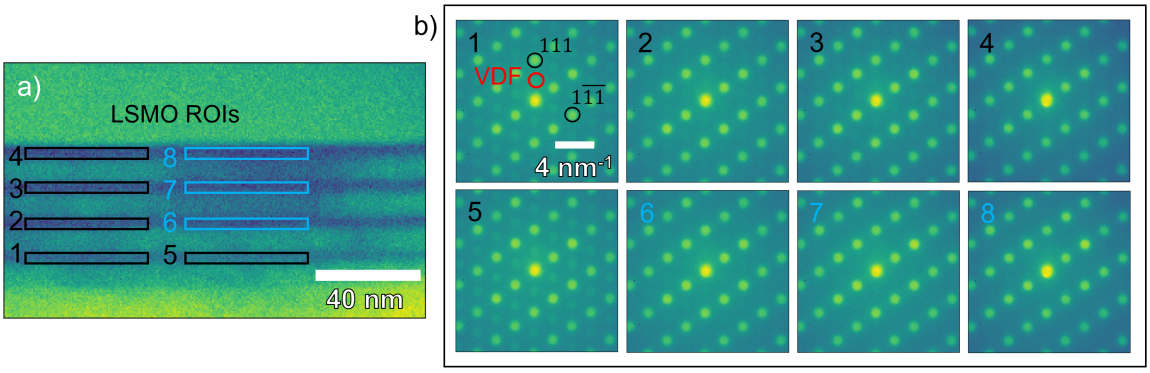

Figure 5.14: a) ROIs where LSMO is in contact with domain 1 LFO are blue, and ROIS where LSMO is in contact with domain 2 LFO are black. b) Diffraction patterns from LSMO layers. The number in the upper left corner annotates the ROI used to generated the diffraction pattern. A red circle marks the diffraction spot used for VDF generation.

The VDF in Figure 5.14 was created by selecting a superreflection between $(000)_{pc}$ and $(111)_{pc}$, exclusive to LFO. LSMO layers therefore appear dark in the VDF. There are no observable changes in the diffraction patterns when comparing LSMO in contact with the two LFO domains. This implies that the structure of LSMO remains unchanged near different LFO domains, suggesting that the vertical domain growth is not a result of structural differences in LSMO. Another explanation for the vertical domain growth is that the domains arise due to the step-and-terrace structure of $(111)_{pc}$ domains. This is addressed in Section 6.3.

An interesting observation in Figure 5.14 is that the diffraction pattern from the bottom layer of LSMO (region 1 and 5) is different from diffraction patterns from the successive layers (region 2-4 and 6-8). All diffraction patterns from regions 2-4 and 6-8 are identical to the simulated diffraction pattern of LSMO in Figure 5.8 a). The diffraction pattern from the bottom LSMO layer differs from the simulated diffraction pattern because it has reflections which are extinct in simulations. This indicates that LSMO in the second, third and fourth layer (region 2-4 and 6-8) has the same structure as bulk LSMO, while the bottom layer has undergone some structural distortion, causing the extinct reflections to appear. It is very unlikely that the appearance of extinct reflections in the bottom LSMO layer is caused by dynamic scattering effects, as the contribution from dynamic scattering is assumed to be approximately equal across the scanned region. Given the relatively small scan area and minimal sample thickness variation in this region, this assumption seems justifiable. It can therefore be assumed that there are structural differences which cause the variations in diffraction patterns in the LSMO layers.

The HRTEM image of $(LSMO/LFO)_4/DSO$ in Figure 5.15 contains multiple interesting features. Firstly, the individual layers of LFO and LSMO can be easily differentiated based on the appearance of their atomic lattices, as opposed to the $(LSMO/LFO)_{10}$ /STO sample in Figure 5.11. In line with all previous results from the crystallographic characterization of $(LSMO/LFO)_4/DSO$, the three top layers LFO have both domain 1 and 2 structure, and the bottom LFO layer displays monodomain growth.

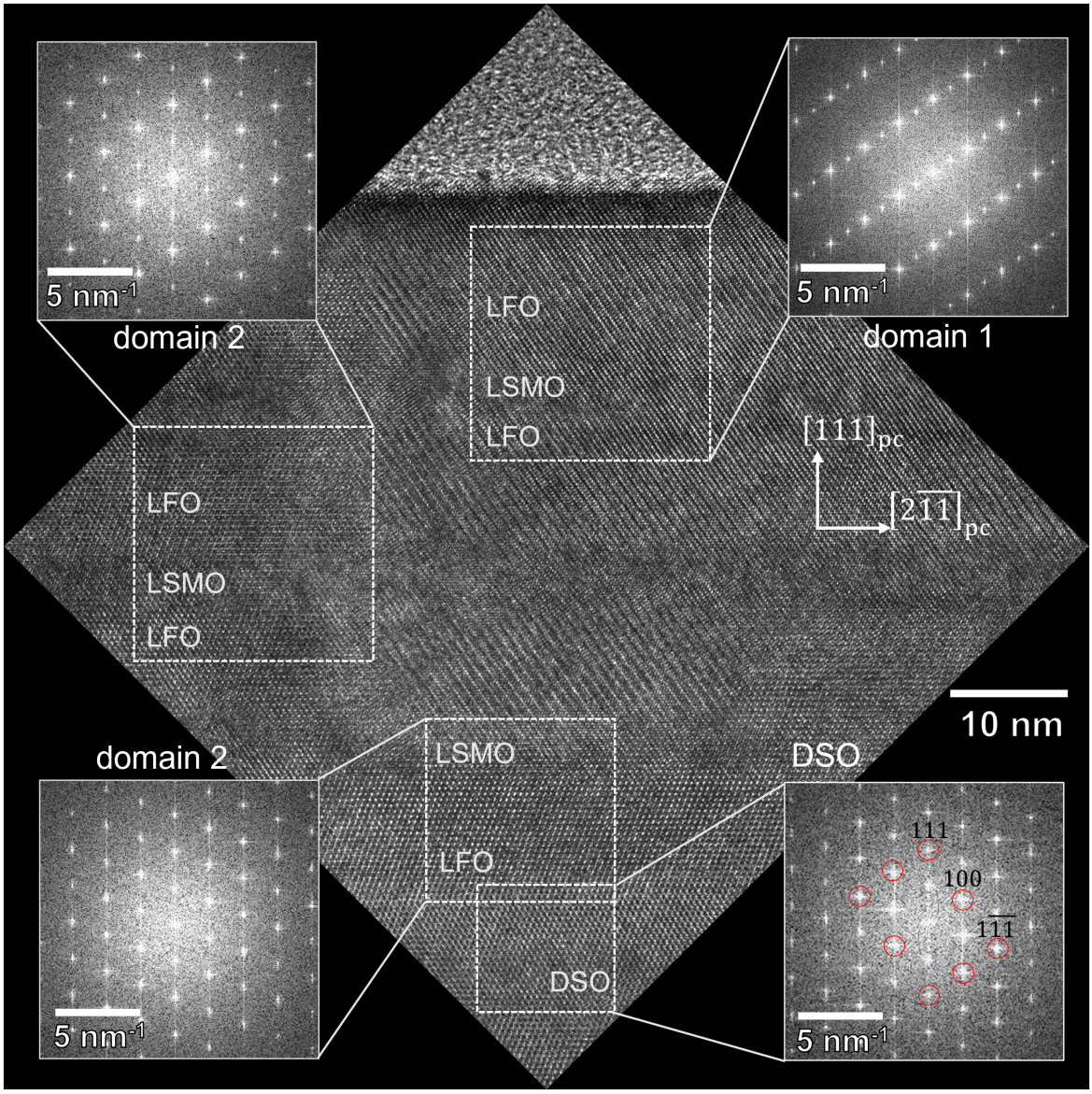

Figure 5.15: HRTEM image of $(LSMO/LFO)_4/DSO$ acquired along the $[0\bar{1}1]_{pc}$ zone axis with FFTs from the the regions of interest indicated by dashed squares. Pseudocubic FFT reflections are indexed and marked with red circles.

The FFTs from the left domain and the bottom LFO layer are consistent with simulated diffraction patterns of domain 2 in Figure 5.7. The FFT from the right region

is not similar to the simulated diffraction pattern for domain 1 LFO, as it misses the rows of reflections in the $[011]_{pc}$ direction. This could suggests that LFO in this region has undergone a structural change, reducing the periodicity in the $[011]_{pc}$ direction compared to the bulk structure. This is in agreement with S-SPED patterns from the same regions in Figure 5.13 c), where the reflections that are non-existent in the FFT have very faint intensities. As the S-SPED pattern from this region is slightly ambiguous, and the FFT could be subject to HRTEM contrast effects, it cannot be determined whether a change in lattice periodicity has occurred in LFO domain 1 or not.
In agreement with previous findings, the bottom LFO layer shows domain 2 orientation, whereas domain 1 orientation appears in the upper layers. A vertical domain wall, marking the boundary between domain 1 and 2 LFO, is visible across three LFO layers on the left side of the image. Although the HRTEM image clearly shows structural differences between domain 1 and domain 2 LFO, no structural differences can be seen between different regions of LSMO in Figure 5.15. A HRTEM image from a separate region of the superlattice underlining this is included in Appendix C.

In summary, the crystallographic characterization of the superlattices revealed different types of structural distortions and domain growth. In $(LSMO/LFO)_{10}$/STO, LSMO had undergone unit cell distortions in all layers. In $(LSMO/LFO)_4$/DSO, only the bottom layer of LSMO displayed structural distortions. It was not possible to determine whether structural changes in LFO occurred or not, as features in the S-SPED data could be interpreted both as a result of dynamic scattering effects or as structural changes compared to the simulated diffraction patterns. Both superlattices displayed domain growth with vertical domain walls. Monodomain growth was found in the bottom layer of LFO in $(LSMO/LFO)_4$/DSO, while successive layers showed multidomain growth.

Chapter 6

Discussion and future work

6.1 S-SPED

It was demonstrated that S-SPED correction did not give noticeable resolution improvement in a dataset recorded with "perfect" instrument alignment. However, this does not render S-SPED generally unnecessary. Inherent probe wandering was detected in all other recorded datasets acquired with "normal" alignment. Significant probe wandering was also reported in the work of Nordahl et al. [15], also detected with "good" instrument alignment. We can therefore assume that probe wandering is likely to be present in a significant portion of "normal" SPED acquisition setups. Moreover, it was demonstrated that S-SPED can significantly improve resolution in data acquired with different types of misalignment. Having a method that makes SPED more robust against instrument misalignment is beneficial in several ways. Firstly, it could alleviate the rigorous alignment requirement for SPED, potentially liberating time and making data acquisition more effective. Secondly, robustness against misalignments could make SPED more available to less experienced operators, as manually aligning 8 VBF images in the post-acquisition process is arguably less demanding than performing accurate SPED alignment. When imaging beam sensitive materials, alignment adjustments cannot be performed at the region of interest, as this can lead to beam damage near important features. SPED acquisition of beam sensitive materials are therefore often done "blindly". Post-acquisition aberration correction through S-SPED application is therefore useful to make this type of acquisition more robust against misalignment and local variations in sample height.

Automatic VBF alignment

In their work, Nordahl et al. [15] employed SmartAlign software [59] to perform rigid alignment of the segment VBF images. In this thesis, the built-in HyperSpy function `estimate_shift_2D()` [60] was tested for automatic rigid alignment of the VBF images. The method did not perform satisfactory alignment compared to manual image alignment. This was most likely due to the lack of detectable features in the X-direction of the VBF images of the superlattices. Additionally, it is possible that

varying diffraction contrast between the segments due to fulfilment of different diffraction conditions for the different incident beam angles made feature detection more complicated. As such, automatic rigid alignment in S-SPED is most likely feasible for samples with well defines edges such as nanoparticles. For the future, especially if a larger number of segments are acquired, it could be convenient to develop an automatic method to track feature movement for S-SPED correction.

Quantification of intensity line profile slope

In this work, the steepness of the slope of intensity line profiles across interfaces with different contrast was used to compare the resolution enhancements in S-SPED datasets. In these plots, significant changes in slope steepness were observed, and this was deemed sufficient to qualitatively demonstrate resolution improvements. For future work, a more precise approach would be to quantify the differences in slope steepness, for instance by utilizing curve fitting. Nordahl et al. did this using a least squares method with an artcan function for similar intensity line plots [15].

Number of segments in S-SPED

As demonstrated in Section 4.3, the resolution improvement achievable with S-SPED correction increases with the number of segments recorded. For future work, it would be interesting to record S-SPED data with single-probe integration paths. Theoretically, this would produce images with a resolution close to NBD-SED, but with the added benefits of high quality diffraction patterns due to precession. With the same parameters as utilized in this work, Nordahl et al. [15] calculated this number to be $n = 46$ segments. Although this is time and memory consuming, acquisition of 46 segments is feasible by changing the precession frequency and/or scan time in order to achieve sufficient diffraction intensity. This would be an interesting experiment future exploration of S-SPED.

6.2 EELS

Pre-edge background removal

In the background subtraction procedure conducted in the EELS data processing, a Hydrogenic GOS model was utilized for curve fitting [55]. As this approximation could not model the $M_{4,5}$-edges of La and Dy, the relative intensities of these core loss edges could not be compared with the core loss intensities of the other elements in the samples. In order to perform more precise curve fitting and include all core loss edges, it would be beneficial to utilize a Hartree-Slater wave function approximation [56]. While this was not available during the EELS data processing for this study, it would be advantageous for future EELS work.

Energy spread of incident beam

During the EELS acquisition sessions, the FWHM of the ZLP was measured to monitor the energy spread of the incident beam. In the two session, the FWHM was measured to 3.05 eV and 3.16 eV, which is significantly larger than expected when using a CFEG instrument like the *JEOL ARM200F*. A FWHM of < 1 eV is routinely achieved with this instrument [61]. However, other operators of the *JEOL ARM200F* observed a broader than normal FWHM during the time period of the acquisition. No explanation was found for the unusually large energy spread of the incident beam.

White-line ratio of Fe-$L_{2,3}$

It has been demonstrated by Tan et al. that the white-line ratio of Fe-$L_{2,3}$ does not increase monotonously with the oxidation state of Fe, as it does for Mn-$L_{2,3}$ [42]. However, the white-line ratio of Fe-$L_{2,3}$ peaks does change for different oxidation states, but without following any systematic trend [42]. It was therefore determined that it was useful to measure the white-line ratios of Fe-$L_{2,3}$ in order to detect possible relative changes in oxidation state. If the white-line ratio of Fe-$L_{2,3}$ had varied in the samples, this would have been an indication of changes in the oxidation state. However, it is difficult to determine whether the lack of any observed changes in the white-line ratio of Fe-$L_{2,3}$ was due to a stable oxidation state or insensitivity of the method.

Oxygen vacancy formation and TM oxidation state

A surprising finding in all EELS results was that no difference in the white-line ratio of the Mn-$L_{2,3}$ edge occurred in neither superlattice in regions where there were signs of oxygen vacancies in the spectral features of the O-K edge. Mn is expected to undergo a reduction in oxidation state during the creation of oxygen vacancies due to charge neutrality [45]. This indicates that oxygen vacancies formed independently from the TM ions. Further studies are needed to investigate the formation of oxygen vacancies in the superlattices.

6.3 Crystallography

Resolution in S-SPED data from (LSMO/LFO)$_{10}$/STO

The interpretation of the S-SPED data presented in Figure 5.9 was based on the assumption that the single layers were resolved, and that the diffraction information did indeed come from LFO and LSMO, separately. Firstly, individual layer resolution in this dataset was demonstrated through the VDF contrast in Figure 4.3 and 5.11. This single layer contrast was obtained by selecting the edge of the $(111)_{pc}$ reflection. The varying contrast between the layers was attributed to slight movements of this reflection due to the variation of the $(111)_{pc}$ plane separation between LSMO and LFO. The single layer contrast exhibited in these VDF images thus demonstrated that structural in single layers were present in (LSMO/LFO)$_{10}$/STO, and that S-SPED

application could resolve single layers.
However, the similarity between the diffraction patterns in LSMO and LFO could also be caused by structural mixing of the superlattice layers. Layer mixing, possibly due to 3D growth, was only detected in upper superlattice layers, while lower layers were demonstrated to be chemically distinct in EELS scans. The regions of interest for diffraction analysis were therefore selected from the lower layers in order to minimize contributions from layer mixing. Moreover, diffraction patterns from smaller regions of interest, down to single probe positions were inspected in both layers, showing the same similarity in diffraction patterns from LSMO and LFO. This approach was outlined in Section 3.3. While it cannot be definitively stated that all sample positions within the ROIs in Figure 5.9 were solely LSMO or LFO, it is reasonable to assume that potential contributions to the diffraction pattern the other superlattice material would be relatively small.

Origin of domain growth

The following information is obtained through discussions with Hallsteinsen and Liu, the creators of the superlattices, as PLD growth is not my primary field of research. The different domain growth seen between the samples can be explained by considering the surface symmetry of the substrates. In DSO$(111)_{pc}$, the substrate surface symmetry is pseudo-hexagonal with buckled hexagons. As the LFO$(111)_{pc}$ surface is also pseudo-hexagonal, certain orientations of LFO are expected to be energetically favoured on this substrate, dictating the initial growth. The orientation of the monodomain LFO layer on (LSMO/LFO)$_4$/DSO most likely represents the lowest-energy configuration of the buckled hexagons. However, on the hexagonal STO$(111)_c$ surface, all three rotations of the LFO unit cell is expected to be geometrically and energetically equal. There is therefore no energetically preferred orientation during initial growth of LFO on STO$(111)_c$. This could explain why multiple orientations were present in the bottom layer of LFO on STO$(111)_c$, while only one orientation was present in the bottom layer on DSO$(111)_{pc}$. (LSMO/LFO)$_{10}$/STO.
Not all types of domain growth is expected to give vertical domain walls like the ones observed in the superlattices. It is possible that some "directional" coupling mechanism such as octahedral tilt are responsible for vertical domain growth, but no signs of this was detected in the crystallographic analysis. A more plausible theory is that the vertical domain walls are a result of the atomic step-and-terrace structure characteristic for $(111)_{pc}$ substrates [62]. It is possible that the unit cell orientation of initial atomic layers differs on either side of an atomic step. As the step is transferred to successive layers through layer-by-layer growth, a vertical domain wall is formed between the two orientations.

Crystallographic characterization future work

Differentiating between the orthorombic $(101)_o$ and $(011)_o$ orientations in LFO is important to make predictions about the magnetic properties of the samples [21]. It was not possible to determine the orientation of LFO with the techniques used in this work.

However, there are other approaches which can determine the orientation of LFO. The alternating displacement of La-ions makes the La atomic column appear elongated in the direction of ion modulation. The direction of this elongation differs between the $(101)_o$ and $(011)_o$ orientations of LFO. This can be seen in the schematic in Figure 5.6 in Section 5.2.3. By imaging the lattice using STEM-HAADF, it is possible to differentiate between the two orientations based on the eccentricity of the La atomic column. In previous work by Hallsteinsen et al., the HyperSpy package Atomap [63] was utilized to measure the eccentricity of the La-columns in STEM-HAADF images of LSMO/LFO/STO$(111)_c$ [13].
In this work, 4D-HOLZ-STEM imaging was used to identify domains which exhibited lattice periodicity doubling along the electron beam by detection of HOLZ ring doubling. However, it is plausible that other types of information can be extracted from this dataset. Previous research has shown that a varying intensity of the HOLZ rings could be used to map atomic shifts [37]. Analysis of the HOLZ ring intensities and other potentially interesting properties was not conducted in this work due to time limitations. Overall, a more comprehensive analysis of the STEM-HOLZ dataset may potentially reveal additional interesting information about the crystal structures in the samples in future work.
Hallsteinsen et al. demonstrated that atomic reconstructions due to incompatible octahedral rotations occurred in an LSMO/LFO/STO$(111)_c$ bilayer [13]. Similar modulations of octahedral tilt and rotation at perovskite oxide heterointerfaces has been observed in multiple studies [7]. Given that $(\text{LSMO/LFO})_{10}$/STO and $(\text{LSMO/LFO})_4$ /DSO each have 19 and 7 epitaxial heterointerfaces, respectively, several with incompatible octahedral tilt patterns, changes to the octahedral tilt patterns are likely to occur in the superlattices. It was not possible to directly image octahedral tilt with the techniques utilized in this work. However, high-resolution STEM-ABF has been used previously to directly image the oxygen lattice in perovskite oxides [63]. It would be very interesting to apply this technique on the studied superlattice systems for exploration of possible octahedral tilt modulation at the interfaces.
This work was conducted with cross-section TEM samples. Along the zone axes of both samples, the orientations giving domain 2 diffraction patterns were degenerate. The true distribution of domains in the superlattices could therefore not be determined. Diffraction experiments with plan-view samples would be useful to image the size and distribution of the domains in the superlattices. In the direction perpendicular to the superlattice surface, the three orientations of the orthorombic unit cells produces different diffraction patterns. This has been done previously, using conventional TEM-DF imaging to create a DF mosaic image of domains in LFO/STO$(111)_c$ [18]. This would be an interesting technique to apply for future exploration of the superlattice domains. It would be especially interesting to perform plan-view DF imaging of $(\text{LSMO/LFO})_4$/DSO, as no equivalent imaging of LFO/DSO$(111)_{pc}$ has been performed previously.

6.4 Future magnetic characterization

Perovskite oxide superlattice systems exhibit extraordinarily complicated physics [6]. Multiple coupling mechanisms, confinement effects and interface phenomena may occur across the alternating FM LFO and AFM LSMO layers in the studied superlattices. It is outside the scope of this work to predict the impact of the structural, chemical and electronic findings in this work on the functional properties of the materials. However, a few assumptions can be made. Interdiffusion of Fe in both superlattices, layer intermixing in $(LSMO/LFO)_{10}/STO$ and the proposed change in Mn oxidation state in LSMO layers in $(LSMO/LFO)_4/DSO$ are findings which are expected to disrupt double-exchange in LSMO and super-exchange in LFO. Additionally, unit cell distortion and strain effects in both superlattices could imply a change the Mn - O - Mn and Fe - O - Fe bond angle, which is important for magnetic exchange mechanisms. The next step in studying these material systems should therefore involve characterization of their functional properties, specifically focusing on magnetic behaviour. It would then be very interesting to relate the functional properties to the findings that have been presented in this thesis.

Chapter 7

Conclusion

In this thesis, two perovskite oxide superlattices were studied using a range of TEM techniques. Additionally, the new S-SPED technique was tested and developed to achieve improved resolution in both real and reciprocal space.
S-SPED was tested on normally aligned and intentionally misaligned data, and the effect of the number of segments was investigated. It was determined that acquiring 8 segments struck a favorable compromise between data size, acquisition time, and resolution improvement. Significant resolution improvement was observed in well aligned and misaligned datasets by applying S-SPED correction. However, S-SPED correction resulted in negligible resolution enhancement in a "perfectly aligned" dataset compared to "normally" aligned datasets. Nevertheless, the capability of S-SPED to enhance resolution and provide robustness against instrument misalignments through reduction of probe wandering was demonstrated. Notably, the application of the S-SPED methodology was critical to the crystallographic characterization of the superlattices studied in this work.
STEM-EELS, HRTEM, HOLZ-STEM and S-SPED was used to study the chemical composition and crystal structure of $(LSMO/LFO)_{10}/STO$ and $(LSMO/LFO)_4/DSO$. $(LSMO/LFO)_4/DSO$ exhibited chemically distinct layers throughout the superlattice, while $(LSMO/LFO)_{10}/STO$ displayed some intermixing of layers, potentially due to 3D growth. Significant interdiffusion of Fe into LSMO was detected in both superlattices. The ELNES at the O-K edge in both superlattices suggested the presence of oxygen vacancies. In $(LSMO/LFO)_{10}/STO$ this was found in multiple layers, both near the STO substrate and close to the amorphous protection layer. In $(LSMO/LFO)_4/DSO$, signs of oxygen vacancies were only observed in the bottom LFO layer. In $(LSMO/LFO)_4/DSO$, a gradual shift of the Mn-L_3 ionization edge onset energy was observed in multiple LSMO layers and attributed to a possible change in the relative concentration of Mn^{3+} and Mn^{4+} within the layers.
Crystallographic analysis uncovered structural coupling throughout the $(LSMO/LFO)_{10}/STO$ superlattice, as LSMO had undergone unit cell distortions and adopted a similar unit cell structure to LFO. In $(LSMO/LFO)_4/DSO$, unit cell distortion was found in the bottom layer of LSMO, while the subsequent LSMO layers maintained their bulk structure. At least two structural domains were identified in both superlattices,

corresponding to different orientations of the orthorombic unit cell on the $(111)_{pc}$ substrates. In $(LSMO/LFO)_4$/DSO the bottom LFO layer showed monodomain growth in the same orientation as DSO. The coherent vertical domain walls in both superlattices were attributed to the atomic step-and-terrace structure of the $(111)_{pc}$ substrates. Overall, intriguing discoveries about the structural and chemical conditions in the superlattice have been made. This was done using multiple TEM techniques, including the new S-SPED methodology.

References

[1] J. D. Hunter. 'Matplotlib: A 2D graphics environment'. In: *Computing in Science & Engineering* 9.3 (2007), pp. 90–95.

[2] Inkscape Project. *Inkscape*. Version 0.92.5. 2020.

[3] Magnus Själander et al. 'EPIC: An Energy-Efficient, High-Performance GPGPU Computing Research Infrastructure'. In: *arXiv:1912.05848 [cs]* (2019).

[4] R Stanley Williams. 'What's Next? The end of Moore's law'. In: *Computing in Science & Engineering* 19.2 (2017), pp. 7–13.

[5] Qingkai Tang and Xinhua Zhu. 'Half-metallic double perovskite oxides: recent developments and future perspectives'. In: *Journal of Materials Chemistry C* (2022).

[6] Ramamoorthy Ramesh and Darrell G Schlom. 'Creating emergent phenomena in oxide superlattices'. In: *Nature Reviews Materials* 4.4 (2019), pp. 257–268.

[7] Pavlo Zubko et al. 'Interface physics in complex oxide heterostructures'. In: *Annu. Rev. Condens. Matter Phys.* 2.1 (2011), pp. 141–165.

[8] PA Salvador et al. 'Growth and magnetoresistive properties of ($LaMnO_3$)m/($SrMnO_3$)n superlattices'. In: *Applied physics letters* 75.17 (1999), pp. 2638–2640.

[9] A Bhattacharya et al. 'Metal-insulator transition and its relation to magnetic structure in ($LaMnO_3$)2 n/($SrMnO_3$) n superlattices'. In: *Physical review letters* 100.25 (2008), p. 257203.

[10] Eric Bousquet et al. 'Improper ferroelectricity in perovskite oxide artificial superlattices'. In: *Nature* 452.7188 (2008), pp. 732–736.

[11] Pablo Aguado-Puente et al. 'Structural and energetic properties of domains in $PbTiO_3$/$SrTiO_3$ superlattices from first principles'. In: *Physical Review B* 85.18 (2012), p. 184105.

[12] Zijian Hong et al. 'Stability of polar vortex lattice in ferroelectric superlattices'. In: *Nano letters* 17.4 (2017), pp. 2246–2252.

[13] I Hallsteinsen et al. 'Concurrent magnetic and structural reconstructions at the interface of (111) oriented $La_{0.7}Sr_{0.3}MnO_3$/$LaFeO_3$'. In: *Physical Review B* 94.20 (2016), p. 201115.

[14] Jonathan S Barnard et al. 'High-resolution scanning precession electron diffraction: Alignment and spatial resolution'. In: *Ultramicroscopy* 174 (2017), pp. 79–88.

[15] Gregory Nordahl et al. 'Correcting for probe wandering by precession path segmentation'. In: *Ultramicroscopy* 248 (2023), p. 113715.

[16] Charles Kittel. *Introduction to Solid State Physics*. 8th ed. Wiley, 2004.

[17] T Bolstad et al. 'Effect of (1 1 1)-oriented strain on the structure and magnetic properties of $La_{0.7}Sr_{0.3}MnO_3$ thin films'. In: *Journal of Physics: Condensed Matter* 30.25 (2018), p. 255702.

[18] E Christiansen et al. 'Structural investigation of epitaxial $LaFeO_3$ thin films on (111) oriented $SrTiO_3$ by transmission electron microscopy'. In: *Journal of Physics: Conference Series*. Vol. 644. 1. IOP Publishing. 2015.

[19] Sheng-Qiang Wu et al. 'B-site ordering and strain-induced phase transition in double-perovskite La2NiMnO6 films'. In: *Scientific reports* 8.1 (2018), p. 2516.

[20] SJ Hibble et al. 'Local distortions in the colossal magnetoresistive manganates $La_{0.7}Ca_{0.3}MnO_3$, $La_{0.8}Ca_{0.2}MnO_3$ and $La_{0.7}Sr_{0.3}MnO_3$ revealed by total neutron diffraction'. In: *Journal of Physics: Condensed Matter* 11.47 (1999), p. 9221.

[21] Kristoffer Kjærnes et al. 'Uniaxial Néel vector control in perovskite oxide thin films by anisotropic strain engineering'. In: *Physical Review B* 103.22 (2021), p. 224435.

[22] Lianxu Ye et al. 'Epitaxial (110)-oriented $La_{0.7}Sr_{0.3}MnO_3$ film directly on flexible mica substrate'. In: *Journal of Physics D: Applied Physics* 55.22 (2022), p. 224002.

[23] Céline Lichtensteiger. 'InteractiveXRDFit: a new tool to simulate and fit X-ray diffractograms of oxide thin films and heterostructures'. In: *Journal of applied crystallography* 51.Pt 6 (2018), p. 1745.

[24] *SurfaceNet*. https://surfacenet.de/files/start.php. Accessed: 10.06.2023.

[25] Koichi Momma and Fujio Izumi. 'VESTA: a three-dimensional visualization system for electronic and structural analysis'. In: *Journal of Applied crystallography* 41.3 (2008), pp. 653–658.

[26] Stephen Blundell. *Magnetism in Condensed Matter*. 2003.

[27] X Ke et al. 'Low temperature magnetism in the perovskite substrate $DyScO_3$'. In: *Applied Physics Letters* 94.15 (2009), p. 152503.

[28] Jin Won Seo et al. 'Antiferromagnetic $LaFeO_3$ thin films and their effect on exchange bias'. In: *Journal of Physics: Condensed Matter* 20.26 (2008), p. 264014.

[29] M Cesaria et al. 'LSMO-growing opportunities by PLD and applications in spintronics'. In: *Journal of Physics: Conference Series*. Vol. 292. 1. IOP Publishing. 2011, p. 012003.

[30] David B Williams and C Barry Carter. 'Transmission electron microscopy'. In: *Systematic Materials Analysis* 4 (1978), pp. 407–432.

[31] Alexander S Eggeman and Paul A Midgley. 'Precession electron diffraction'. In: *Advances in Imaging and Electron Physics*. Vol. 170. Elsevier, 2012, pp. 1–63.

[32] *MerlinEM Direct Electron Detector*. https://quantumdetectors.com/products/merlinem/. Accessed: 15.11.2022.

[33] R Vincent and PA Midgley. 'Double conical beam-rocking system for measurement of integrated electron diffraction intensities'. In: *Ultramicroscopy* 53.3 (1994), pp. 271–282.

[34] Alexander S Eggeman et al. 'Aberration-corrected and energy-filtered precession electron diffraction'. In: (2013).

[35] F-T Huang et al. 'Scanning transmission electron microscopy using selective high-order Laue zones: Three-dimensional atomic ordering in sodium cobaltate'. In: *Physical review letters* 105.12 (2010), p. 125502.

[36] Magnus Nord et al. 'Three-dimensional subnanoscale imaging of unit cell doubling due to octahedral tilting and cation modulation in strained perovskite thin films'. In: *Physical Review Materials* 3.6 (2019), p. 063605.

[37] Magnus Nord et al. 'Atomic resolution HOLZ-STEM imaging of atom position modulation in oxide heterostructures'. In: *Ultramicroscopy* 226 (2021), p. 113296.

[38] Ray F Egerton. *Electron energy-loss spectroscopy in the electron microscope*. Springer Science & Business Media, 2011.

[39] C Ricolleau et al. 'Performances of a cold FEG microscope with an objective lens aberration corrector'. In: ().

[40] RF Egerton and M Malac. 'EELS in the TEM'. In: *Journal of Electron Spectroscopy and Related Phenomena* 143.2-3 (2005), pp. 43–50.

[41] Katherine E MacArthur et al. 'Probing the effect of electron channelling on atomic resolution energy dispersive X-ray quantification'. In: *Ultramicroscopy* 182 (2017), pp. 264–275.

[42] Haiyan Tan et al. 'Oxidation state and chemical shift investigation in transition metal oxides by EELS'. In: *Ultramicroscopy* 116 (2012), pp. 24–33.

[43] Robert A Lawrence et al. 'Effects of Multiple Local Environments on Electron Energy Loss Spectra of Epitaxial Perovskite Interfaces'. In: *The Journal of Physical Chemistry C* (2022).

[44] Lide Yao et al. 'Electron-Beam-Induced Perovskite–Brownmillerite–Perovskite Structural Phase Transitions in Epitaxial $La_{0.7}Ca_{0.3}MnO_3$'. In: *Advanced Materials* 26.18 (2014), pp. 2789–2793.

[45] Naoyuki Nakagawa, Harold Y Hwang and David A Muller. 'Why some interfaces cannot be sharp'. In: *Nature materials* 5.3 (2006), pp. 204–209.

[46] *EELS atlas*. https://eels.info/atlas. Accessed: 15.10.2022.

[47] Yusuke Seto et al. 'ReciPro: free and open-source multipurpose crystallographic software integrating a crystal model database and viewer, diffraction and microscopy simulators, and diffraction data analysis tools'. In: *Journal of Applied Crystallography* 55.2 (2022).

[48] V-DH Hou. 'Reduce correlated noise in EELS spectrum with high quality dark reference'. In: *Microscopy and Microanalysis* 15.S2 (2009), pp. 226–227.

[49] Francisco De La Peña et al. 'Hyperspy/Hyperspy: Hyperspy 1.1. 2'. In: *Zenodo* (2019).

[50] DN Johnstone et al. 'pyxem/pyxem: pyxem 0.13. 2 (Version v0. 13.2)'. In: *Zenodo. https://doi. org/10.5281/zenodo* 4687011 (2021).

[51] *DigitalMicrograph Software*. https://www.gatan.com/products/tem-analysis/gatan-microscopy-suite-software. Accessed: 02.02.2023.

[52] John M Cowley and A F Moodie. 'The scattering of electrons by atoms and crystals. I. A new theoretical approach'. In: *Acta Crystallographica* 10.10 (1957), pp. 609–619.

[53] *Signal1D tools: Spike removal*. http://hyperspy.org/hyperspy-doc/current/user guide/signal1d.html. Accessed: 15.05.2023.

[54] Kayleigh LY Fung et al. 'Accurate EELS background subtraction–an adaptable method in MATLAB'. In: *Ultramicroscopy* 217 (2020), p. 113052.

[55] *Model fitting: Fitting multidimensional datasets*. http://hyperspy.org/hyperspy-doc/current/user_guide/model.html. Accessed: 15.05.2023.

[56] RD Leapman, P Rez and DF Mayers. 'K, L, and M shell generalized oscillator strengths and ionization cross sections for fast electron collisions'. In: *The Journal of Chemical Physics* 72.2 (1980), pp. 1232–1243.

[57] *Signal2D tools: Signal registration and alignment*. https://hyperspy.org/hyperspy-doc/current/user_guide/signal2d.html. Accessed: 15.05.2023.

[58] *Dask: dask.array.roll*. https://docs.dask.org/en/stable/generated/dask.array.roll .html. Accessed: 15.05.2023.

[59] Lewys Jones et al. 'Smart Align—a new tool for robust non-rigid registration of scanning microscope data'. In: *Advanced Structural and Chemical Imaging* 1.1 (2015), pp. 1–16.

[60] *Signal2D Tools: Signal registration and alignment*. https://hyperspy.org/hyperspy-doc/current/user_guide/signal2d.html. Accessed: 10.04.2023.

[61] GW Paterson et al. 'Electron energy loss spectroscopy of a chiral plasmonic structure'. In: *Journal of Physics: Conference Series*. Vol. 644. 1. IOP Publishing. 2015, p. 012005.

[62] Ingrid Hallsteinsen et al. 'Effect of polar (111) oriented SrTiO3 on initial perovskite growth'. In: *Crystal Growth & Design* 16.4 (2016), pp. 2357–2362.

[63] Magnus Nord et al. ‘Atomap: a new software tool for the automated analysis of atomic resolution images using two-dimensional Gaussian fitting’. In: *Advanced structural and chemical imaging* 3.1 (2017), pp. 1–12.

Appendix A

PLD growth parameters

The following descriptions are based on information from Ingrid Hallsteinsen and Yu Lui. $(111)_{pc}$ oriented growth substrates such as STO$(111)_c$ and DSO$(101)_o$ require special surface preparation due to the polarity of the $(111)_{pc}$ surface [62]. DSO and STO were therefore prepared by the method described in ref. [62] to stabilize the interface prior to deposition.
For (LSMO/LFO)4/DSO, $La0.7Sr_{0.3}MnO_3$ and $LaFeO_3$ targets were utilized with a target-substrate separation of 50 mm and a growth temperature of 580 °C. The deposition involved 997 laser pulses for LFO and 400 for LSMO, each executed 4 times at a fluency of 1.9J/cm^2. The growth pressure was set at 0.266 mbar O_2, with post-annealing conducted with a 100 mbar O_2 pressure. As for the $(LSMO/LFO)_{10}$/STO superlattice, it was grown by PLD in 2017, and a TEM lamella was created from this thin film as a "plan B" sample to be studied in this thesis during a period when the PLD was not operational. Consequently, it was not possible to obtain the specific PLD growth parameters for this sample.

Appendix B

Interdiffused Fe

Plots of the Fe-$L_{2,3}$ peaks and corresponding white-line ratios of interdiffused Fe found in LSMO in both superlattices are shown in Figure B.1. There is no systematic difference between Fe in LFO and Fe in LSMO in neither of the superlattices, suggesting that the no change of oxidation state in Fe is associated with diffusion.

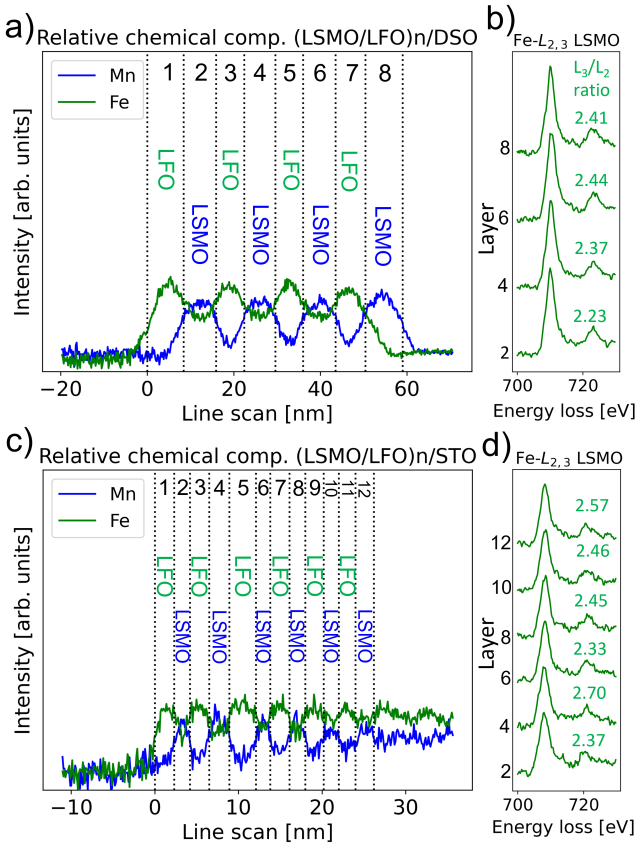

Figure B.1: a) Overview of $(LSMO/LFO)_4/DSO$ EELS chemical composition line scan. b) Fe-$L_{2,3}$ peaks and white-line ratios from LSMO regions. c) Overview of $(LSMO/LFO)_{10}/STO$ EELS chemical composition line scan. d) Fe-$L_{2,3}$ peaks and white-line rations from LSMO regions.

Appendix C

Crystallographic characterization

Figure C.1 shows a HRTEM image suggesting that the LSMO lattice appears similar in proximity of different LFO domains.

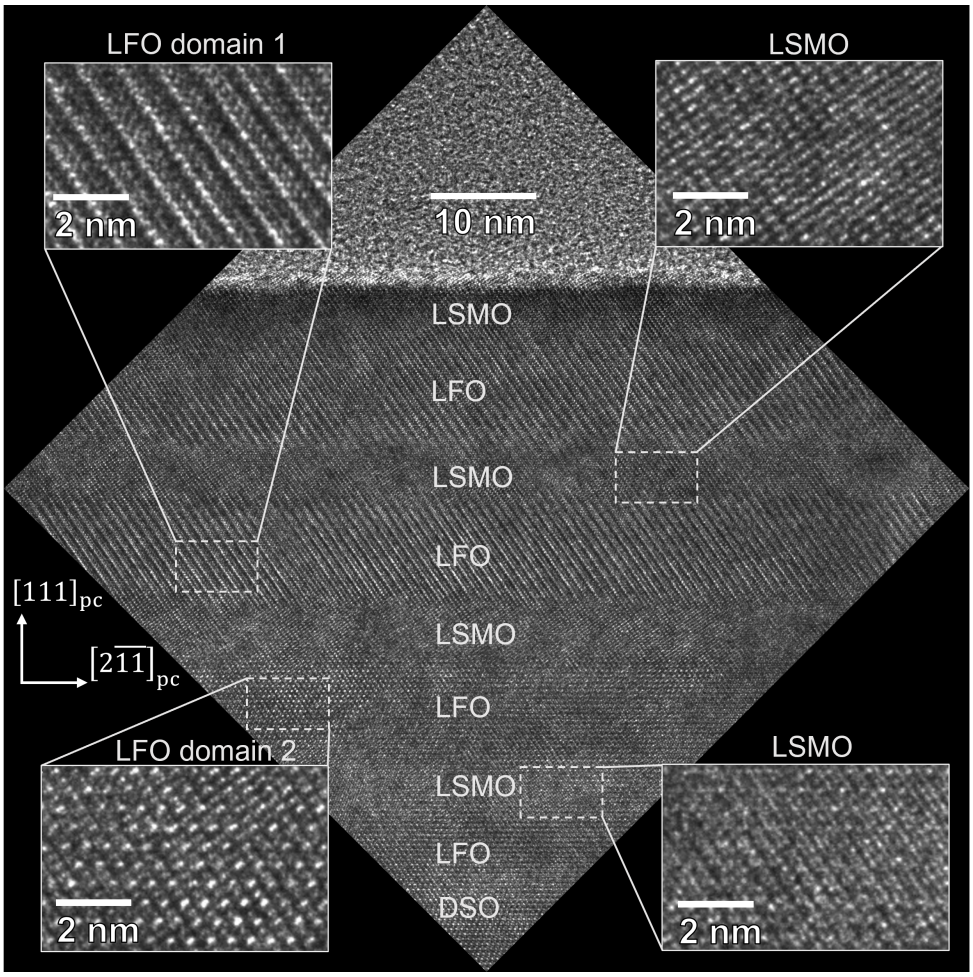

Figure C.1: HRTEM image of $(LSMO/LFO)_4/DSO$ superlattice imaged along the $[0\bar{1}1]_{pc}$ zone axis.

Appendix D

Code

The following code is selected to demonstrate the main data analysis steps performed in STEM-EELS and S-SPED work. For conciseness, recurring operations are only included once, and otherwise indicated with a comment. Processing steps which were run on the NTNU HPC cluster IDUN are indicated with the comment `#run on IDUN`. A batch script utilized to submit a Python job to the IDUN queue manager is also included.

D.1 IDUN batch script

```
#!/bin/bash
#SBATCH --job-name="FileConversion 8SSPED"    # Job name
#SBATCH --account=share-nv-fys-tem    # Account for consumed resources
#SBATCH --nodes=1                # Allocate 1 nodes for the job
#SBATCH --time=00-20:00:00     # Upper time limit for the job (DD-HH:MM:SS)
#SBATCH --mem=30000
#SBATCH --partition=CPUQ
#SBATCH --output=output.out
#SBATCH --mail-user=susanabo@ntnu.no

cd ${SLURM_SUBMIT_DIR}
echo "Echo!"

module purge
module load intel/2020b
module load Python/3.8.6-GCCcore-10.2.0


pythonpath='/cluster/projects/itea_lille-nv-fys-tem/miniconda3/envs/pyxem-dev/bin/
    python'
${pythonpath} FileConversion.py *.mib
```

D.2 S-SPED

D.2.1 S-SPED correction and initial processing

```
#### FILE CONVERSION AND SEGMENT SLICING ####
#Run on IDUN
import hyperspy.api as hs
import matplotlib.pyplot as plt
import dask.array as da
from skimage import feature
import numpy as np
import scipy as sc
import math
import pyxem as pxm

filename='SSPED8_265x160_12x2_0p920x0p926nm_CL12cm_NBD_alpha5_spot0p5nm
_1deg_100Hz_10ms_1p25msFrameTime_50msFBD_332degRot_Thick.mib'
s = pxm.load_mib(filename, reshape = False)

x, y = 256*8, 160
s1 = s.inav[:x*y]
s2 = hs.signals.Signal2D(s1.data.reshape((y,x,256,256))).as_lazy()
s2.save('Raw_data.zspy', chunks = (64,64,64,64), overwrite=True) #save reshaped raw
    data

print("y= ", s2.axes_manager.navigation_axes[1].size)
print("x= " , s2.axes_manager.navigation_axes[0].size)
s = hs.load('Raw_data.zspy', lazy=True)

#save slices
s_flat = hs.signals.Signal2D(s.data.reshape(
    s.axes_manager.navigation_axes[0].size*s.axes_manager.navigation_axes[1].size,
    256, 256))
s_flat.set_signal_type('electron_diffraction')
num_slices = 8
vbf_list=[]
for slice_num in range(num_slices):
        slice_sig = hs.signals.Signal2D(s_flat.data[slice_num::8, :, :].reshape(s.
    axes_manager.navigation_axes[1].size,s.axes_manager.navigation_axes[0].size/
    num_slices, 256, 256))
        slice_sig.set_signal_type('electron_diffraction')
        slice_sig.save('slice%i.hspy'%(slice_num), chunks=(32, 32, 32, 32),overwrite=
    True)
        vbf=slice_sig.T.sum()
        vbf_list.append(vbf)

vbf_stack = hs.stack(vbf_list, axes=0)
vbf_stack.save("vbf_8SSPED_stack.hspy",overwrite=True)


#### ALIGNING VBF OF SLICES ####
s_8SSPED = hs.load("vbf_8SSPED_stack.hspy")
s = s_8SSPED

#number of pixels to shift slices, using align2D
shift = [
    [0,0],
    [5,0],
    [10,-2],
    [13,-5],
    [12,-7],
    [9,-9],
    [4,-9],
    [0,-9]]
shift=np.array(shift)
```

```
57
58 aligned_stack= s.deepcopy()
59 aligned_stack.align2D(reference='cascade',shifts = shift, crop = True)
60
61 test_stack = hs.stack([aligned_stack.inav[0],aligned_stack.inav[1]],axes=0) #compare
       two slices
62 test_stack.plot(norm='log', cmap='viridis')
63
64 #shifts need to be in this form fo be used with da.roll(): sign of y changed and list
       turned to tuples
65 shift_list = []
66 for s in shift:
67     shift_list.append((-s[0], s[1]))
68
69 #### CORRECTING SSPED DATASETS ####
70 #Run on IDUN
71 import matplotlib.pyplot as plt
72 import hyperspy.api as hs
73 import dask.array as da
74 import numpy as np
75 import scipy as sc
76
77 signal_list = hs.load("*.hspy", lazy=True) #load segments
78 original_signal_list=signal_list
79
80 shift_list = [ #shifts: Make sure on the correct form compared to Align2D
81     (0,0),
82     (-5,0),
83     (-10,-2),
84     (-13,-5),
85     (-12,-7),
86     (-9,-9),
87     (-4,-9),
88     (0,-9)]
89
90 for signal, shift in zip(signal_list, shift_list):
91     signal.data = da.roll(signal.data, shift, axis=(0, 1))
92
93 signal_stack = hs.stack(signal_list, rechunk=False)
94 signal_corrected = signal_stack.mean(axis=2, rechunk=False)
95 signal_corrected.save("8SSPED_corrected.zspy", chunks=(64, 64, 64, 64), overwrite =
       True)
96
97 signal_stack_not_corrected = hs.stack(original_signal_list, rechunk=False)
98 signal_not_corrected = signal_stack_not_corrected.mean(axis=2, rechunk=False)
99 signal_not_corrected.save("8SSPED_not_corrected.zspy", chunks=(64, 64, 64, 64),
       overwrite = True)
100
101
102 ####  DIFFRACTION PATTERN ROTATION ####
103 #run on IDUN
104
105 s_8SSPED_corrected = hs.load("s_8SSPED_corrected.hspy")
106 s_8SSPED_corrected =s_8SSPED_corrected.inav[:-9,:-13] #crop rolled pixels
107
108 s_8SSPED_original = hs.load("s_8SSPED_not_corrected.hspy")
109 s_8SSPED_original =s_8SSPED_original.inav[:-9,7:-6]
110
111 s_rot = s_8SSPED_corrected.rotate_diffraction(28)
112 s_rot_crop = s_rot.isig[34:222,34:222] #smallest possible square in cropped region
113
114 s_rot_original = s_8SSPED_original.rotate_diffraction(28)
115 s_rot_crop_original = s_rot_original.isig[34:222,34:222]
116
117 s_rot_crop.save("8SSPED_corr_rotated.zspy",chunks=(64,64,64,64))
118 s_rot_crop_original.save("8SSPED_not_corr_rotated.zspy",chunks=(64,64,64,64))
```

D.2.2 Analysis of corrected S-SPED

```
#### IMAGE ANALYSIS ####

#### VDF and intensity line plots ####
def set_scale(s):
    s.axes_manager[-1].scale = 0.0955
    s.axes_manager[-2].scale = 0.0955
    s.axes_manager[-1].units = '1/nm'
    s.axes_manager[-2].units = '1/nm'

    s.axes_manager[0].scale = 0.686
    s.axes_manager[1].scale = 0.686
    s.axes_manager[0].units = 'nm'
    s.axes_manager[1].units = 'nm'

s = hs.load("8SSPED_corr_rotated.zspy")
set_scale(s)

#Convenient plot to observe diffractoin pattern shifts
s.sum(axis=0).plot(norm='symlog',cmap='viridis')

#Select diffraction spots for VDF
roi1 = hs.roi.CircleROI(cx=45.842, cy=40.685, r=0.52525, r_inner=0) #LFO domain 1
roi2 = hs.roi.CircleROI(cx=46.988, cy=42.213, r=0.52525, r_inner=0) #LFO domain 2
roi3 = hs.roi.CircleROI(cx=42.6905, cy=38.393, r=0.52525, r_inner=0) #111-spot (
    bright LSMO)

#Make VDF
vdf_d1 = s.get_integrated_intensity(roi1)
vdf_d2 = s.get_integrated_intensity(roi2)
vdf_d3 = s.get_integrated_intensity(roi3)

line_d1 = vdf_d1.isig[15.:50.,:].sum(axis=0) #cutting unecessary regions
line_d2 = vdf_d2.isig[15.:50.,:].sum(axis=0)
line_d3 = vdf_d3.isig[15.:50.,:].sum(axis=0)

line_d1 = hs.signals.Signal1D(line_d1)
line_d2 = hs.signals.Signal1D(line_d2)
line_d3 = hs.signals.Signal1D(line_d3)

line_d1.axes_manager[0].scale = 0.686
line_d1.axes_manager[0].units = 'nm'
line_d2.axes_manager[0].scale = 0.686
line_d2.axes_manager[0].units = 'nm'
line_d3.axes_manager[0].scale = 0.686
line_d3.axes_manager[0].units = 'nm'

line_d1.save("line_d1.hspy")
line_d2.save("line_d2.hspy")
line_d3.save("line_d3.hspy")

#line plots
fig, ax = plt.subplots()
s = hs.load("line_d1.hspy")
ax = plt.imshow(s,cmap='viridis',norm='log')
plt.xticks([])
plt.yticks([])
fig.savefig("line_d1.png",bbox_inches = 'tight',dpi=400)
plt.show()


#### DIFFRACTION PATTERNS FROM ROIS ####
roi1 = hs.roi.RectangularROI(left=87.808, top=39.788, right=120.05, bottom=43.904) #
    LFO domain 1
roi2 = hs.roi.RectangularROI(left=17.15, top=38.416, right=49.392, bottom=42.532) #
    LFO domain 2
```

```
roi3 = hs.roi.RectangularROI(left=76.832, top=89.866, right=109.074, bottom=93.982) # DSO

s_diff1 = s.T.get_integrated_intensity(roi1)
s_diff2 = s.T.get_integrated_intensity(roi2)
s_diff3 = s.T.get_integrated_intensity(roi3)
```

D.3 EELS

```
import hyperspy.api as hs
import matplotlib.pyplot as plt
from hyperspy.misc.eels.tools import get_edges_near_energy


#### SIGNAL LOADING AND SPIKE REMOVAL ####
s = hs.load("*.dm4")
s_hl = s[5]
s_ll = s[6]

s_ll.spikes_removal_tool()
s_hl.spikes_removal_tool()
s_ll.save('s_ll_cosmic.hspy')
s_hl.save('s_hl_cosmic.hspy')

s_ll = hs.load('s_ll_cosmic.hspy')
s_hl = hs.load('s_hl_cosmic.hspy')


#### CREATING MODEL FOR BACKGROUND REMOVAL ####
#Run on IDUN
import hyperspy.api as hs
import matplotlib.pyplot as plt
from hyperspy.misc.eels.tools import get_edges_near_energy

s_ll = hs.load("s_ll_cosmic.hspy")
s_ll.add_elements(('Fe','Mn', 'O', 'Dy', 'Sc', 'La'))
edges = ("Mn_L3", "Mn_L2", "O_K", "Fe_L3", "Fe_L2", "Ti_L3", "Ti_L2")
m = s_ll.create_model()
m.multifit()
m.enable_fine_structure()
m.multifit()
m.save("s_ll_model.zspy", overwrite = True)

s_hl = hs.load('s_hl_cosmic.hspy') #change things here
s_hl.add_elements(('Dy','La'))
m_hl = s_hl.create_model()
m_hl.multifit()
m_hl.enable_fine_structure()
m_hl.multifit()
m_hl.save("s_hl_model.zspy", overwrite= True)

#### MODEL BASED BACKGROUND REMOVAL (WITH FINESTUCTURE)####
s= hs.load('s_ll_model.zspy')
m2 = s.models.restore('a')

#Sc
m2.components.Sc_L3.active = False
s_sc = s- m2.as_signal()
s_sc.save('s_sc_br.hspy')
m2.components.Sc_L3.active = True

#O
m2.components.O_K.active=False
s_o = s - m2.as_signal()
s_o.save('s_o_br.hspy',overwrite=True)
```

```
m2.components.O_K.active = True

#Mn
m2.components.Mn_L3.active=False
s_mn = s - m2.as_signal()
s_mn.save('s_mn_br.hspy',overwrite = True)
m2.components.Mn_L3.active=True

#Fe
m2.components.Fe_L3.active=False
s_fe = s - m2.as_signal()
s_fe.save('s_fe_br.hspy',overwrite = True)
m2.components.Fe_L3.active=True


#### BACKGROUND REMOVAL WITHOUT FINE STRUCTURE ####
#Dy from hl
s_hl.add_elements(('La', 'Dy'))
m_hl = s_hl.create_model()
m_hl.active_components
m_hl.multifit()
m_hl.components.La_M2.active=False
m_hl.multifit()

#Turn off relevant element
m_hl.components.Dy_M5.active = False
m_hl.components.Dy_M4.active = False
s_dy_br = s_hl - m_hl.as_signal()
s_dy_br.save("s_dy_br.hspy")

#La from ll
s_ll.add_elements(('Fe','Mn', 'O', 'Sc','La'))
m_ll = s_ll.create_model()
m_ll.components.Sc_L1.active = False
m_ll.components.Mn_L1.active = False
m_ll.components.Fe_L1.active = False
m_ll.multifit()

m_ll.components.La_M4.active = False
m_ll.components.La_M5.active = False
s_la_br_multifit = s_ll - m_ll.as_signal()
s_la_br_multifit.save("s_la_br.hspy")


#### CHEMICAL LINE PROFILES ####
s_mn_br = hs.load("s_mn_br.hspy")
s_o_br = hs.load("s_o_br.hspy")
s_sc_br = hs.load("s_sc_br.hspy")
s_fe_br= hs.load("s_fe_br.hspy")
s_dy_br = hs.load("s_dy_br.hspy")
s_la_br = hs.load("s_la_br.hspy")

s_o_crop = s_o_br.isig[520.:550.]
s_o_line = s_o_crop.sum(axis=-1).T

s_mn_crop = s_mn_br.isig[630.:660.]
s_mn_line = s_mn_crop.sum(axis=-1).T

s_fe_crop = s_fe_br.isig[700.:730.]
s_fe_line = s_fe_crop.sum(axis=-1).T

s_sc_crop = s_sc_br.isig[450.:470.]
s_sc_line = s_sc_crop.sum(axis=-1).T

s_dy_crop = s_dy_br.isig[1286.:1337.]
s_dy_line = s_dy_crop.sum(axis=-1).T

```

```
s_la_crop = s_la_br.isig[770.:880.]
s_la_line = s_la_crop.sum(axis=-1).T

hs.plot.plot_spectra([s_dy_line, s_sc_line, s_fe_line, s_mn_line, s_la_line])

#### CHEMICAL COMPOSITION LINE SCAN PLOT ####
fig, ax = plt.subplots(figsize=(9,5))
interface = 19.7

ax.plot(s_o_line.axes_manager[0].axis -interface, s_o_line.data, label='O', color= 'r')
ax.plot(s_mn_line.axes_manager[0].axis -interface , s_mn_line.data, label='Mn', color = 'b')
ax.plot(s_fe_line.axes_manager[0].axis -interface, s_fe_line.data, label='Fe', color= 'g')
ax.plot(s_la_line.axes_manager[0].axis -interface, s_la_line.data, label='La', color= 'y')
ax.plot(s_dy_line.axes_manager[0].axis -interface, s_dy_line.data, label='Dy', color= 'purple')
ax.plot(s_sc_line.axes_manager[0].axis - interface, s_sc_line.data, label='Sc', color = 'lightblue')
ax.legend(prop={'size': 15})

ax.yaxis.set_ticks([])
plt.title("Relative chemical composition (LSMO/LFO)n/DSO", fontsize = 20)
ax.tick_params(axis='x', which='major', labelsize=17)
ax.set_xlabel('Line scan [nm]', fontdict={'fontsize': 17})
ax.set_ylabel('Intensity [arb. units]', fontdict={'fontsize': 17})


ax.annotate("DSO", (-18,240000), fontsize=17)
ax.annotate("LSMO/LFO", (6,150000), fontsize=17)
ax.axvline(x=0, color='black', linestyle=':')

plt.show()
fig.savefig("Relative_chem_comp_DSO.png", bbox_inches='tight', dpi=400)


#### EELS FINE STRUCTURE ####
# get fine structure from in each superlattice layer
def get_layer_plot(s,layer):
    lfo1= s.inav[21.:26.].sum(axis=0)
    lsmo1 = s.inav[29.:34.].sum(axis=0)
    lfo2 = s.inav[36.:41.].sum(axis=0)
    lsmo2 = s.inav[43.:48.].sum(axis=0)
    lfo3 = s.inav[50.:55.].sum(axis=0)
    lsmo3 = s.inav[57.:62.].sum(axis=0)
    lfo4 = s.inav[63.:68.].sum(axis=0)
    lsmo4 = s.inav[70.:75.].sum(axis=0)

    lfo_list = [lfo1, lfo2, lfo3,lfo4]
    lsmo_list = [lsmo1, lsmo2, lsmo3,lsmo4]
    layer_list = [lfo1, lsmo1, lfo2,lsmo1, lfo3,lsmo3 ,lfo4, lsmo4]

    c1 = 'green'#lfo
    c2 = 'blue'#lsmo
    if layer == "lsmo":
        stack=hs.stack(lsmo_list,axes=0)
        cascade_plot = hs.plot.plot_spectra(stack, style='cascade',color=c2,padding = 0.7)
    if layer == "lfo":
        stack=hs.stack(lfo_list,axes=0)
        cascade_plot = hs.plot.plot_spectra(stack, style='cascade', color = c1, padding = 0.7)
    if layer == "all":
        stack=hs.stack(layer_list,axes=0)
        color_list = [c1,c2]*4
```

```
183         cascade_plot = hs.plot.plot_spectra(stack, style='cascade',color = color_list
    , padding = 0.9)
184     return stack
185
186 #interesting fine structures
187 lfo_o_K = get_layer_plot(s_o_crop,"lfo")
188 lsmo_o_K = get_layer_plot(s_o_crop, 'lsmo')
189 lfo_fe_L23 = get_layer_plot(s_fe_crop, "lfo")
190 lsmo_mn_L23 = get_layer_plot(s_mn_corp, "lsmo")
191
192
193 #plotting (done similarly for all edges)
194 s= lfo_O_K
195 fig, ax = plt.subplots(figsize=(2,6))
196 diff = 0.8 #plot separation
197 num_layers = 4
198 for i in range(num_layers):
199     spectrum = s.inav[i]
200     spectrum /= spectrum.max(axis=-1) #normalizing
201     ax.plot(spectrum.axes_manager[0].axis, spectrum.data +diff*i, color= 'g')
202
203 ax.yaxis.set_ticks([])
204 plt.title("O-K LFO", fontsize = 17)
205 ax.tick_params(axis='x', which='major', labelsize=17)
206 ax.set_xlabel('Energy loss [eV]', fontdict={'fontsize': 17})
207 plt.show()
208 fig.savefig("O_K_LFO_DSO.png",bbox_inches='tight' ,dpi=400)
209
210 #### FINE STRUCTURE PEAK RATIOS ####
211 def get_mean_ratio(ratios):
212     return sum(ratios.data)/len(ratios.data)
213
214
215 ratio_list = []
216 num_layers = 4
217 for i in range(num_layers):
218     s = lfo_fe_L23.inav[i]
219     s_fe_l3 = s.isig[705.:717.] #L3 energy
220     s_fe_l2 = s.isig[717.:728.] #L2 energy
221     l3_l2_ratio = s_fe_l3.sum(axis=-1).T / s_fe_l2.sum(axis=-1).T
222     mean_ratio = get_mean_ratio(l3_l2_ratio)
223     ratio_list.append(mean_ratio)
224
225
226 #### CHEMICAL SHIFTS THROUGH SINGLE LAYERS ####
227 #Mn
228 s_mn_rebin = s_mn_crop.rebin(scale =(6,1))
229
230 s_mn1_top = s_mn_rebin.inav[22:24].sum() #bottom layer (closest to DSO)
231 s_mn1_bottom = s_mn_rebin.inav[29:31].sum()
232
233 s_mn2_top = s_mn_rebin.inav[34:36].sum() #second layer
234 s_mn2_bottom = s_mn_rebin.inav[40:42].sum()
235
236 s_mn3_top = s_mn_rebin.inav[46:48].sum() #third layer
237 s_mn3_bottom = s_mn_rebin.inav[52:54].sum()
238
239 s_mn4_top = s_mn_rebin.inav[56:58].sum() #top layer
240 s_mn4_bottom = s_mn_rebin.inav[64:66].sum()
241
242 s_mn_shift = [
243     [s_mn1_top,s_mn1_bottom],
244     [s_mn2_top, s_mn2_bottom],
245     [s_mn3_top, s_mn3_bottom],
246     [s_mn4_top, s_mn4_bottom]]
247
248 #acquisition of Fe and O ELNES done similarly
```

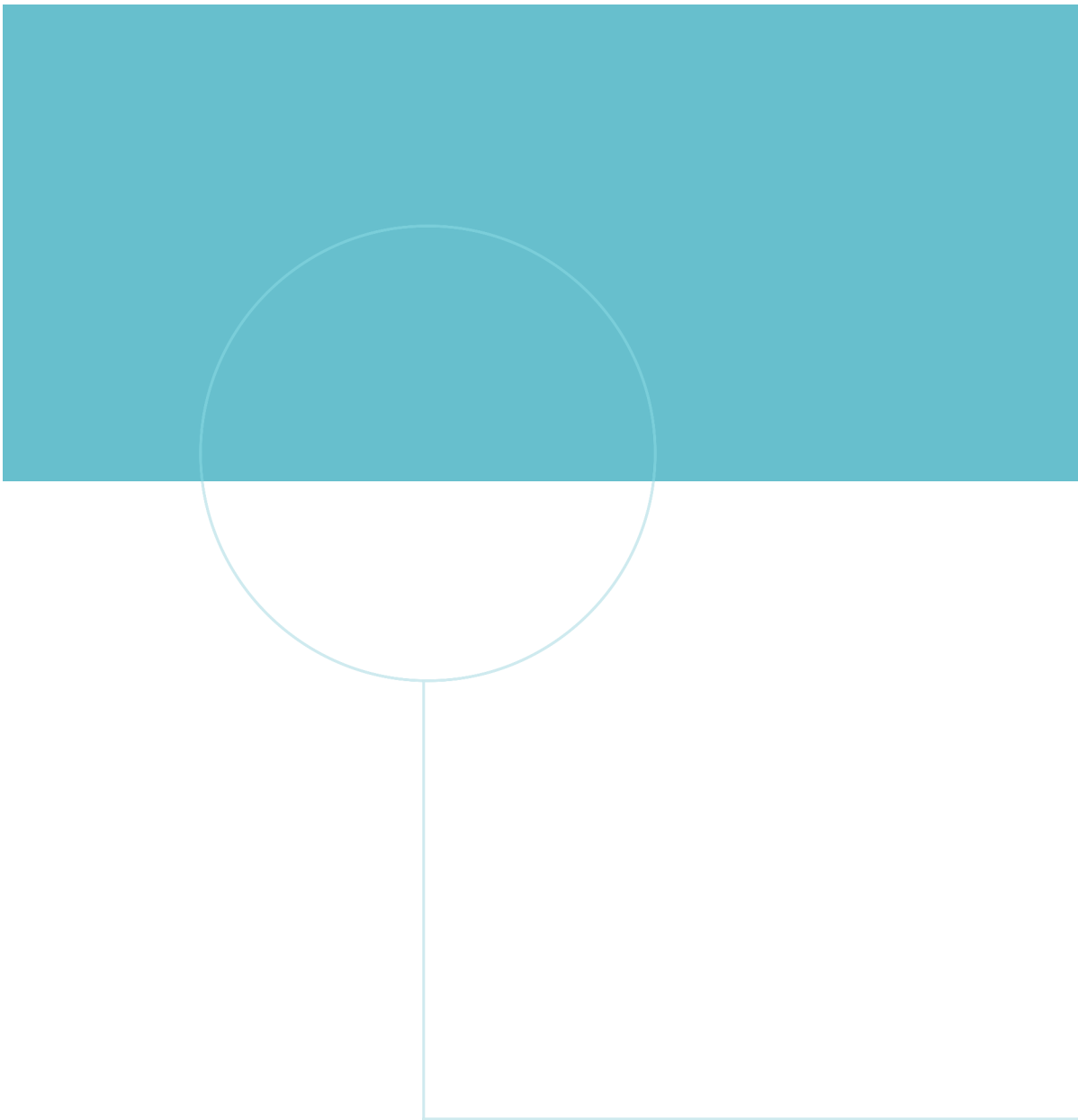

NTNU

Norwegian University of
Science and Technology